DTU Library

Correlating Structure and Reactivity: MoS2 Nanoparticles for Hydrogen Evolution

Jørgensen, Kristina Pilt; Nielsen, Jane Hvolbæk

Publication date:
2007

Document Version
Early version, also known as pre-print

Link back to DTU Orbit

Ph.D. thesis
Department of Physics
Center for Individual Nanoparticle Functionality
The Technical University of Denmark
-

Correlating Structure and Reactivity: MoS$_2$ Nanoparticles for Hydrogen Evolution

Kristina Pilt Jørgensen

March 2007

Preface

This thesis is submitted in partial fulfillment of the requirements for the Ph.D. degree from the Technical University of Denmark. The project has been carried out at the Institute of Physics at the Technical University of Denmark, within the Interdisciplinary Center for Catalysis, ICAT and Center for Individual Nanoparticle Functionality, CINF, during the last three years under the supervision of Dr. Jane H. Nielsen. Financial support was provided by the Technical University of Denmark

I would like to take this opportunity to spend a few words of thanks. First I would like to thank my supervisor Jane H. Nielsen for enlightening discussions and encouraging supervision. This thanks is certainly extended to Ib Chorkendorff who stepped in when Jane was not available and has stayed in since. During the work on MoS_2 on Au I worked closely with Thomas Jaramillo and enjoyed many enlightening and fun hours in his company. I would like to thank Sebastian Horch for his help with the STM, for teaching me tips and tricks from his many years of experience with the STM and for stepping in to do STM in his chamber when it turned out that our STM did not withstand H_2S. A great thanks goes to Hans Christian Sørensen and Dan Shacham from our workshop and to the father of the Aarhus STM Erik Lægsgaard for their high quality help and positive attitudes.

I would like to thank the members ICAT, CINF and CAMP over the years for contributing to making not only a nice work place, but also a community. Working and socializing with you has been a pleasant and inspiring experience. Last, but not least, I would like to express my loving thanks to Per for his love and support during the joys and frustrations of this work.

Kristina Pilt Jørgensen
Lyngby, March 30$^{\text{th}}$ 2007

ii

Abstract

The title of this thesis is Correlating Structure and Reactivity: MoS_2 Nanoparticles for Hydrogen Evolution. In the work, MoS_2 nanoparticles have been imaged with UHV STM on different substrates to relate their structure with their activity for hydrogen evolution measured at ambient conditions.

The MoS_2 morphology on etch pitted highly ordered pyrolytic graphite was imaged showing 3-4nm wide, 1-1.5nm high particles of MoS_2 on the surface. The binding of the particles to the substrate was very weak and increased annealing temperatures during preparation of the particles and the introduction of sputter defects were chosen as a strategy to improve the conditions for resolving the particles. During these experiments, the Besenbacher group achieved the first resolved imaged of hexagonal MoS_2 nanoparticles on HOPG and further studies on this system was therefore stopped.

The attention was then turned to studying MoS_2 on Au(111). On the Au(111) surface MoS_2 nanoparticles were synthesized using annealing temperatures of 400°C and 550°C and characterized by XPS and STM verifying that that both preparation procedure yielded primarily triangular or truncated triangular MoS_2 nanoparticles. The morphology as a function of coverage was investigated and for the single layered morphologies, the activity for hydrogen evolution was measured in an electrochemical cell at ambient conditions. The activity was shown to scale with the edge length of the particles, identifying the active site for the reaction to the particle edge. Finally, the activity of the active site was shown to be in the high range, above that of the common metals.

iv

Resumé

Titlen på denne afhandling er Korrelation af struktur og reaktivitet: MoS_2 nanopartikler til brintudvikling. I det præsenterede arbejde er MoS_2 nanopartikler blevet afbildet med UHV STM på forskellige overflader for at kunne relatere strukturen af disse partikler til deres brintudviklingsaktivitet ved gængse betingelser.

På æts-modificerede HOPG overflader er MoS_2 morfologien blevet afbildet og viser 3-4nm brede, 1-1.5nm høje MoS_2 partikler. Partiklernes binding til substratet er meget svag og en strategi af øgede temperaturer under præparationsproceduren og introduktion af sputringsdefekter blev valgt for at forbedre afbildningsbetingelserne på overfladen. Under disse eksperimenter, opnåede Besenbacher gruppen de første billeder der viste opløsning af heksagonale MoS_2 partikler på HOPG og videre studier på dette system blev derfor stoppet.

Fokus blev i stedet rettet mod studier af MoS_2 på Au(111). MoS_2 nanopartikler blev syntetiseret på Au(111) overfladen ved brug af annealing temperaturer på 400°C og 550°C og efterfølgende karakteriseret med XPS og STM, hvilket verificerede at begge præparationsmetoder førte til enkelt-lags trekantede eller trunkerede trekantede MoS_2 nanopartikler. Morfologien blev undersøgt som funktion af dækningsgraden og for de enkelt-lagede morfologier blev aktiviteten for brintudvikling målt i en elektrokemisk celle ved gængse betingelser. Det blev påvist at aktiviteten skalerer med kantlængden på partiklerne, hvilken identificerer det aktive site til partiklernes kant. Endelig vistes det at aktiviteten af det aktive site lå i den høje ende, over aktiviteten af de almindelige metaller.

Contents

Chapter 1

Introduction

1.1 Heterogeneous catalysis and Surface Science

Catalysis is a far spanning field, which provides modern society with a range of chemicals, pharmaceuticals, commodities, fertilizers and fuels as well as means for preventing pollution [1, 2]. Most catalytic processes are liquid or gas-phase reactions that are catalyzed heterogeneously on the surface of transition-metal based particles. Compared to the uncatalyzed reactions, these surfaces enable energetically favorable reaction pathways, where one or more reaction barriers are lowered, enabling a higher rate of the reaction. The reactions typically proceed in a series of elementary steps on the surface, such as adsorption, diffusion, reaction and desorption of product. In each of these steps the interaction between the surface of the catalyst and molecules and atoms going through the step has an impact on the barriers for that step, ultimately determining the rate of the reaction. In understanding heterogeneous catalysts it is vital that one understands the surface of the catalyst material on an atomic level, as different surface geometries - sites - will influence the reaction steps differently. In the simplest case, one kind of site lowers the rate-limiting step of the reaction much more than any other sites, and thus determines the overall catalytic performance; the catalytic turnover scales linearly with the exposed active surface sites of the catalytic nanoparticles.

Industrial catalysts consist of catalytic nanoparticles on highly porous supports, that among other things serve to optimize the number of active sites exposed. The shape and size of the catalytic nanoparticles is influenced by the interaction with this support material and determines the distribution of sites exposed on the particle surface. The complex structure of the

catalyst and the environments of the catalytic particles under operating conditions make the investigation of the catalytic surfaces in this setting immensely difficult. Therefore the general approach is to ease the investigation and the understanding of the catalyst by breaking it down into different components and study these.

In surface science this is generally done by studying model systems in well-defined environments. The most simple model system is low-index single crystals studied in Ultra High Vacuum (UHV). Much insight has been gained from such studies [1, 3], but this type of model system does not enable the study of the undercoordinated surface atoms on a nanoparticle. The effect of these can be elucidated by the study of a slightly more complex system: stepped single crystals. In fact, studies of such surfaces indicate that the undercoordinated step sites may completely dominate the catalytic activity, as the activity of these sites may be orders of magnitude larger than the terrace sites [4]. An example where such simple model systems have provided valuable insights into a reaction, is ammonia synthesis, where studies have shown that the crystal steps completely dominate the activity and insight from surface science has enabled the design of better catalyst based on understanding the trends of molecule-surface interaction [4–8].

The next step up in complexity of the model systems is of course to study catalytic nanoparticles on a simple support material e.g. a single crystal. This is more challenging both due to the increased complexity of the model system, but also due to the fact that many of the spectroscopies of surface science are averaging techniques, which do not resolve the diversity of the nanoparticles, which will have a certain size and shape distribution. Therefore in these studies microscopies have proven essential to the understanding [3, 9].

Similarly to the increased complexity in the material of the model, the complexity of the environment of the model system may also be increased. Reactivity is rarely straightforwardly measured in UHV setups as most reactions take place at pressures that are either un-realizable in UHV chambers or just destroy the well-controlled vacuum if a chamber is subjected to them. The most simple approach to gauge activity is adsorption and/or exchange-type studies in UHV [1, 2]. Here the activity is not measured, but vital adsorption, desorption or recombination steps in a reaction are followed either by TPD-type experiments, exchange experiments or STM imaging of e.g. adsorbed or decomposed molecules. Approaching industrial conditions, one may attach a so-called high pressure cell to a UHV chamber, allowing studies at pressures above 10^{-6} Torr that will destroy the vacuum in a

separated part of the chamber, where higher pressures may be realized [1]. Another approach is to subject ones well-controlled and UHV characterized model system to industrial conditions outside the chamber. This is very rarely straightforward as problems with sample oxidation by the air, lack of enough signal from the very low surface area of the model systems, corrosion etc. often occur.

The model systems studied in the work presented in this thesis are MoS_2 nanoparticles on two different substrates. The activity of the model system is measured under ambient conditions. Thus the model systems and conditions presented here strive to climb the latter of complexity of model systems in the aim to relate the catalytic activity to the sites on the nanoparticulate catalyst.

1.2 Hydrogen evolution

Alternative energy carriers such as hydrogen are of growing interest as fossil fuels pose increasing environmental concerns and are expected to become increasingly costly and less easily available [10–12]. If hydrogen is to become viable as an alternative energy carrier technological improvements and cost reductions are needed in its production and storage and in fuel cell technology [10, 13, 14]. Today, the dominating way of producing hydrogen is by steam reforming of natural gas, but hydrogen can also be produced cleanly and renewably e.g. by electrolysis if the current is supplied from renewable sources such as hydro, solar or wind energy. Electrolysis is the splitting of water into hydrogen and oxygen by applying a voltage difference between to electrodes, one catalyzing the formation of hydrogen, the other the formation of oxygen. Unfortunately, the hydrogen evolution reaction, by which hydrogen is formed, is catalyzed most effectively by Pt-group metals which are scarce and expensive [15]. Thus if the scheme of using electrolysis to produce hydrogen is to become viable, new materials are needed.

Hydrogen evolution is the reaction whereby H_2 molecules are formed electrochemically from protons and electrons in solution. The overall reaction can be written

$$2H^+ + 2e^- \rightarrow H_2$$
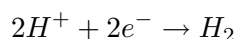
The reaction takes place at an electrode, supplying electrons and catalyzing the reaction. In acidic solutions it is generally agreed that the reaction proceeds by the adsorption of atomic hydrogen at the electrode surface [15, 16]

$$H^+ + e^- + * \rightarrow H*$$
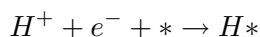
This is followed by one of two pathways to the formation of molecular hydrogen, either hydrogen is formed from two adsorbed hydrogen atoms

$$2H* \rightarrow H_2$$
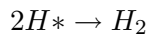
or it is formed by the reaction of an adsorbed hydrogen with another proton and electron

$$H^+ + e^- + H* \rightarrow H_2$$

Irrespective of the pathway, two electrons are used in the formation, and thus the current drawn is a measure of the turnover of the reaction.

Usually, hydrogen evolution has been investigated using electrochemistry techniques in combination with spectroscopic techniques for catalyst characterization [15]. The activity for hydrogen evolution is measured by the exchange current density; a measure of the catalytic turnover at equilibrium voltage in terms of the current evolved in the reaction normalized to the electrode surface area [17–20]. From peaks in cyclic voltammograms and the slopes of exchange current densities plotted against voltage, electrochemist can in some cases gain insight on e.g. the binding of surface species during reaction and the reaction mechanism, but many factors complicate these interpretations [15].

Analogous the descriptions of turn over in the field of gas-phase catalysis, the exchange current density has been related to kinetic parameters. The logarithmic plot of the exchange current density as a function of physico-chemical parameters such as experimentally determined work-function, metal-hydride enthalpy of formation and Gibbs free energy of hydrogen adsorption [18–20] have shown volcano-type relations. Volcano relationships basically reflect the Sabatier principle; a general framework in catalysis that explains that optimal surfaces exhibit moderate binding energies of reaction intermediates. Recently, a simple kinetic model was described which shows that the exchange current density should be well-described by the Gibbs free energy of hydrogen adsorption of a catalytic material [17]. A volcano relationship was found by showing that the best electrode materials are those for which the reaction is thermo-neutral, i.e. the Gibbs free energy of hydrogen adsorption ΔG_H is zero. This trend is based on a simple kinetic model and therefore one may expect the criterion of $\Delta G_H \cong 0$ to be necessary but not sufficient. Experimentally determined exchange current densities of pure metals plotted as a function of the DFT-calculated ΔG_H confirmed the predictions of the model as seen in figure 1.1. The calculation of a free energy

of hydrogen adsorption by DFT is relatively fast, and thus the criterion allows one to use DFT as a screening tool for new materials, speeding up and perhaps widening out the search for better materials as the experimental effort can be focussed on those materials predicted by the model to be most interesting.
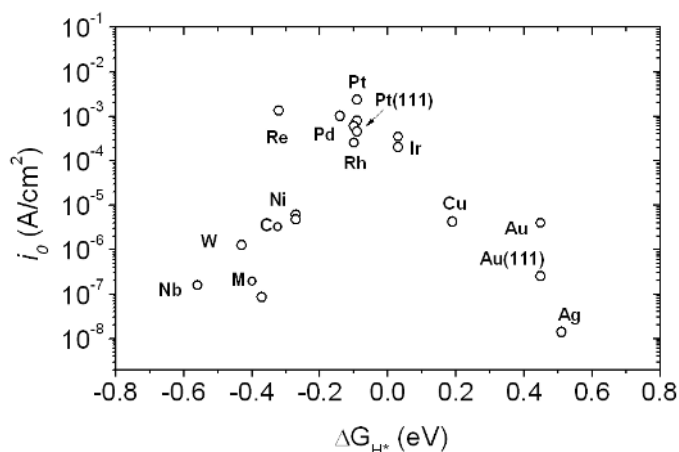

Figure 1.1: Volcano plot of the exchange current density as a function of the DFT-calculated Gibbs free energy of adsorbed hydrogen for the pure metals. Samples are polycrystalline unless otherwise noted. The Gibbs free energies are from [17]. Exchange current densities are from [19, 21–24]

1.3 MoS$_2$ for hydrogen evolution

When searching for an optimal material for a catalyst for a reaction, one place to look for inspiration is in enzymes. Many enzymes are essentially catalysts for reaction needed in our bodies. For hydrogen evolution one may look at e.g. the enzyme hydrogenase or the enzyme nitrogenase which both catalyze the evolution of hydrogen. This was the approach of Berit Hinnemann and Jens Nørskov in Paper I. The active centers of these enzymes also fulfill the criterion of $\Delta G_H \cong 0$ as seen in figure 1.3, indicating that this may be true for all good hydrogen evolution catalysts. Searching for other materials that obey the criterion, MoS$_2$ nanoparticles were found to be interesting.

MoS$_2$ nanoparticles have received much interest as they have been used as desulphurization catalysts for decades and are also of interest in the field

of photocatalysis [25–27]. MoS_2 consists of trilayers of S, Mo and S in a hexagonal lattice as illustrated in figure 1.2. The trilayers stack like sheets of graphite, held together by van der Waals forces, but also exist as single trilayers depending on the support and surrounding conditions. The most common form is the $2H$-MoS_2 form, which is the form found in the natural form pure MoS_2, molybdenite [28]. In the $2H$-MoS_2 form, the second layer is translated one half compared to the first. MoS_2 also exists in a $3R$-MoS_2 form where the layer positions repeat every three layers [29] as well as in more unordered structures like the rag structure [30].
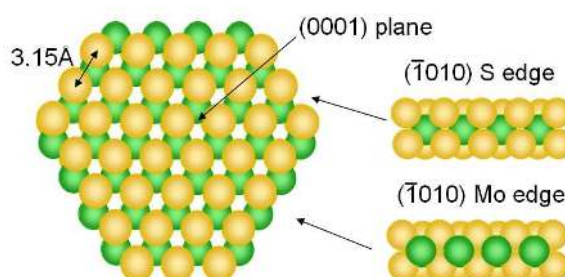

Figure 1.2: The stucture of a MoS_2 trilayer. The atomic distances in the basal plane are 3.15Å. The two possible terminations of the (0001) plane are seen to the right: the S edge and Mo edge. In sulphiding conditions the Mo edge will be additionally sulphided. When stacked the trilayers are held together only by van der Waals forces, separated by 6.15Å from Mo to Mo [31].

Previous studies of MoS_2 as a hydrotreating catalyst have extensively characterized the catalyst using a large range of techniques [25, 27]. The relation between the activity (and selectivity) and the geometric and electronic structure of the catalyst has been studied extensively, and the structure of the active phase of the catalyst has been established to be MoS_2 nanoparticles on high area and porosity γ-AlO_3 supports, largely by extended x-ray absorption fine-structure spectroscopy (EXAFS) [25]. For the hydrodesulphurization (HDS) reaction the activity has long been associated with the edge of the particles as the basalplane is very inactive [25, 32, 33]. TEM imaging of the nanoparticles gives limited resolution of the particle shapes as sufficient contrast is usually only present, when the particles are imaged edge on [34]. The growth of the particles is usually such that the MoS_2 particles lie with the basalplane parallel to the substrate, although edge-bonded

structures have also been observed [27, 35, 36] Recently, basalplane images of MoS$_2$ particles have been obtained using high-angle annular dark-field scanning transmission electron microscopy [37], but a detailed characterization of the structure of the particles is still generally beyond the reach of electron microscopies.

Further light has been shed on the detailed structure of the MoS$_2$ nanoparticles by a recent combination of STM and DFT studies by the Besenbacher and Nørskov groups. STM images of MoS$_2$ on Au(111) revealed that the MoS$_2$ nanoparticles on this surface were single layered triangular or hexagonal particles depending on the sulphiding conditions and that a bright rim lined the particle edge, attributed by DFT to a conducting state in the otherwise semiconducting MoS$_2$ following the particle perimeter [38–40]. The Mo edge of the particles was shown to more stable than the S edge and the Mo edge was shown to be sulphided. The sulfur termination can be either dimers as observed or monomers depending on the sulphiding conditions. The activity of the edge was finally indicated by adsorption studies using hydrogen and thiophene [41, 42].
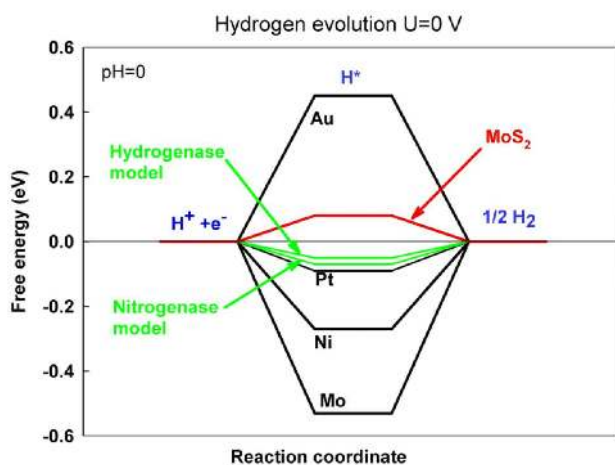

Figure 1.3: The calculated free energy diagram for hydrogen evolution for Au(111), Mo(110), Pt(111), hydrogenase, nitrogenase and MoS$_2$.

The DFT calculated free energy diagram of MoS$_2$ nanoparticles for hydrogen evolution can be seen in figure 1.3. As seen in the figure, ΔG_H for

MoS$_2$ is close to zero, indicating that this may be a very interesting hydrogen evolution catalyst. The DFT calculations are based MoS$_2$ nanoparticles terminated by the Mo-edge with sulphur monomers, which is the predicted termination under the employed reaction conditions [43]. The first hydrogen adsorbing on the sulphided Mo edge is strongly bound, whereas the second hydrogen adsorbs with a Gibbs free energy of 0.08eV. Thus the reaction turns over at this hydrogen coverage, and therefore this is the relevant value of ΔG_H. This is also the value seen in figure 1.3, from which it can be seen that ΔG_H for the hydrogen adsorption on MoS$_2$ is on the same order with opposite signs of that of Pt, which seems very promising. It is interesting to note, that in both MoS$_2$ and the nitrogenase enzymes, the sulfur atom that binds the hydrogen is twofold bound to a transitionmetal atom, Mo and Fe respectively, a coordination which might be important for the catalytic activity.
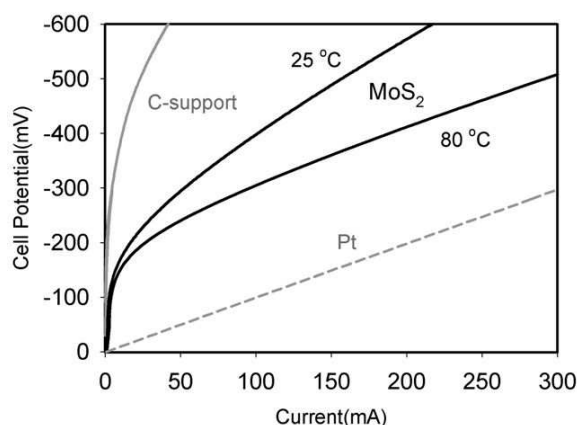
Figure 1.4: Polarization curves for Pt, carbon support and MoS$_2$ cathodes.

Having identified MoS$_2$ to be a candidate as a good hydrogen evolution catalyst, its ability to catalyze hydrogen evolution was tested experimentally. This was done by Jacob Bonde in Paper I in a membrane electrode assembly with a platinum electrode on one side and a MoS$_2$ on graphite electrode at the other. The measured I-V curves (polarization curves) are seen in figure 1.4 and show that MoS$_2$ is a reasonable catalyst material; hydrogen is evolved at an overpotential of 0.1-0.2V. This experimental test shows that MoS$_2$ indeed catalyzes the hydrogen evolution reaction as predicted lending weight to the DFT based predictions.

1.3.1 Unanswered questions

Having seen that nanoparticulate MoS_2 is a catalyst for hydrogen evolution a number of questions remain. How good is this catalyst, what is its structure and is the active site for the reaction on the edge as proposed? These cannot be answered from the experiments in the membrane electrode assembly. Here highly controlled and characterized experiments are needed. We therefore set out to answer these questions by preparing UHV MoS_2 model systems, characterizing them using STM and measuring their activity under ambient conditions.

1.4 Thesis outline

In this chapter an introduction to the field of surface science and heterogenous catalysis was given and the motivation and background of the work presented in the following parts of the thesis was described. In chapter 2, the experimental techniques used in the work are presented with special emphasis on Scanning tunneling Microscopy which is the core technique applied. Chapter 3 describes STM experiments on a MoS_2 on HOPG model system. Chapter 4 describes STM experiments on a MoS_2 on Au(111) model system and links these to hydrogen evolution activity measurements on the model system. Finally, the conclusions are summarized and an outlook on further investigations is given.

Chapter 2

Experimental techniques

The experimental techniques applied in the work presented in this thesis include X-ray photoelectron spectroscopy and scanning tunneling microscopy in UHV and electrochemical measurements of the activity for hydrogen evolution. This combination of techniques allows for the chemical composition of the surface of sample to be analyzed and the structure of surface the samples to be imaged under the well-controlled UHV conditions after which the activity under ambient conditions of the carefully prepared and characterized UHV samples can be measured and linked to the structure and composition of the samples.

2.1 X-ray Photoelectron Spectroscopy

X-ray Photoelectron Spectroscopy (XPS) is based on the simple principle of radiating x-ray photons onto the sample, where the energy of these photons may be transferred to electrons bound in the atoms of the sample. This will allow the electrons to escape the atom with a kinetic energy corresponding to the photon energy, $h\nu$, minus the binding energy the electron had in the atom, $E_{binding}$, and the work function of the sample, ϕ_{sample}

$$E_{kin} = h\nu - E_{binding} - \phi_{sample} \tag{2.1}$$

If the photons used in the spectroscopy have a well-defined known energy, measuring the kinetic energy of the escaped electrons will result in a spectrum with peaks corresponding the the energy levels of the electrons in the sample atoms. The kinetic energy measured E'_{kin} is related to the kinetic energy of the electron when it escapes the surface trough the aligning

of the fermi levels of the sample and the analyzer, which results in

$$E'_{kin} + \phi_{analyzer} = E_{kin} + \phi_{sample} \qquad (2.2)$$

where $\phi_{analyzer}$ is the work function of the analyzer. The peaks in the spectrum therefore have energies given by [44]

$$E'_{kin} = h\nu - E_{binding} - \phi_{analyzer} \qquad (2.3)$$

The species present in the sample can be identified by referencing the spectrum to the spectra of the atomic species, which is available in a reference handbook [45, 46].

The method is surface sensitive because the escaping electrons have a relatively low mean free path in the surface, which ensures that only electrons escaping atoms in the surface layers escape the sample and are detected. The deepest layers probed in XPS spectra are ~20Å into the surface of the sample.

In this work, a RQ 20/38 dual Al/Mg anode X-ray source and a PHOI-BOS 100 hemispherical energy analyzer from SPECS were used in the XPS measurements.

2.1.1   Qualitative analysis

The general features seen in an XPS spectrum are a number of peaks; singlets and doublets, superimposed on a background, which increases on the lower kinetic energy side of each peak.

The background increase on the lower kinetic energy side of each peak is a result of electrons undergoing energy losses, when escaping the sample.

There are four kinds of peaks that may occur in a spectrum. They are energy level peaks, ghosts, satellites and energy loss peaks. The energy level peaks are generally more intense than the other peaks, their intensity reflecting the amount of the corresponding species in the surface. Ghost peaks correspond to traces of radiation from the anode not in use and are therefore shifted by the energy difference between the Mg and Al $K\alpha_{12}$ lines (233eV). Satellite peaks correspond to radiation from other peaks than the $K\alpha_{12}$-peak in the energy distribution of the x-rays from the anode. Energy loss peaks are peaks corresponding to excitation levels of the surface plasmons. The different kinds of peaks are observed with a declining frequency in XPS spectra in the order they are listed here.

The energy level peaks are singlets for s orbital electrons, and doublets for p, d and higher orbitals. The energy splitting of the levels is due to spin
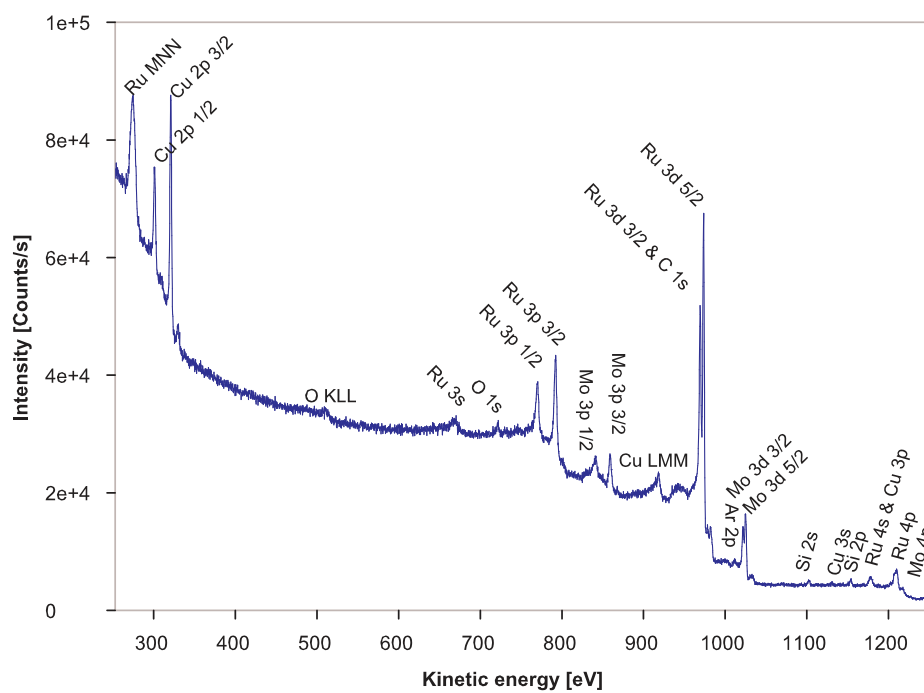
Figure 2.1: A broad XPS spectrum of an unclean Ru sample acquired using a Mg anode

orbit coupling. Further splitting may also occur, but has not been identified in our spectra. Depending on the chemical surroundings of an element its energy levels will shift slightly, which is known in XPS as the chemical shift of a peak. This may allow for not only the identification of the chemical species in a surface but also their chemical state, e.g. whether a metal is in a metallic, oxidized or sulphided form.

In figure 2.1 an example of a broad XPS spectrum of a Ru sample is seen. The spectrum covers a large energy range and reveals the presence of an abundance of species, as it was taken when the sample was not clean. Peaks from Ru, Cu, O, Mo, Ar, Si and C are seen in the spectrum as indicated by the labels. The Ru, Mo and Cu peaks are all expected to be present in the spectrum as an area including the Ru sample, Mo sample plate and Cu sample house contributes to the spectrum with the analyzer settings used. Ar most likely comes from a prior sputtering of the sample. The remaining peaks from Si, O and possibly C are due to impurities in the sample.

2.1.2   Quantitative analysis

From an XPS spectrum the relative concentrations of the species in the sample can be found by analyzing the peak intensities.

The intensity of a peak is the product of the probability for emission of a photoelectron per indicent photon P_{xk}, the number of photons $F_{h\nu}$ and the transmission function of the analyzer $T(E_{xk})$

$$I_{xk} = P_{xk}F_{h\nu}T(E_{xk})$$

where I_{xk} is the intensity from the energy level k in the species x [47].

P_{xk} is given by

$$P_{xk} = \sigma_{xk}N_x\lambda_{xk}$$

where σ_{xk} is the cross section of level k in the element x, N_x is the concentration of the species x in the surface and λ_{xk} is the mean free path of an electron emitted from level k in species x, travelling through species x.

Usually, the intensity can be expressed simply as

$$I_{xk} = S_{xk}N_xF_{h\nu}$$

where S_{xk} is known as the sensitivity factor and is available in reference materials.

Thus knowing the sensitivity factors and keeping the x-ray intensity constant, the relative intensities of peaks from level k in species x and level l in species y give the relative concentrations of species in the surface

$$\frac{I_{xk}}{I_{yl}} = \frac{S_{xk} N_x}{S_{yl} N_y} \tag{2.4}$$

In practice, the intensities are found by fitting the peak shapes observed by subtracting a background and fitting the peak shapes by bell shaped curves, such as e.g. Lorentzians and Gaussians with reasonable widths. For doublet peaks, requirements of a fixed splitting found in reference materials and a $2j + 1$ degeneracy are also often inferred.

2.2   Scanning Tunneling Microscopy

Scanning tunneling microscopy provides images of the topmost layer of the surface. It utilizes the quantum mechanical phenomenon tunneling to probe the local density of states at the Fermi level. This is done by holding a very sharp metallic needle (the tip) very close to the surface, applying a bias to it and scanning it across an area on the sample, while keeping the tunneling current between the tip and the sample constant. As the tunneling current is exponentially dependent on the distance between the sample and the tip, the vertical movement of the tip will image the topography of the surface.

There are two ways of operating the STM: Constant current mode and constant height mode. In constant current mode, the tip is moved towards and away from the sample, keeping the tunneling current constant, while scanning it across the sample. The image is generated by plotting the movement of the tip. In constant height mode, the tip is held at a constant height above the surface and the image is generated by plotting the measured tunneling current.

The images presented in this work are all in constant current mode. The tunneling parameters, i.e. current and voltage, used when acquiring a STM picture displayed in this work are stated, where the image is presented.

Theoretical treatment of the tunnel current is difficult, because the tunneling phenomenon is quantum mechanical and the exact geometry and composition of the system of tip and sample is unknown. Therefore large amounts of work has been done, investigating STM theoretically under a variety of different simplifying assumptions. This work is described elaborately in [48].

Tersoff and Hamann [49, 50] provided a simple description of the tunneling current, providing insight into the interpretation of STM images, by using Bardeens formalism to describe the tunneling current and applying it to a simple describtion of the tunneling conditions. Bardeens formalism [51] uses a time dependent treatment based on perturbation theory treating the tip and sample as two non-interacting systems instead of trying to solve the problem for the combined system. In this formalism the tunneling barrier is assumed rectangular and a transfer Hamiltonian describing the electron tunneling from the tip to the sample, is used. In three dimensions this leads to the following expression for the tunneling current

$$I = \frac{2\pi e}{\hbar} \sum_{\mu,\nu} \left\{ f(E_\mu) \left[1 - f(E_\nu + eU) \right] - f(E_\nu + eU) \left[1 - f(E_\mu) \right] \right\} \cdot |M_{\mu\nu}|^2 \delta(E_\nu - E_\mu)$$

where f is the Fermi distribution function, U is the applied bias between the tip and the sample, E_μ and E_ν are the energies of the unperturbed electronic states of the tip, ψ_μ, and the sample surface, ψ_ν, in the absence of tunneling. Finally $M_{\mu\nu}$ is

$$M_{\mu\nu} = \frac{-\hbar^2}{2m} \int d\mathbf{S} \cdot (\psi_\mu^* \nabla \psi_\nu - \psi_\nu \nabla \psi_\mu^*)$$

where $\mathbf{S}$ is any surface lying entirely in the vacuum region between the tip and the surface of the sample [48].

Tersoff and Hamann applied this approach to STM, assuming that the tip is spherical at its very end, so that its wavefunction can be approximated with an s-shaped orbital, and taking the low bias and low temperature limit [49, 50]. The expression for the tunneling current can then be reduced to

$$I \propto U \cdot n_t(E_F) \cdot e^{2\kappa R} \cdot n_s(E_F, \mathbf{r}_0)$$

where $n_t(E_F)$ is the density of states at the Fermi level, E_F, for the tip, the decay rate κ is $(2m\phi)/\hbar$, where ϕ is the effective local tunneling barrier height, R is the radius of the curvature of the end of the tip and $n_s(E_F, \mathbf{r}_0) = \Sigma_\nu |\psi_\nu(\mathbf{r}_0)|^2 \delta(E_\nu - E_F)$ is the surface local density of states at the Fermi level evaluated at the center of the curvature of the end of the tip $\mathbf{r}_0$.

Thus images obtained with the STM are not simply images of the sample topography as they may appear at a first glance, but may be understood as maps of the local density of states at the Fermi level provided that the tip wave function can be approximated by an s-orbital and that the density of states at the Fermi level of the tip does not change during the imaging.

If the exponential decay of the wavefunctions in the vacuum region is put into this equation, it is seen that the tunneling current and the distance, s, between the tip and the sample are exponentially related,

$$I \propto e^{-2\kappa s}$$

which is the basis of the very high lateral sensitivity of the STM. If a single atom on the tip sticks out 1Å it will carry 90% of the tunneling current [2].

Within the Tersoff-Hamann model, features on the surface are imaged according to the way they influence the LDOS of the surface. This has been further supported by calculation by Lang [52, 53], showing that e.g. S and He adsorbed on a jellium surface are imaged as a protrusion and a depression respectively. Thus if the local density of states is enhanced or depleted by e.g. an adsorbate, the STM image will show a protrusion or depression

as the tip has to move away from or closer to the surface to maintain a constant current.

In summary, the STM images are maps of the local density of states of the surface. As a very first approach to interpreting STM images, one may think of it as a surface topography, as features such as steps are imaged in this fashion. For images on the atomic scale or where two different materials are present on the surface this picture is insufficient for the interpretation of the images. Here one must remember that the images reflect the local density of states, and interpretations of the images should be careful and preferably supported by e.g. DFT calculations of the structures observed.

2.2.1   The Construction of the Århus STM

The total STM unit is attached to a flange on the UHV-chamber. It can be seen in figure 2.2. As can be seen the STM unit is very compact. This has the advantage of keeping the resonance frequency of the unit high, in order to obtain the required steadiness of the system, that allows controlled movement of the tip by picometers, without which the atomic resolution would be entirely lost.

When operating the STM, the STM unit is hanging from three springs in its corners, which prevents most of the vibrations of the chamber from being transferred to the STM unit. However, the damping they supply is not enough to protect the STM from unusually large vibrations, so large vibration sources should be kept away from, or isolated from, the chamber.

The sample is fastened to the STM by sliding it under two flat springs on top of the STM unit, as seen in figure 2.3, which fix the sample to the unit.

The Approach of the Tip to the Sample

The tip is approached to the sample with the help of a linear motor, which is seen in figure 2.3. It consist of three cylindrical piezoelectric elements; an upper, a middle and a lower one. The tip is placed on top of the scanner tube, which is mounted on top of a rod that goes though the linear motor (See figure 2.3).

Piezoelectric element are characterized by the fact, that they expand and contract depending on the voltage applied to them. The upper and lower piezos will expand and contract in the horizontal plane, while the middle piezo expands and contracts in the vertical plane. This is what makes the
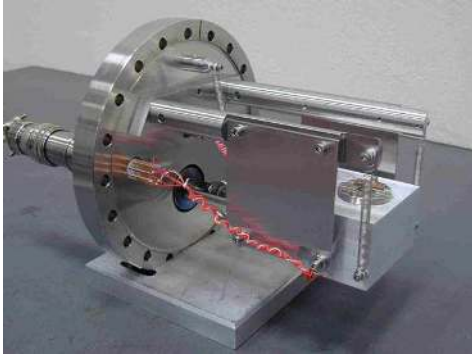
Figure 2.2: The STM unit. The STM is the small cylinder inserted in the block hanging from springs.
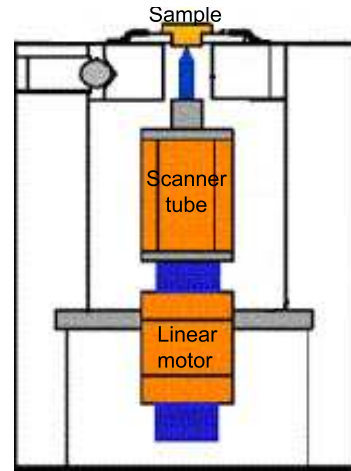

Figure 2.3: A sketch of the STM with a sample inserted at the top. The lines across the scanner tube and linear motor indicate the boundaries between the piezoelectric elements they consist of.

linear motor work.

The linear motor moves the tip up in the following way: First the lower piezo is clamped, holding the rod. The upper piezo is unclamped and middle piezo is contrated. This moves the rod upwards [54]. Then the upper piezo is clamped, the lower piezo unclamped and the middle piezo expanded. This expands the nanoworm, while keeping the rod in position and bring us back to the first step. Repeating these steps a sufficient number of times brings the tip up to the surface of the sample.

To avoid a collision between the tip and the sample, a desired tunneling current is set in the software. A feedback loop, in the electronics controlling the STM, measures the tunneling current during tip approach and stops the tip movement, when this current is obtained. Finally the piezos are relaxed, while maintaining the distance between the tip and the surface of the sample and the STM is ready to scan the tip across the surface.

Scanning the Tip Across the Surface of a Sample

When the STM unit is disengaged and the tip brought close to the surface of the sample, the STM is ready to scan the tip across the surface. The scanning movement is performed by the scanner tube. The scanner tube is a hollow cylindrical piezoelectric element, consisting of four sheet electrodes each covering a fourth of its circumference, as indicated in figure 2.3.

The tube is bend in the x-direction by applying opposite voltages to the two opposing electrodes that are parallel to this direction[54]. Similarly, it is bend in the y-direction by applying an asymmetrical voltage on the two other electrodes. The length of the tube is altered by changing the voltage on the inside of the tube, thus elongating or contracting the entire tube.

For the horizontal movement (in the xy-plane), a voltage is supplied from the computer and a range of the deflection is set to either 0, 1 or 2. An attenuator, which is basically a variable resistance, scales the voltage to the voltage needed to deflect the scanner tube, within the chosen range of deflection. The voltage from the computer is supplied through a digital port with a limited number of bits. Thus the voltage signal can only take a given number of values, and as the voltage is scaled the separation between the possible values is also scaled. A large deflection range, corresponding to a large voltage range, results in a relatively poorer spatial resolution of the movement than a small deflection range. This means that the lowest possible deflection range for a given image size should always be chosen to give the best possible resolution.

The prediction of the deflection corresponding to a certain voltage is approximated by two third order polynomials, which are used in two different deflection ranges and together constitute the algorithm for predicting the required voltage. This model works quite well[54]. However it can't counteract effects like the creep of the piezoelectric material, which stems from the fact that there is a small time constant on the expansion of the piezos, when a voltage is applied, nor can it counteract heat-induced drift[54]. Fortunately, these effect are easily identified when scanning, the first as a twisting in the first image after a large movement of the tip and the second as a movement of the scanned area from scan to scan although no movement was intended.

For the z movement, the computer supplies a voltage corresponding to the desired constant current and sets a variable called the gain. The voltage is fed into an amplifier, which amplifies this signal according to the gain.

This variable works by the same principle as the range of deflection for the xy movement. A small gain gives a large deflection range. As with the range, choosing the gain is a trade off between a large deflection range and a high resolution of the z-motion. A high gain is required to avoid driving the tip into the sample, when there are large differences in the heights of the sample, whereas a small gain is needed to get a good resolution of the STM image.

The deviation of the tunneling current from the desired level scales the signal once more, either lowering the voltage on the piezos, if the current is too high, or increasing the voltage, if the current is too low. The sensitivity with which the STM should react to a change in the tunneling current is adjusted with a second gain parameter. A high value of this parameter makes the STM track the tunneling current very closely and a low value corresponds to running the STM in constant height mode. The largest possible value should always be chosen when scanning in constant current mode, but it may be necessary to lower the value slightly, if an resonance frequency is observed in the images.

Acquiring a Good Tip

When scanning with the STM it is essential to have a sharp tip. If one atom on the tip is 1Å closer to the sample than the rest, it will carry 90% of the current. This is the way of obtaining sharp images. However, acquiring this state of the tip is not straight forward.

In the work presented here a W tips have been used. The tips are made by electrochemical etching of a W wire in a NaOH solution. This should produce a sharp tip. The sharpness of a tip is checked by microscope before putting it in the STM, but at the level that is important for tunneling, the tip curvature can of course not be resolved by optical microscopes and one simply has to hope for the best.

Once the tip is installed in the STM, several things can be tried to improve the state of the tip. None of them are a sure way to success, and the process of getting a good tip is often a mixture of patience and luck. With the Aarhus type STM tips cannot be exchanged in UHV and it is therefore usually worth the effort to improve on a tip once it has been installed.

The methods are more or less drastic, and typically, the more drastic they are the, more effective they are. Thus we would typically make an assessment of how bad the tip is, and start with the less drastic approaches relevant to its state. In the order from less to the more drastic the methods

are: Giving it time to recover, moving to different area, reversing the polarity of the tunneling voltage, increasing the tunneling voltage for a period of ten seconds, increasing the tunneling voltage for a longer period, dipping the tip into a metallic surface, using a high voltage method and finally opening the chamber and replacing the tip. There is a reasoning behind each method, but exactly what is going on is not fully known nor understood. There is an element of chance involved in restoring the tip.

Giving the tip time and moving it is done in the hope that any atoms, it might have picked up, will fall of. To increase the chances of any atoms falling of, the polarity of the tunneling voltage can be reversed, disturbing the system. Increasing the tunneling voltage is done in the hope of either ripping atoms of the tip and onto the surface or from the surface onto the tip. Increasing the time in which this is done, combines this method with the "give it time" approach.

Dipping the tip into a metal surface on purpose is a slightly drastic yet relatively effective method of improving the tip. The tip is dipped into the surface while measuring the current as a function of the height of the tip. The height, to start and stop the tip at, can be chosen, and the height is then changed in a steady movement up and down. When a (hopefully) good tip is achieved, the tunneling current should suddenly increase, when the tip is moved towards the sample, and suddenly decrease, when the tip is moved away from it. The height, at which the current, increases should be larger than when it decreases and the difference in current before and after the in/decrease should be of the order of 10nA-20nA.

The high voltage method is essentially the same method as the method mentioned above, where the tunneling voltage is increased. The difference is that using this method, the voltage is increased to higher voltage by an external source. As high voltages are not desirable in the STM, the method should be considered a last resort before having to replace the tip and it is very rarely used.

When all the methods mentioned above have failed to improve a poor tip, the only choice left is to open the chamber and replace it. This is of course a timely process and in addition to this, tips are not in abundance as they are difficult to produce.

2.2.2   STM Images

Acquiring Good STM Images

Acquiring good STM images requires a number of factors to be considered. STM images in their nature are very local snapshots of the state of a surface. Therefore one needs to ensure that the images taken are representative. To do this, large overview images should complement smaller close up images of the surface. Also, images should be made of several different areas of the sample. To ensure the validity of the images the general features seen in the images should be observed repeatedly in successive images, but only once within one image, as a repetition of the image features indicates a double tip. Also the scanning speed should be varied for comparison of images to ensure that periodic structures (e.g. atomic lattice patterns) are real and not simply periodic noise signals.

When scanning the highest possible vertical and horizontal resolution achievable should be used. This involves both considerations of the range and gain as above, but also a consideration of the size of the image relative to the number of pixels in it. When scanning, the scanning program allows the images scanned to have a number of different pixels. We have traditionally scanned 256×256 pixel images, as these are acquired reasonably fast and the program shows four consecutive images when scanning in this size, easing the comparison of images while scanning. However, if small details are wanted in large images, such as e.g. atomic resolution on a $200\text{\AA} \times 200\text{\AA}$ scale, a larger number of pixels are needed. This can be achieved as 512×512 pixel images can be scanned. When scanning in this size, the program only shows one image on the screen, making comparison of images harder and at the same time causing the image acquisition to be slower.

Finally, to achieve good resolution the right scanning parameters should be chosen. To obtain highly resolved images a sharp tip is needed and the tip-sample distance should be small, i.e. the tunneling resistance low [48]. That means that the tunneling parameters influence the images such that low voltages and high current should give the best resolution. The highest resolution is therefore obtained when the tip is very close to the sample and the currents fairly high, which also means that these tunneling parameters offer the greatest chances of tip-surface interactions. Depending on the system this may or may not need to be a concern when scanning.

Interpreting STM Images

When scanning the tip across the surface, the local density of states at the fermi level of the surface is mapped out. This map is the STM image. If always keeping in mind, that what is actually seen is the density of states, one can describe the image as the topography of the surface. This is often a fair approximation and it eases the basic interpretation of the images.
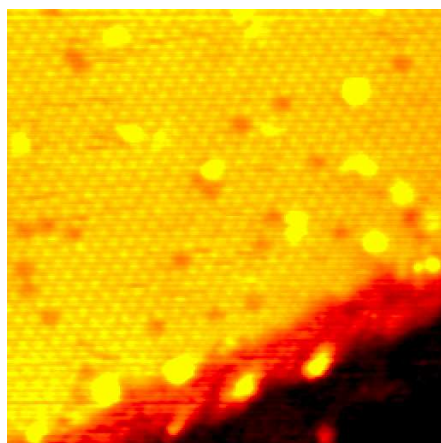

Figure 2.4: A 130Å×130Å STM image showing the features observed in the STM images presented in this work; terraces, steps, atomic lattice pattern and isolated protrusions and extrusions.
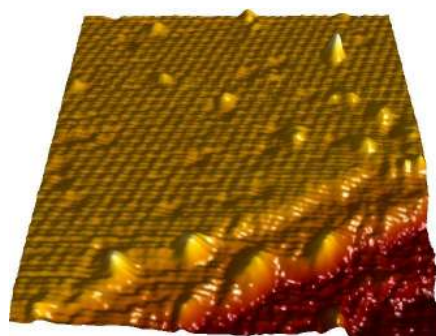
Figure 2.5: The image from figure 2.4 represented in a 3D fashion to illustrate the meaning of the interpretation of the images as the topography of the surface.

In figure 2.4 an STM image is seen. The color scale goes from black, representing low parts of the image, through red to yellow, representing high parts of the image. The image has been chosen as an example, because it contains all the features seen in the STM images presented in this thesis; terraces, steps, atomic lattice pattern and isolated protrusions and extrusions. In the image, a terrace is seen, on the upper left half and three steps are seen in the lower right half of the image, as lines across which the color changes rapidly. On the terrace an atomic lattice pattern is clearly visible as a hexagonal mesh of circular protrusions. Isolated protrusions appear as bright yellow spots, both on the terrace and the steps and small depressions are seen as small dark spots on the terrace. To further illustrate what this

traditional version of an STM image shows, figure 2.5 is the same image represented in a 3D fashion. Here protrusions and depressions appear as such and the structure of the stepped part of the image appears clearer. This representation of the images naturally infers the view of the images as topographic images in ones mind, and it is therefore important to stress that the image represents the local density of states and that the depressions and protrusions may not be topographic features of the sample, but local depletions and enhancements of the density of states. The advantage of the 3D representation is that is shows details that one may otherwise not see due to the limitations of the color scale in normal images as e.g. the structure of the protrusions in this case.

Data representation

When an STM image is acquired, it is rarely free of small amounts of noise and the surface is often tilted slightly with respect to the STM. Therefore raw data often needs filtering. This can be done fairly easily using STM image processing programs.

The tilting of surfaces is a result of a small misalignment between the natural scanning plane of the piezo motor and the plane of the surface of the sample. The image tilt may be corrected by STM software. Careful tilt-correction is important when measuring apparent heights in an image. On the other hand, a tilting of the surface may at times be helpful in displaying STM images, as tilting may allow details on several terraces to be seen as is the case in figure 2.4.

The raw data behind figure 2.4 is seen in figure 2.6. In figure 2.7 the same image is seen after it has been smoothened by averaging each data point relative to the nearest neighboring points. As seen smoothing removes the line noise of the image and it will also reduce irregular noise patterns. If a regular noise pattern is seen, this may be removed by fft-filtering, removing the corresponding peak in the fourier transform of the image and performing an inverse transform to obtain the filtered image. There are many filtering techniques available as the knowledge from general image processing can be used in the filtering of STM images. Filtering is a balance between representing the data nicely and staying true to the data by not removing to much of the original information in data. When choosing to filter the image it is important to be aware of this balance, and applying filtering only to a degree where the actual features of the image are not compromised or distorted by the attempts to enhance them.
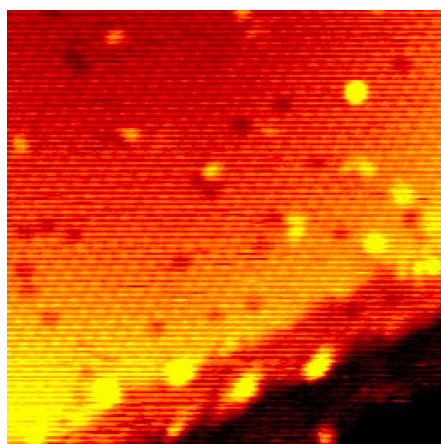
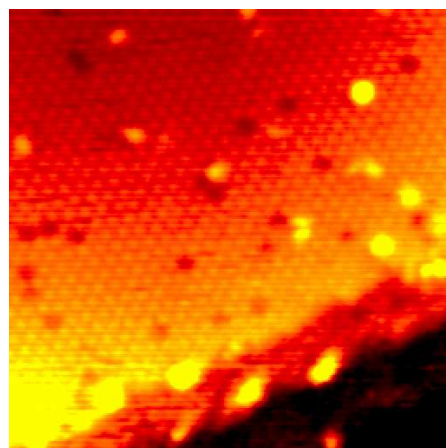Figure 2.6:   The raw data used to create the image in figure 2.4.

Figure 2.7:   Image 2.6 after noise reduction has been performed by averaging each point relative to its nearest neighbors.

Calibrating STM images

The lengths and heights measured on an STM image need calibration, as they depend on the length of the tip used when scanning and the characteristics of the piezo elements of the scanner tube.

To calibrate the vertical distance measured, a feature with a well known height is needed, i.e. a feature is needed where the height measured is the height of the feature and not an apparent height. Such a height will often be available in the form of a step on a clean surface.

The horizontal calibration requires the measurement of a well known horizontal distance. Here an atomic spacing of the substrate is often used. The horizontal calibration is typically different in different directions, which should be considered. The horizontal calibration may be performed in real space by measuring a number of atomic spacings, but where possible calibration by using fourier transforms of the image is preferable, as this typically averages over more data than the real space measurements.

Usually the uncalibrated image sizes are quite close to the actual image sizes and therefore calibration is usually not necessary unless high precision is required, e.g. if atomic distances are measured.

2.3 Electrochemical activity measurements

This section serves as a short introduction to the electrochemical measurements presented in this thesis. All electrochemical measurements were made by Thomas F. Jaramillo.

The activity for hydrogen evolution is measured by measuring the current resulting from voltage sweeps in an electrochemical cell. As the voltage is swept in a negative potential window, a current will start to flow generated by the hydrogen evolution reaction. The current will increase exponentially with the voltage as illustrated in the left side of figure 2.8. To extract the exchange current density at zero potential, the current measured is fitted to the Tafel equation $i = i_0 e^{-\beta\eta F/RT}$, where η is the overpotential [15]. By extrapolating this fit to zero overpotential the exchange current density i_0 is found as illustrated on the right hand side of figure 2.8. Naturally, when comparing the extrapolated exchange current densities from different samples it is important that they have very similar Tafel slopes, i.e. the slope of the fitted data in the right half of the figure, as the extrapolation results in small deviations of slope having large impact on the found exchange current densities.
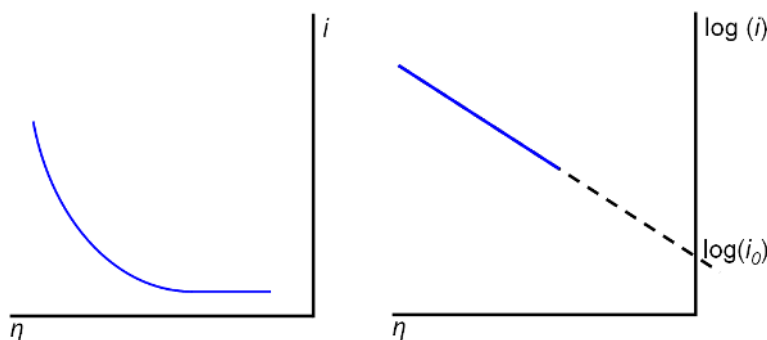

Figure 2.8: An illustration of the principles behind extracting the exchange current density from the measured current of a negative voltage sweep in an electrochemical cell.

The cell used in the measurements presented in this thesis is designed to only expose the top facet of the samples from the UHV chamber to the electrolyte to ensure that only the well-characterized part of the sample contributes to hydrogen evolution. The cell itself is simply a teflon beaker in the bottom of which a hole has been drilled. By sealing this with a viton

o-ring onto the surface of the sample, only the 0.10cm^2 center of the top facet of the sample is exposed to the electrolyte solution. The measurements are performed in a H_2SO_4 electrolyte solution, which serves to provide an excess of protons available for the reaction. The overpotential used in the Tafel equation is relative to the Normal Hydrogen Electrode (NHE) which is a standard in electrochemistry. In practice this is inconvenient to work with and during measurement, the voltages are instead held relative to a Saturated Calomel Electrode (SCE) and subsequently can be converted to voltages relative to the NHE.

Chapter 3

MoS$_2$ on HOPG

In this chapter the nanoparticulate MoS$_2$ catalyst is studied in a MoS$_2$ on HOPG model system, which is a very realistic model system as graphite in more rough forms are other used as substrates in electrochemistry [16]. The model system is also interesting as interesting in the HDS reaction where MoS$_2$-based carbon supported catalysts have shown high activities [55–58]. In this work, the HOPG is etch pit modified to allow better pinning of the nanoparticles to the substrate and the morphology of the nanoparticles is studies by STM.

3.1 Sample preparation

3.1.1 Substrate preparation

Graphite is a layered material consisting of sheets of covalently bound C in a hexagonal lattice, which are held together by van der Waals forces as seen in figure 3.1. The graphite layers are very inert and HOPG is therefore simply cleaned by scotch tape cleaving it in air. This peals of the top layers of the graphite, exposing a very flat graphite surface as seen in figure 3.2. The graphite layers stack such that every second atom in the top layer is directly on top of an atom in the layer below (A type) and the others are directly above the center hollow between six atoms in the next layer (B type) as seen in figure 3.1. This is reflected in STM images of the surface as seen in the inset in figure 3.2; As the B-type atoms are imaged as protrusions whereas the A-type are imaged as hollows, the spacing between protrusions in atomic scale images of the HOPG surface is 2.46Å [59–61].

Depositing nanoparticles on the flat HOPG surface, the particles bind very weakly to the plane of the sheets and agglomerate at defects such as
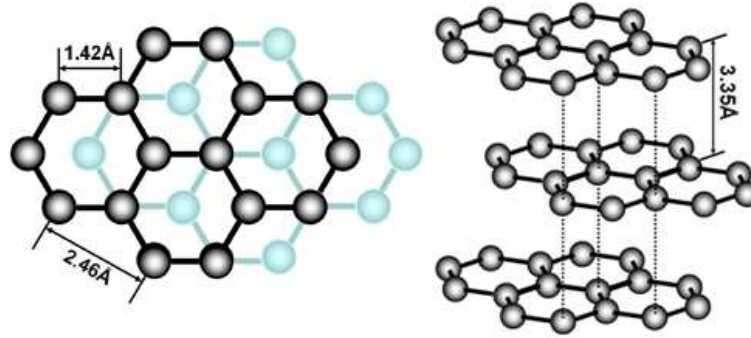
Figure 3.1: The structure of HOPG. Left: top view of the basalplane of HOPG, illustrating the positions of the atoms in the second layer relative to the top layer. The C-C distance in the plane is 1.42Å and the in-plane lattice constant 2.46Å. Right: The stacking of HOPG layers. The layers are separated by 3.35Å [48].

steps, as could be expected from such an inert surface. The particles that remain on the plane will easily be moved by the interaction with the STM tip [62]. The stronger binding to the steps of the graphite can be utilized to pin the clusters to the surface by inducing etch pits in the HOPG surface [62–64]. Etch pits are single layer holes formed by oxidizing surface defects in the graphite, basically inducing increased step density on the surface. Etch pits have been long known to form in graphite [65] and their formation is well-characterized [66].

In this study, etch pits are formed by sputtering the HOPG surface lightly with 160eV Ar$^+$ ions for 20 seconds at a flux resulting in a chamber pressure of $1.5 \cdot 10^{-7}$Torr and subsequently heating it to 630°C for 5 minutes in air. The air reacts away the graphite from the defect and not the intact graphite plane, creating an etch pit. The HOPG is heated by placing it on a resistively heated Si wafer, which acts as a hotplate and heats the HOPG sample. The temperature is monitored with a thermocouple on the back of the Si wafer. The resulting HOPG surface is always etch pitted, although the extend of the pits vary. Figure 3.3 shows an etch pitted HOPG surface with intermediate sized pits.

Reintroducing the sample into vacuum, it is annealed to 600°C degrees to desorb any adsorbates from the background and the sample plate, achieving a clean HOPG surface, which is ready for MoS$_2$ deposition.
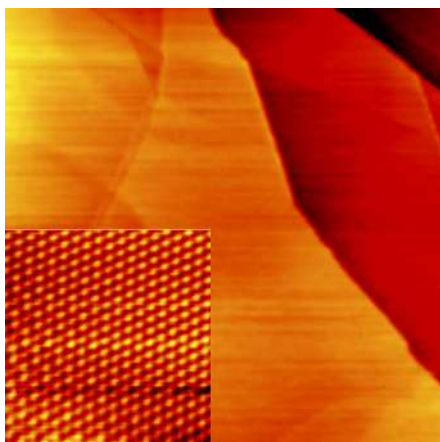
Figure 3.2: STM image of cleaved HOPG showing the flatness of the cleaved HOPG on a large scale. Inset: Atomically resolved area of the HOPG surface. Large image: 10000Å x 10000Å, 1.0nA, 525mV Inset: 50Å x 50Å, 0.64nA, 363mV
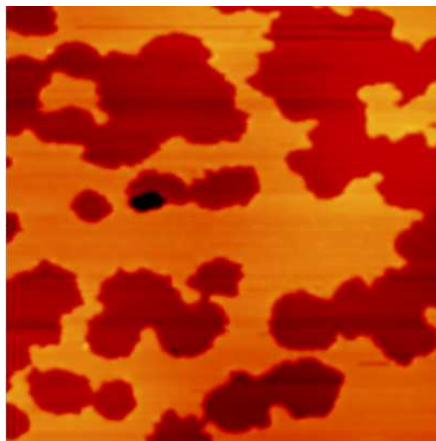
Figure 3.3: STM image of etch pitted HOPG showing medium sized pits. 1000Å x 1000Å, 0.4nA, 526mV

3.1.2 MoS$_2$ preparation

MoS$_2$ is synthesized on the HOPG surface by physical vapor deposition of Mo in a background pressure of H$_2$S and subsequent annealing in the same H$_2$S atmosphere. The synthesis is performed immediately after pre-annealing the HOPG to desorb any background adsorbates. As the sample is cooling and reaches 177 °C, H$_2$S is backfilled into the chamber to a pressure of 10^{-6} Torr. When the sample temperature has further dropped to 147 °C, Mo is deposited. The sample is then allowed to cool to 100 °C, before it is annealed to allow the particles to crystallize. After this annealing, the H$_2$S leak valve is closed when the sample has cooled to 95 °C. This preparation procedure is taken directly from the STM studies of MoS$_2$ on Au in the Besenbacher group [38, 67], where an annealing temperature of 400°C for 15min was used.

The preparation procedure is illustrated schematically in figure 4.1. As a starting point we used exactly the same preparation procedure as had been used by the Besenbacher group. In later experiments the Mo dosing
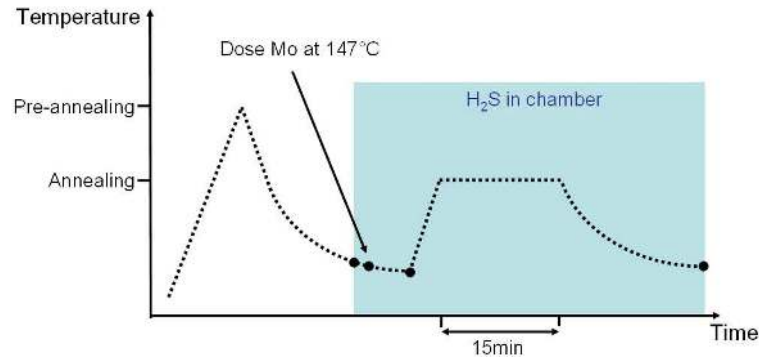
Figure 3.4: The MoS$_2$ preparation procedure. The sample is heated to the pre-annealing temperature, typically 600°C, and while cooling H$_2$S is let into the chamber at 177°C, Mo dosed at 147°C and the sample further cools to 100°C. Then the sample is annealed at the annealing temperature for 15min and when cooled to 95°C the H$_2$S leak valve is closed. The dots represent temperatures that are not changed when changing the preparation parameters.

rate and annealing temperature where adjusted, but the general design of the preparation procedure was maintained. It should be noted here that when changing the annealing temperature, the pre-annealing temperature was always kept at least as high.

The Mo doser is homemade and based on resistive heating of a Mo filament made from a 0.5mm, 99.95% Mo wire. The Mo filament is thoroughly outgassed and the cleanliness of the evaporated Mo is checked by XPS. The rate of the Mo doser was determined before each deposition using a Quartz Crystal Microbalance (QCM). After outgassing, the Mo wire becomes very brittle and therefore great care is taken to avoid any strain when mounting the filament in the doser. Also, another identical Mo doser was added to the chamber in order to minimize the number of bakes due simply to a broken Mo filament. An E-beam doser, where a Mo rod is heated by electron bombardment, would not be as affected by the problem of the brittleness of the Mo. However, the choice to use the filament based doser despite this drawback was made because HOPG is very easily sputtered and this type of doser would create the risk charged Mo ions that would not land softly on the HOPG surface but rather go deeper into the HOPG structure, which was not the intension here.

The H$_2$S is supplied from an N25 purity bottle supplied by Air Liquide. It's purity was checked with the mass spectrometer.

The preparation procedure was initially tested on a Au(111) sample, to ensure that the MoS$_2$ structure seen in [38] was reproduced. As seen in figure 3.5 this was the case; the MoS$_2$ nanoparticles are flat, primarily triangular particles, with the characteristic edge state on the particle perimeter.
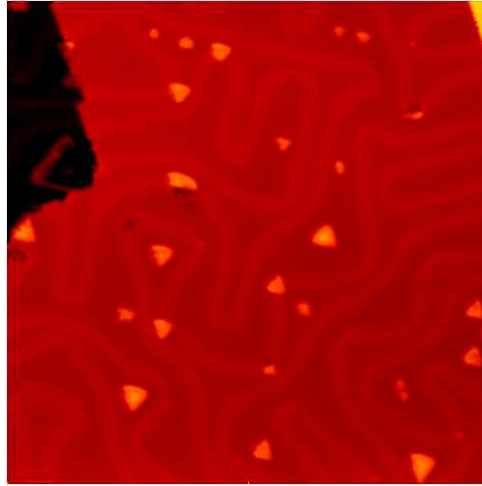

Figure 3.5: STM image of MoS$_2$ on Au(111) from a test of the preparation procedure showing single-layered triangular MoS$_2$ nanoparticles. 500Å x 500Å, 0.6nA, 312.5mV

3.2 MoS$_2$ morphologies on HOPG

MoS$_2$ nanoparticles were initially prepared on HOPG in the same way as it had been done on Au(111). The resulting morphology, however, was very different, with large particles, which looked non-crystalline in their structure, as seen in figure 3.6. The particles typically appear to be 3-4nm across and 1-1.5nm high.

Technically, scanning the particles requires great care as the particles are easily picked up by or swept away by the tip when scanning to closely or too fast. The effects are clearly seen when scanning, tip changes are very frequent and particle removal events are seen by the disappearance of the particle from one scanning line of the image to the other. To minimize this, care must be taken when scanning. The scanning speed should be kept
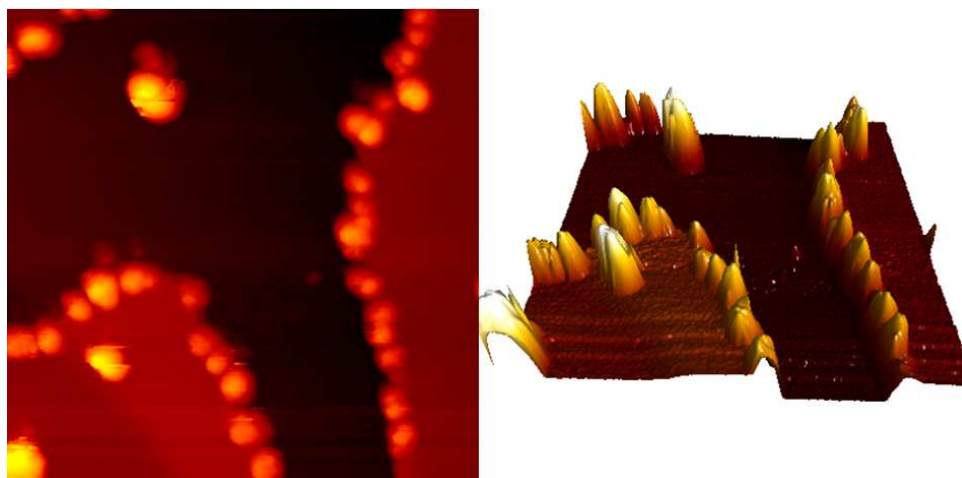
Figure 3.6: STM image of MoS$_2$ on etch pitted HOPG from the initial sets of experiments. On the right a 3D representation of the image is seen where the height is scaled by 5 compared to the horizontal scale. 500Å x 500Å, -0.7nA, -1995mV

very low to allow the best possible chances for the STM to react to changes in height and relatively high tunneling voltages and low tunneling currents should be used to have larger tip-sample distance and weaker tip-particle interaction. This is a trade-off between minimizing the tip interactions with the surface so that it does not disturb the surface and keeping sufficiently strong interaction to ensure that the details in the images are still seen.

The image in figure 3.6 represents this balance. The tunneling parameters are gentle enough that particles are rarely moved, but the shapes of steps of the HOPG surface are still reasonably resolved. The particle shapes observed, however, are somewhat different from the triangular flat particles seen on Au(111).

The sulphidation of the particles should be ensured by the ratio of H$_2$S to Mo impinging on the surface. The Mo dosing rate corresponds to $\sim 1 \cdot 10^{-3}$ ML/s and the H$_2$S background pressure of $1 \cdot 10^{-6}$ Torr corresponds to 1 L/s, which should provide an H$_2$ excess which secures sulphidation of the Mo. The composition of the particles could not be checked by XPS as the focussing of the hemispherical analyzer was malfunctioning, resulting in very poor signal and a large signal from the area around the sample, where a Mo housing and a Ta sample plate contributed to XPS lines on top of where the

MoS$_2$ lines would lie. As the Mo and H$_2$S purity had been confirmed and the MoS$_2$ was reproduced on Au(111), MoS$_2$ should be formed on the HOPG surface. To further ensure ourselves that the particles observed were MoS$_2$ we reconfirmed the formation of the known morphology on Au(111) and lowered the Mo dosing rate to $\sim 1 \cdot 10^{-4}$ ML/s in the following experiments.
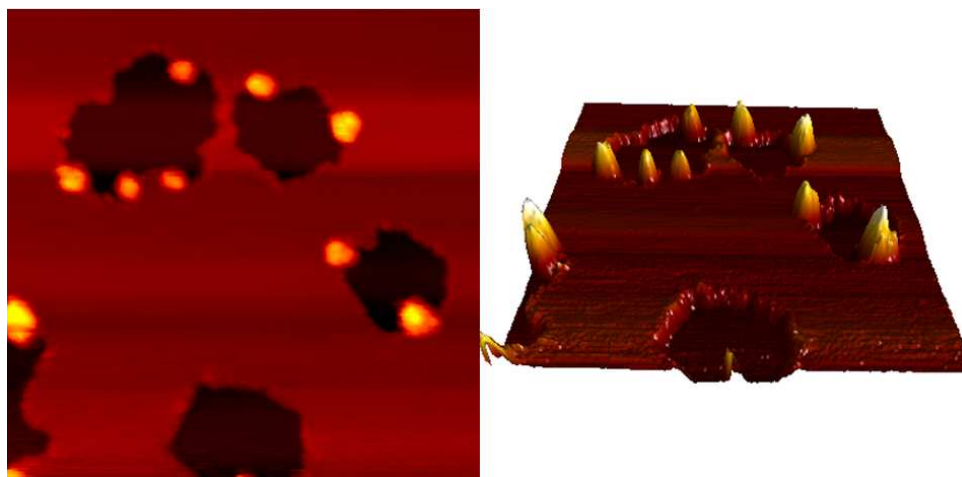

Figure 3.7: STM image of MoS$_2$ on etch pitted HOPG at lower coverage using a lower dosing rate. On the right a 3D representation of the image is seen where the height is scaled by 5 compared to the horizontal scale. 500Å x 500Å, -0.2nA, -1000mV

In figure 3.7 MoS$_2$ nanoparticles on HOPG which have been synthesized with the lower Mo dosing rate and a lower coverage to make the particles better separated are seen. The particle separation made the tip changes fewer and ensured that the particles were not overlapping each other improving the chances of resolving their shapes. However, the apparent particle shapes and sizes are unchanged by these changes. The particles observed were therefore concluded to be MoS$_2$ and their shapes more closely examined.

A closeup of these particles is seen in figure 3.8 along with a line profile across a graphite step and one of the particles in figure 3.9. As seen in figure 3.8, the particles lie against the HOPG steps and are very steep with slopes comparable to that of the steps. The particles have slightly elongated shapes which seem to follow the step although the irregularity of the step profile makes it hard to determine exactly. The line profile in figure 3.9 reveals that the slope of the particles is indeed comparable to that of the
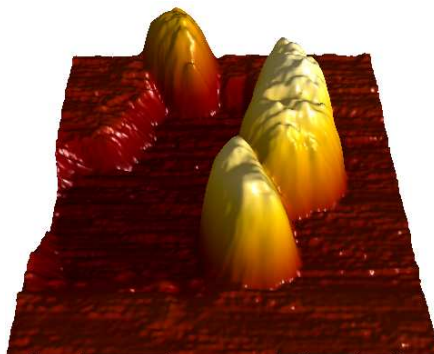
Figure 3.8: A closeup STM image represented in 3D of MoS$_2$ on etch pitted HOPG. 200Å x 200Å, 0.2nA, 1.0V. The height is scaled by 5 compared to the horizontal scale.

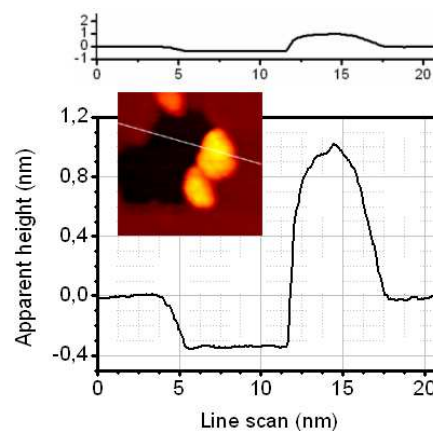Figure 3.9: Line profile across a MoS$_2$ particle and HOPG pit as indicated in the inset image. Top: The height and line scan scales at 1:1 ratio. Bottom: Expanded height scale showing details of the profile.

step and that they are reasonably flat although an entirely flat basalplane is not imaged. The apparent particle height is 1.3nm corresponding to the geometric height of 2-3 MoS$_2$ layers [31].

The slope of the HOPG step, clearly shows that observed particles shapes are convolutions of the real particle shapes and the shape of the tip. Such convolutions are well-known and may lead to large overestimations of the particle size and large deviation between the imaged particle shape and the real particle shape [62]. Taking the slope of the steps as indicative of the added slope to a vertical step by the tip-convolution of its shape, one may speculate on the deconvoluted shape of the particle. With such considerations, a closer look at the line profile in figure 3.9 indicates that the particles have vertical sides and a width in the range of 2nm. The particle size is therefore in the same range as those observed in industrial MoS$_2$ catalysts [37, 68].

To further investigate the particle shapes, a flatter or simply larger morphology of the particles or a stronger pinning of the particles to the surface was needed, such that the tip convolution would not dominate the apparent particle shapes. In the literature, three different approaches were identified

to possibly achieve this: Studies of both Au and Ru nanoparticles on etch pits had shown that by making the nanoparticles large enough to fill the etch pits, they would be pinned to the surface and start to grow to large flat morphologies [63, 64]. Unfortunately this would lead to very large particles, tens of nanometers wide, which would less resemble the particles in industrial catalysts, and this option was therefore discarded. Studies of large MoS$_2$ crystals on HOPG by Li et al [69, 70] had shown that a morphology of layered MoS$_2$ would spread out and flatten with annealing to high temperatures in H$_2$S. And finally, studies of Ag nanoparticles on sputtered HOPG had shown that the particles were pinned more strongly to such a surface than to an etch pitted surface [62, 71]. These latter two approaches of sintering at high temperatures in H$_2$S and sputter defecting the HOPG to further pin the particles seemed appealing and we therefore decided to explore both routes.
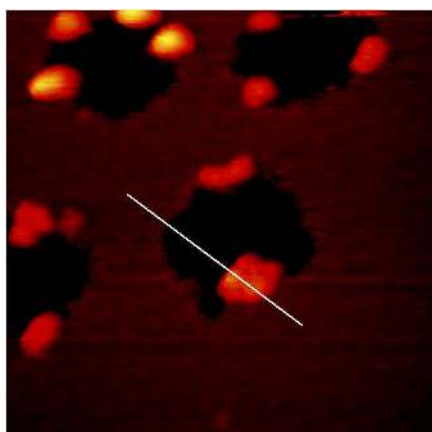
Attempts to achieve resolvable particle shapes

Figure 3.10: STM image of a MoS$_2$ sample prepared with an annealing temperature of 650°C. The line is the basis of the line profile in figure 3.11. 500Å x 500Å, 0.6nA, 526mV
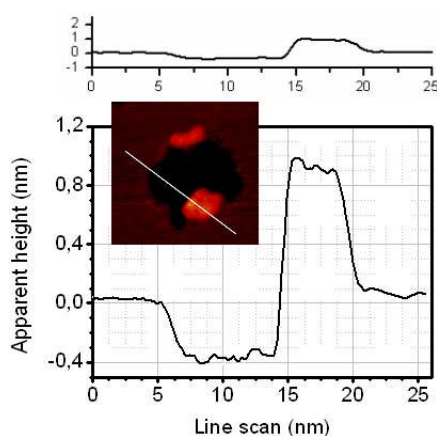

Figure 3.11: Line profile across a MoS$_2$ particle and HOPG pit as indicated in the inset image. Top: The height and line scan scales at 1:1 ratio. Bottom: Expanded height scale showing details of the profile.

Sintering the particles to temperatures as high as 1000 °C after deposi-

tion or by elevating the annealing temperature in the preparation procedure yielded no major changes in the average size or height of the observed particles. Occasionally particles were seen on which a flatness of the particle top could be observed as seen in figure 3.10, but these were very rare and their basalplane shape still not resolvable. A line scan across such an island which had been annealed to 650°C during the preparation procedure is seen in figure 3.11. As the particle size and apparent height is approximately the same for particles prepared without the elevated temperatures, one might speculate that the flatness of the top of the particles is seen due to an improved crystallinity. However, annealing temperatures had been used up to 1000°C, and no indications were seen that the number of these very few particles with clearly flat top planes was increased with the increased annealing temperatures.
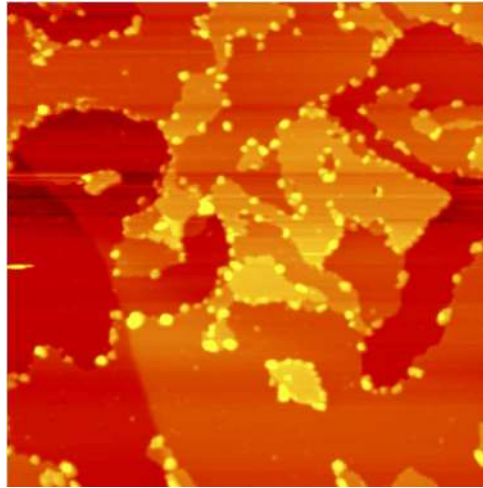

Figure 3.12: STM image of MoS$_2$ on sputtered etch pitted HOPG. The sputtering after etch pitting was 4 times the sputtering used in the etch pitting procedure. 2000Å x 2000Å, -0.5nA, -998mV.

Whatever the annealing temperature used, if the scanning parameters were changed to increase the resolution of the finer details of the particles however, they would be moved by the tip.

Providing better pinning to the substrate was therefore also necessary to obtain resolvable particles. Initially we simply sputtered an etched HOPG sample before deposition before MoS$_2$ deposition, creating a surface with both defect types for nucleation. The resulting morphology is seen in fig-

ure 3.12. The particles seem to prefer binding to the steps rather than the sputter defects, which are also very few in the image. This lead to an investigation of the influence of the pre-annealing on the sputter defects, which turned out to be healed to a large extent during this part of the preparation procedure, meaning that the sputter defecting should be performed immediately prior to the Mo deposition to provide a reasonable sputter defect density for the MoS_2.

3.2.1 Ending our experiments

Unfortunately, during these experiments we experienced major STM failure as the coarse movement stopped working. After many replacements of parts and repeated failure of the coarse movement subsequent to H_2S eposures, it was concluded that the inchworm was somehow corroded by H_2S such that after one or only a few exposures to H_2S it would stop working. This was surprising, as the STM is an Aarhus STM from the Besenbacher group who have not had this problem with their STM in their MoS_2 studies on Au. However it turned out that our STM was a newer generation of the Aarhus STM than the one used for those studies, and that a new material had been taken into use in the inchworm, explaining the difference in the H_2S tolerance of the two instruments. It appeared that we had simply by chance started out with an inchworm that had a relatively high tolerance although it had this inherent weakness, and that we were not so lucky with the replacement parts we had used in the repairing process.

Meanwhile we were aware made that the Besenbacher group had also taken up the studies of MoS_2 on HOPG and had gotten the very first images of a hexagonal shape on a basal-plane bonded MoS_2 island on HOPG. The images obtained by the Besenbacher group showed that the basic structure of MoS_2 on HOPG was as the one known from studies on Au(111) and we therefore stopped any further studies of MoS_2 on HOPG at this point and refocussed attention to linking structure and activity of MoS_2 for hydrogen evolution by studying MoS_2 on the Au(111).

The results from the Besenbacher group has recently been published [72]. They have used a heavily sputter-defected HOPG surface as a substrate. They observe two different morphologies of the MoS_2 nanoparticles. An annealing temperature of 730 °C yielded single layered and hexagonal MoS_2 nanoparticles with the conducting edge state clearly seen in the images. Annealing to 930°C the particles observed are multilayered with 2-5 layers, but still hexagonal with a conducting edge state. The results from the Besenbacher group thus confirmed that the route we were taking of sputter-

defecting and increasing the temperature would have let to more resolvable particle shapes and sizes had we not been stopped the unfortunate STM corrosion problems and at the same time verified that the MoS$_2$ particles observed on Au(111) are analogous to these observed on the more realistic HOPG substrate.

Chapter 4

MoS$_2$ on Au(111)

In this chapter the nanoparticulate MoS$_2$ catalyst is studied in a MoS$_2$ on Au(111) model system. The Au(111) surface provides much better conditions for scanning than the HOPG surface enabling highly resolved images of the nanoparticles to be obtained within a reasonable time frame and at the same time has a reasonably low hydrogen evolution activity. In this work, the morphology of MoS$_2$ is studied with STM and related to the hydrogen evolution activity measurements on the imaged samples.

4.1   Sample preparation

MoS$_2$ is synthesized on Au(111) by dosing Mo in a background pressure of H$_2$S and subsequently annealing in that same H$_2$S atmosphere. The Au(111) surface is cleaned by sputter annealing cycles. Immediately prior to MoS$_2$ deposition the Au(111) sample is heated to 650 °C to ensure a completely clean Au(111) surface. The preparation procedures for MoS$_2$ on Au(111) are illustrated schematically in figure 4.1. The procedures are completely analogous to the MoS$_2$ preparation procedure used in previous studies of MoS2 on Au(111) in the Besenbacher group[38] and the preparation procedure used on HOPG. Two different annealing temperatures are used, 400 °C and 550 °C, and in the following samples synthesis with the former annealing temperature will be referred to as the standard preparation and preparation with the latter will be referred to as the sintering preparation. Likewise, samples resulting from the procedures will be referred to as standard samples and sintered samples, respectively. In this context sintered is to be understood as further sintered as annealing to 400 °C may also cause some sintering.
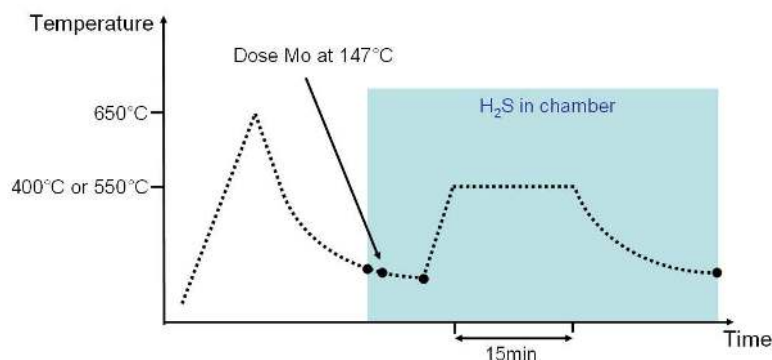
Figure 4.1: The MoS$_2$ preparation procedure. Prior to MoS2 deposition the sample is heated to 650°C. While cooling, H$_2$S is let into the chamber at 177°C and Mo dosed at 147°C before the sample further cools to 100°C. Then the sample is annealed for 15min at 400°C for the standard preparation or 550°C for the sintering preparation and when cooled to 95°C the H$_2$S leak valve is closed. The dots represent temperatures that are not changed when changing the annealing temperature.

The MoS$_2$ doser and the H$_2$S gas are the same as in the studies on HOPG. To minimize the harmful influence of H$_2$S on the chamber, H$_2$S is dosed through a directed doser which somewhat directs the H$_2$S flow from the leak valve onto the sample. The flow used is such that a background pressure of $1\cdot10^{-7}$ Torr is achieved. The H$_2$S exposure time is approximately 60-70 min.

The Mo dosing rates are determined by dosing Mo onto a second Au sample calibrating the Mo amount dosed by XPS. This is done to save time as the very low dosing rates made the rate determination with the QCM very time consuming. With XPS a less precise, but fair estimate of the dosing rate can be assessed much faster than with the QCM.

The preparation procedures both yield MoS$_2$ nanoparticles with the well-known features from previous studies of MoS$_2$ on Au [38, 67, 73]: primarily triangular flat nanoparticles with a bright edge state around the particle perimeter. This is seen in figure 4.2 and 4.3 which show STM images of MoS$_2$ nanoparticles synthesized by the two procedures.
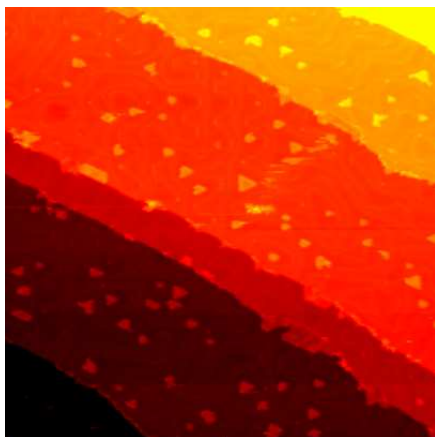
Figure 4.2: STM image showing the MoS$_2$ morphology on Au(111) from a standard preparation where an annealing temperature of 400 °C is used. 940Å x 940Å, 1.3nA, 4mV
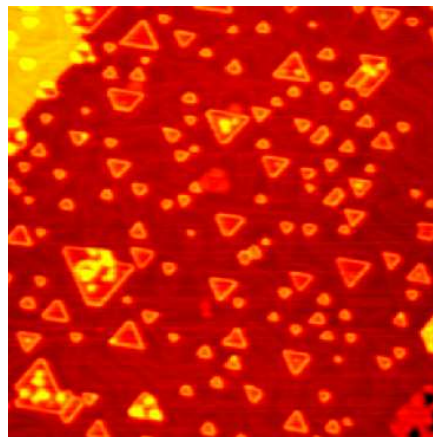

Figure 4.3: STM image showing the MoS$_2$ morphology on Au(111) from a sintering preparation where an annealing temperature of 550 °C is used. 940Å x 940Å, -1.2nA, 1.9V

4.2 The model substrate

The substrate of the MoS$_2$ nanoparticles is not simply a Au(111) surface. During sample preparation the Au(111) sample is subjected to H$_2$S and annealed herein, which may alter its surface. To investigate the effect on the Au surface of the H$_2$S exposure and annealing during MoS$_2$ synthesis, a blank sample was prepared by going through all the steps of the standard preparation procedure except that no Mo was dosed.

Figure 4.4 shows an XPS spectrum of this blank sample. The spectrum reveals no differences from a clean Au(111) surface. The inset shows the binding energy region of the S 2p line, but no sulphur is detected. Similar regions for O and C were also scanned showing that neither O or C is present on the sample. This leads to the suspicion that the substrate is no different from a Au(111) surface. However, measuring the hydrogen evolution on a clean Au(111) surface and the surface of the blank sample, a clear difference is seen. Figure 4.5 shows the hydrogen evolution on clean Au(111) and the blank sample. From the figure it is very clear that the activity of the blank sample is less than that of the Au(111) surface indicating that some of the active sites of the Au surface are blocked.

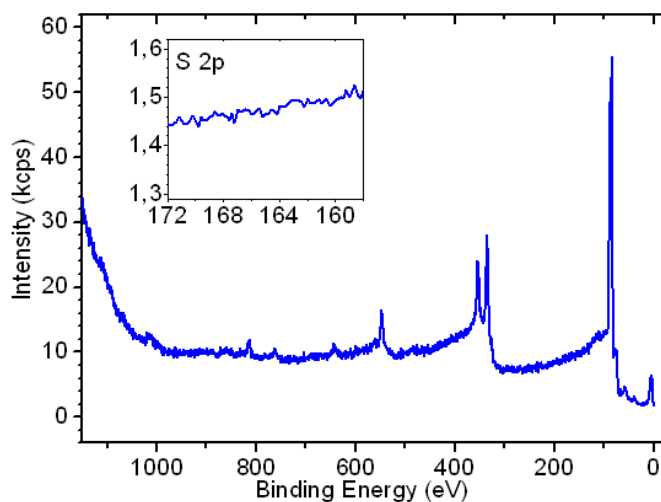Figure 4.4: XPS survey spectrum of a broad binding energy window for the blank sample. The peaks in the spectrum are associated with Au. The inset shows the binding energy region of the S 2p peak, showing that no peak is seen.
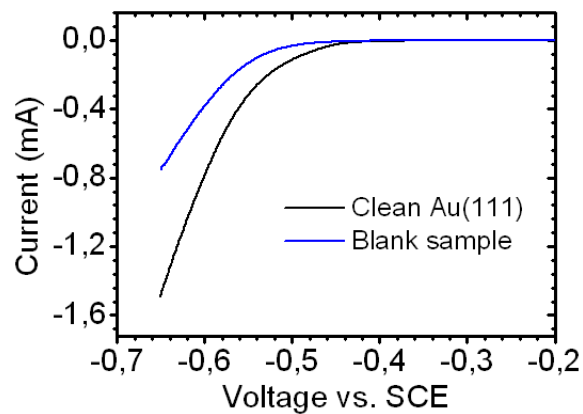

Figure 4.5: Polarization curves showing the hydrogen evolution in a cathodic potential window for a clean Au(111) sample (black) and the blank sample (blue). Sweep rate: 5mV/s.
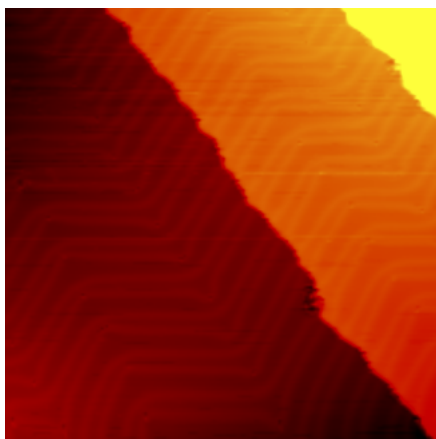
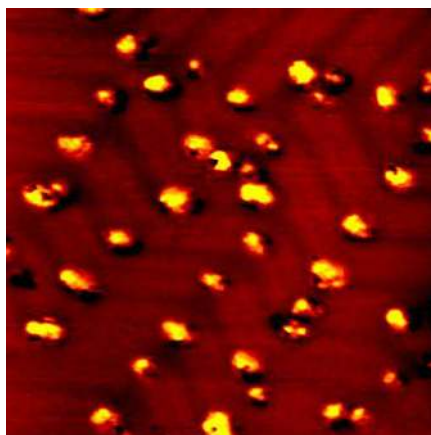Figure 4.6: STM image of the blank sample. The herringbone is regular and no adsorbates are seen. 660Åx660Å, 1.40nA, 969mV

Figure 4.7: STM image of Mo on Au(111). The Mo nucleates at the elbows of the regular herringbone reconstruction. 470Åx470Å, 0.52nA, 1051.0mV

To shed further light on this blocking of sites by something not detectable by XPS, STM imaging was invoked. Figure 4.6 shows an STM image of another blank sample. Surprisingly, the surface looks like a clean Au(111) surface. The herringbone is regular and no adsorbates are seen on either larger overview images or closeup images of the terraces and steps. The HER measurement was therefore repeated on this sample to rule out a difference between the two blank samples and the HER data in figure 4.5 were reproduced. H_2S desorbs from the Au(111) surface at temperatures of 100K-160K [74], which has previously been used in combination with the unchanged appearance of the surface to conclude that the H_2S does not influence the Au(111) during the preparation procedure [67]. However, H_2S has also been shown to desorb at 180K (with a shoulder in the hydrogen desorption at 350K) from a surface of Mo islands on Au(111), which does not mean that H_2S will not react with Mo on Au(111) at the temperatures of the preparation procedures.

The only conclusion that can be drawn is therefore that something is adsorbed in very small amounts on the Au surface during the preparation procedure of the blank sample and that this something blocks sites on the surface resulting in a significantly lower activity than on clean Au(111). One

may of course speculate that this something would likely be sulphur and that these blocked sites might be step sites, but no evidence of this is available.

The blank sample has another difference from the substrate seen in the images of MoS$_2$ on Au(111): The herringbone is un-distorted. The deposition of Mo onto the Au(111) does not account for this distortion as seen in [38] and reproduced in figure 4.7, where Mo has been dosed onto a clean Au(111) using our setup. However, Mo has been reported to interact with the Au(111) surface if annealed even slightly resulting in a distorted herringbone [75, 76]. The exact nature of the interaction is suggested to be either a replacement where Mo atoms replace surface Au atoms which diffuse elsewhere [75] or a capping of the Mo particles by Au from the step edges diffusing onto the particles[76]. Either mechanism would account for the distorted herringbone seen in our MoS$_2$/Au(111) samples. Fortunately, the Au bound to the Mo in the particles is repelled by H$_2$S exposure, as the Mo preferentially binds to S causing the Au to retract from the particles [76]. The STM images of MoS$_2$ on Au(111) at different coverages shown later in this chapter illustrate that the herringbone distortion is very similar for samples with MoS$_2$ coverages above 0.1ML and no effect of the herringbone distortion is seen in the hydrogen evolution measurements presented in this work.

4.3   MoS$_2$ characterization

4.3.1   Spectroscopy

In order to investigate the chemical composition of the samples prepared by either the standard or the sintered preparation procedure, XPS was invoked. The XPS spectra are obtained on samples where the MoS$_2$ coverage is in the single layered regime (see section 4.4). Figure 4.8 shows survey spectra of a broad binding energy region for both a standard and a sintered sample. From these only Mo and S can be identified apart from the Au substrate peaks. The absence of C and O impurities was additionally confirmed by higher precision spectra of the binding energy regions of their 1s lines.

The chemical states of the Mo and S in the samples are examined by high precision spectra of the binding energy regions of the Mo 3d and S 2s lines around 230eV and the S 2p line around 165eV. These spectra are seen in figure 4.9 for the standard sample which had been annealed to 400 °C during preparation and in figure 4.10 for the sintered sample, annealed to 550 °C during preparation. The figures also show the de-convoluted peak
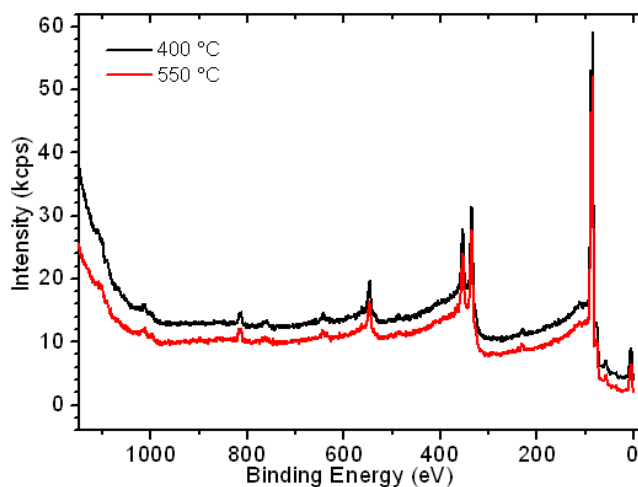
Figure 4.8: XPS survey spectrum of a broad binding energy window for a standard sample (black) and a sintered sample(red). The peaks in the spectrum are associated with Au, Mo and S.

shapes on a linear background. In both samples the Mo 3d$_{5/2}$ and Mo 3d$_{3/2}$ lines have binding energies of 228.5eV and 231.7eV consistent with Mo in the 4+ state as expected for MoS$_2$ [77, 78]. The sulphur 2s line lies as a shoulder on the Mo 3d$_{5/2}$ line and the S 2p line is therefore usually used in studies of MoS$_2$ [69, 79]. The S 2p$_{3/2}$ and S 2p$_{1/2}$ lines have binding energies of 162.0eV and 163.2eV for both samples, consistent with sulphur in MoS$_2$ [77, 80]. The ratio of S to Mo for the two samples is found from the peak intensities and sensitivity factors for the S 2p and Mo 3d lines. For the standard sample the XPS data yields a S to Mo ratio of 2.4 whereas the ratio for the sintered sample is 1.8, i.e. both samples have S to Mo ratios consistent with MoS$_2$. The XPS spectra thus conclusively shows that the Mo and S on the Au surface is in the form of from MoS$_2$.

4.3.2 Transferring samples

As the preparation of MoS$_2$ is harmful to the STM, the STM was not mounted on the chamber during these experiments. Therefore the samples were imaged by Sebastian Horch in a similar chamber also equipped with an Aarhus type STM. The samples were transferred in a vacuum transfer system in which the pressure is typically in the 10^{-7} Torr range. Thus

Figure 4.9: Standard sample XPS spectra of the Mo 3d and S 2s binding energy region on the left and the S 2p region on the right. The peaks are fitted on a linear background with Lorentzian peak shape (FWHM: Mo 3d$_{5/2}$: 1.8eV, Mo 3d$_{3/2}$: 1.8eV, S2s: 1.6eV, S 2p$_{3/2}$: 1.8eV, S 2p$_{1/2}$: 1.8eV.)
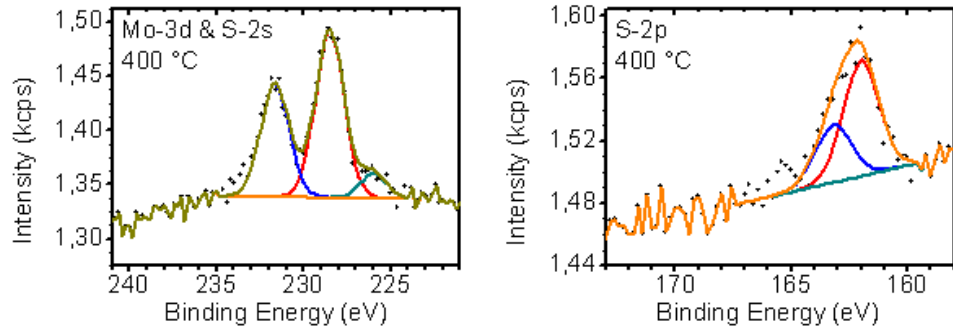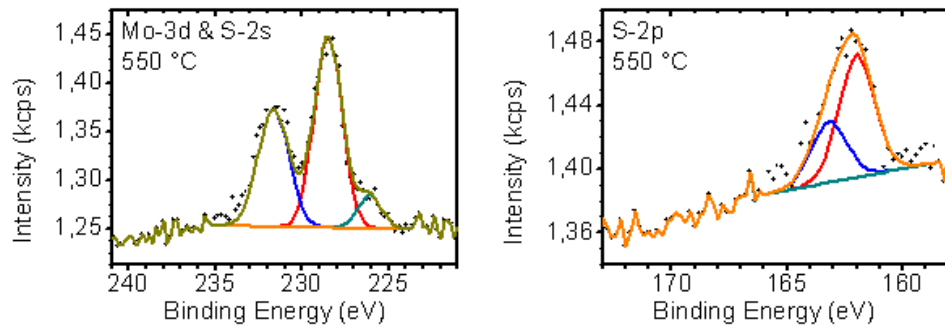

Figure 4.10: Sintered sample XPS spectra of the Mo 3d and S 2s binding energy region on the left and the S 2p region on the right. The peaks are fitted on a linear background with Lorentzian peak shape (FWHM: Mo 3d$_{5/2}$: 1.9eV, Mo 3d$_{3/2}$: 2.1eV, S2s: 1.6eV, S 2p$_{3/2}$: 1.8eV, S 2p$_{1/2}$: 1.8eV.)

the stability of the MoS$_2$ needs to be such that it withstands such pressures without changing its chemical state or morphology. If the activity for hydrogen evolution is also to be measured and to be compared to the imaged morphology, the chemical composition as well as the morphology of the MoS$_2$ needs to be stable even when subjected to ambient air. This was investigated by both STM and XPS. The MoS$_2$ morphology had previously been determined to be as expected with imaging without transfer of Au during the studies of MoS$_2$ on HOPG. Imaging after air exposure was tested by exposing a standard MoS$_2$ sample to air and transferring it back to our STM chamber and imaging it, before the STM was taken off the chamber. Figure 4.11 shows an image of this sample. Although the image is noisy, the MoS$_2$ morphology is clearly preserved and the edge state is still seen on the particles. Thus from the STM images the MoS$_2$ seems unaffected by the air exposure.
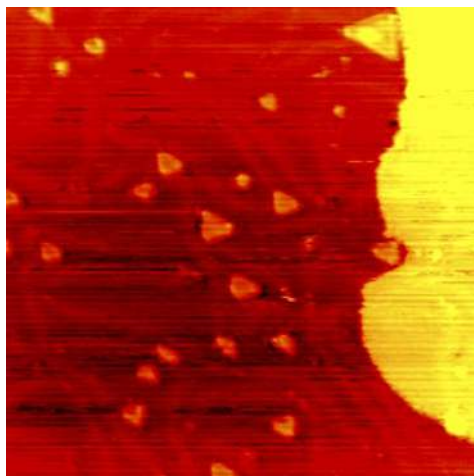
Figure 4.11: STM image of a MoS$_2$ on Au(111) (standard preparation) after exposure to air. The particle morphology seems unaffected by the air exposure. 470Å x 470Å, 0.89nA, 372mV.

XPS measurements of a sintered sample exposed to air reveal that by the air exposure some oxygen is adsorbed on the sample, but chemically the MoS$_2$ is unaffected by this. The oxygen observed in XPS may therefore be suspected to be adsorbed on the Au surface and the STM images suggest that it is diffusing on the surface, making the image slightly noisy, as the oxygen is not seen in any specific locations in the images. Figure 4.12 shows

XPS spectra in the regions revealing the chemical state of MoS$_2$, and no difference is seen in the chemical nature of either the Mo or the S from the air exposure. The sample was subsequently annealed to 200°C to see whether the oxygen reacts with the MoS$_2$ or simply desorbs from the surface. As seen in the figures, the MoS$_2$ was unaffected by this. The oxygen peak did decrease, so apparently, the oxygen is more likely to desorb than react with the MoS$_2$.

The experiments thus confirm that the MoS$_2$ is stable enough to transfer in vacuum before STM imaging and also stable enough to keep its chemical composition and its morphology at ambient conditions justifying the comparison between the STM imaged morphologies and measured hydrogen evolution activities of the samples.
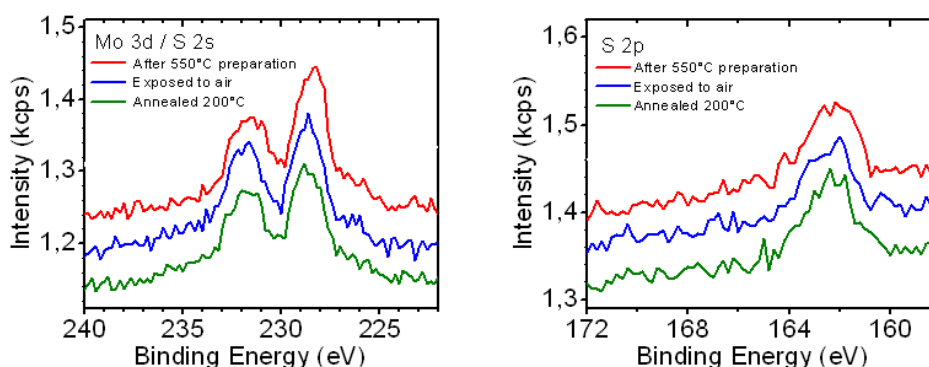
Figure 4.12: XPS spectra of the Mo 3d and S 2s binding energy region on the left and the S 2p region on the right. Red: As prepared sintered MoS$_2$ on Au(111) sample. Blue: The same sample after air exposure. Green: The same sample after annealing to 200°C.

4.3.3 Microscopy

The atomic structure of the MoS$_2$ nanoparticles imaged by STM can be seen in figure 4.13. The structure is the same for particles annealed to 400°C and 500°C. The particle shown in the figure was annealed to 500°C. The atomic distances in the basal plane of the particle is measured to be 3.13Å, which is in good agreement with observations on particles annealed to 400°C [38]. STM images of MoS$_2$ on Au have been interpreted by applying DFT simulations of STM images [39]. On the basal plane the sulphur atoms are imaged as protrusions, whereas the protrusions imaged on the edges do not coincide
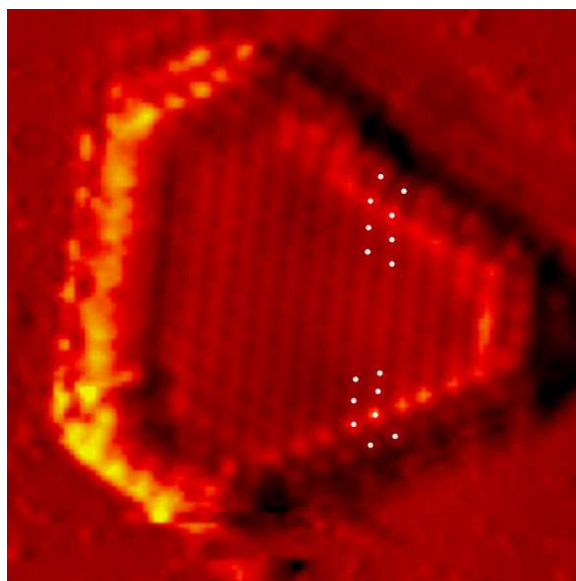
Figure 4.13: Atomically resolved STM image of a slightly truncated triangular MoS$_2$ nanoparticle from a sintered sample. As indicated with the white dots, the structure of the longer edges are consistent with the structure of a sulphided Mo edge. 60Å x 60Å, 1.0nA, 300mV

Figure 4.14: The apparent height of a MoS$_2$ nanoparticle from a sintered sample as a function of bias for a broad negative bias window based on images obtained at a tunneling current of 1.0nA. The geometrical distance of 3.16Å between S atoms in the top and bottom layer of the MoS$_2$ trilayer is indicated by a dashed line.

with the atomic positions. Under the sulfiding conditions of these experiments, the Mo edges are terminated by sulfur dimers. These are in registry with the sulfur atoms in the basal plane, but are imaged out of registry as the protrusions on the STM images are located between the sulphur dimers. Closer inspection of the registry of the edge protrusion of the particle in figure 4.13 reveals that the protrusions along the dominating edges of the particle are imaged out of registry and the protrusions along the truncating shorter edges are in registry. The predominating edges are thus sulphur terminated Mo edges and the short edges sulfur edges, which is consistent with the structure of MoS$_2$ nanoparticles from standard preparation first presented by the Besenbacher group [38].
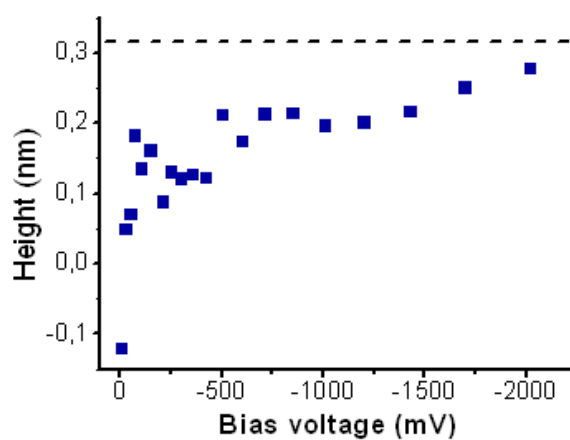
The apparent height of the MoS$_2$ nanoparticles is dependent on the tunneling voltage used. Figure 4.14 shows the apparent height as a function of the tunneling voltage. The trilayer MoS$_2$ sulphur to sulphur layer distance is 3.16Å and from the figure it is seen that as the voltage increases, the apparent height increases asymptotically towards this value. The values in the figure are measured on a particle post-annealed to 550°C, and are in complete agreement with similar data for the standard preparation presented from the Besenbacher group in the thesis of Jeppe Vang Lauritsen [73]. The heights shown in the figure are therefore interpreted as singlelayered MoS$_2$ nanoparticle heights.

4.4 MoS$_2$ morphology

4.4.1 Standard samples

As mentioned above, the MoS$_2$ morphology at low coverages and using the standard preparation is identical to the morphology previously reported in literature. The particles are triangular with a conducting edge state and are well-dispersed on the Au(111) surface. In this study we have investigated a wider range of coverages above the well known morphologies at up to 0.1ML used in the studies by the Besenbacher group. To study activity of the particles we have synthesized at different coverages, to identify the coverage regime where single layerered and well dispersed particles are found on the Au(111) surface. Figure 4.15 shows the MoS$_2$ morphology for area coverages from 0.06ML to 0.31ML, which shows that this regime spans beyond coverages of 0.1ML.

Figure 4.15 shows, that as the coverage is increased, the particle density and particle size increases. The particle shapes are very homogeneous at low coverages showing almost only triangles, but as the coverage increases
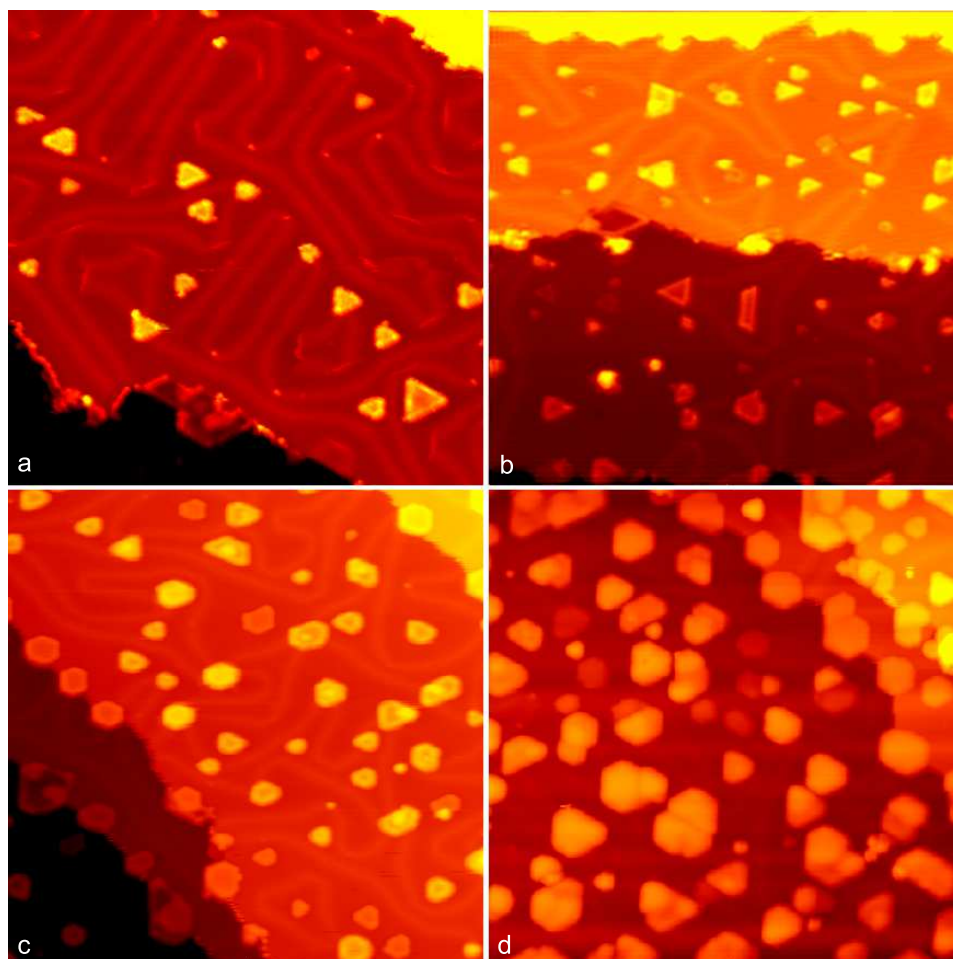
Figure 4.15: 470Å x 470Å STM images of standard samples at different coverages showing the MoS$_2$ morphologies. a: Area coverage 0.06ML (0.12nA, 4mV). b: Area coverage 0.11ML (-1.0nA, -967mV). c: Area coverage 0.16ML (-1.1nA, -999mV). d: Area coverage 0.31ML (-1.1nA, -2.0V).

more irregular particle shapes are seen and the triangular shape becomes increasingly truncated. Although the particle shapes become more diverse and truncated, the conducting edge state is preserved, also on the second MoS$_2$ layer.
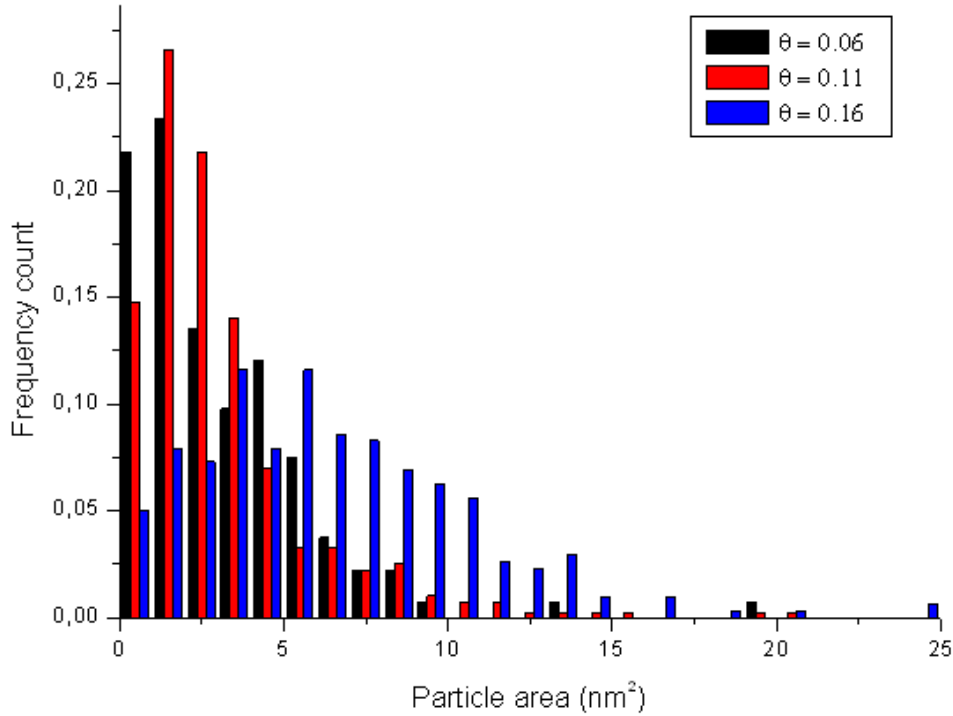
Figure 4.16: Sizedistributions of standard samples for three different MoS$_2$ coverage. The samples included are imaged in figure 4.15 a-c. Black: Area coverage 0.06ML. Red: Area coverage 0.11ML. Blue: Area coverage 0.16ML.

Figure 4.16 shows size distribution for three different coverages corresponding to the single layered regime of morphologies in figure 4.15 a-c. The distributions for the two lowest coverages, 0.06ML and 0.11ML, are narrow and centered around particle areas of 1-2nm^2. For the higher coverage sample (0.16ML), the sizedistribution is significantly broader and shifted upwards towards 5nm^2. Interestingly, the island density of the samples is 0.011/nm^2 for the lowest coverage sample and 0.024/nm^2 for the two other coverages. Thus, the initial increase in coverage is achieved by increasing the particle density to 0.024/nm^2, after which further increase is achieved

by an increase in particle size. In other words, the growth proceeds by first spreading out on the Au(111) surface and once a certain level is reached, the growth proceeds by a growth of the individual particles.

At some point, the particles become so big that they will coalesce. Image d in figure 4.15 reveals that before this process is completed, second layer growth sets in. In all images second layer islands are occasionally seen as well as particles which are lower than single layer particles and appear to have a height comparable to the level of the Au surface. However these are a few in the three samples in images a-c and the coverages of these samples can therefore be said to be in a single-layer regime. The shift from this single layer morphology to a multilayer growth occurs somewhere between coverages of 0.16ML and 0.31ML on the Au(111) surface.

4.4.2   Sintered samples
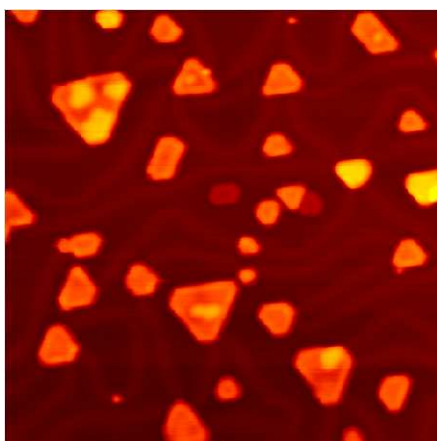
Figure 4.17: 470Å x 470Å STM images of a 0.17ML area coverage sintered sample showing the MoS$_2$ morphology. -0.8nA, -2.0V
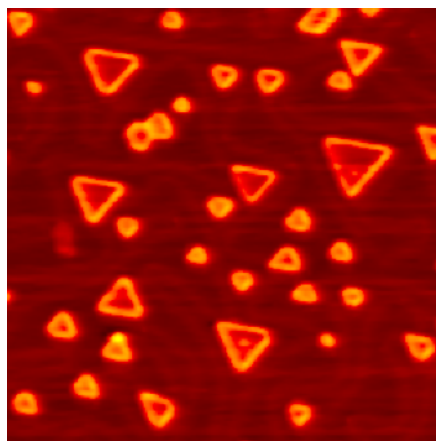
Figure 4.18: 470Å x 470Å STM images of a 0.23ML area coverage sintered sample showing the MoS$_2$ morphology. -1.2nA, -1.9V

Increasing the post-annealing temperature to 550°C yields a sintered version of the morphology obtained by post-annealing to 400°C. Figure 4.17 and 4.18 show two different coverages, 0.17ML and 0.23ML. For the sintered samples, the particle shapes are maintained as truncated single-layer MoS$_2$ nanoparticles with a conducting edge state. In both samples the particle

density is 0.013/nm^2. As the coverages of both samples are such that their densities would be expected to be 0.024/nm^2 if they were standard samples, it seems that the sintering causes the particle density to decrease. The sintering clearly also changes the particle sizes to what appears in the images to be a mixture of small particles and clearly larger ones. This would indicate an Ostwald-ripening type sintering, where larger islands are formed at the expense of the smaller particles.
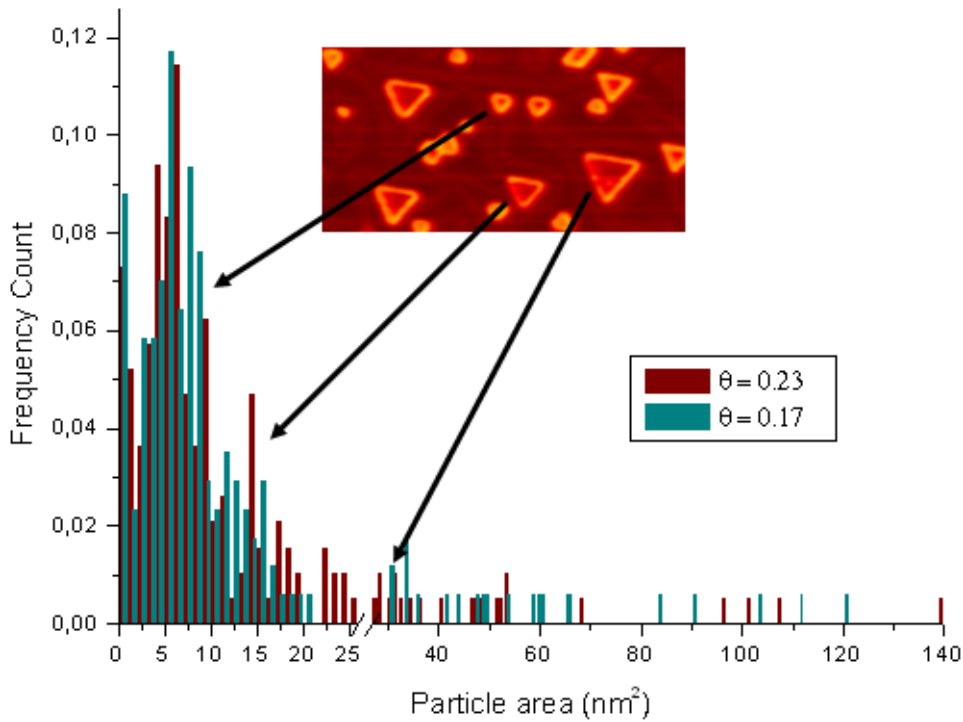
Figure 4.19: Sizedistributions of sintered samples for MoS$_2$ coverages of 0.17ML and 0.23ML. The STM image inset (470Å x 235Å) illustrates the particle sizes of the distribution.

The particle size distributions of the two samples are seen in figure 4.19. The smaller particles seen in the images have sizes centered around 5-6nm^2, i.e. are of similar sizes to the particles seen for the coverage of 0.16ML for the standard samples. The particle size distributions seem to have two peaks, one for the small particles and another for larger particles of sizes centered around 14-15nm^2. The STM image inset in the figure is the top half of

the image in figure 4.18, showing examples of the particle sizes of these two peaks in the size distributions. Contrary to the standard samples, the size distributions for the sintered samples have a very long tail, corresponding to the significant number of very large particles in these samples. The region imaged in figure 4.18 is a part of the larger region seen in figure 4.3, where several of these very large particles are seen.

4.5   Activity measurements
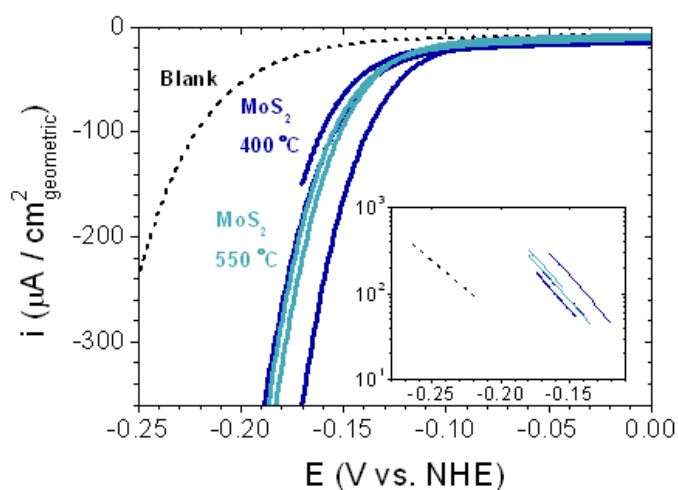
Figure 4.20: Polarization curves and Tafel plots(inset) in a cathodic potential window for 5 MoS$_2$ samples and the blank sample. Dark blue: Standard samples. Light blue: Sintered samples. Main: Polarization curve showing hydrogen evolution on all samples. All the MoS$_2$ samples have Tafel slopes of 55-60 mV/dec irrespective of annealing temperature and coverage. Sweep rate: 5 mV/s. Data is iR corrected.

To investigate the relation between the atomic structure and reactivity for hydrogen evolution of MoS$_2$ nanoparticles hydrogen evolution was measured on the imaged facet of the samples. The MoS$_2$ nanoparticles on Au(111) samples do indeed evolve hydrogen as seen in figure 4.20. The activity of the substrate, when accounting for the H$_2$S exposure and heating, is the activity of the blank sample. Only the hydrogen evolution of the added MoS$_2$ nanoparticles may add to the hydrogen evolution compared to this sample. The current evolved by the hydrogen evolution during anodic

voltage sweeps was measured on the blank sample and on the samples in which the MoS_2 morphology was single layered, i.e. 3 standard samples and two sintered samples. As seen in figure 4.20 the MoS_2 samples are all clearly more active than the blank sample and the differences in the MoS_2 samples are reflected in distinguishable hydrogen evolution curves.

The inset in figure 4.20 shows the Tafel plot of the data, including only the linear region of the data. All MoS_2 samples have very similar Tafel slopes of 55-60 mV/dec and the MoS_2 exchange current densities extracted from the plot may therefore be compared directly.

The exchange current densities extracted may now be related to the different types of sites on the surface. The morphologies of the samples are such that the MoS_2 nanoparticles are single layered, and therefore two general types of sites are seen: terrace sites and edge sites. From the STM images the amounts of each of these two types of sites can be quantified by measuring the area of the MoS_2 nanoparticles, which reflects the number of terrace sites and the length of the particle edge, which reflects the number of edge sites. Using values extracted from STM images to relate to activities measured on $0.10cm^2$ requires a verification that the images are representative of the surface. To be able to resolve the particles well enough to extract the edge length and area with reasonable resolution, images of 470Å x 470Å are used. This image size is not small enough that the atoms of the surface are resolved, but not too large; the edge length may easily be identified as the bright edge state is clearly seen as can be seen in the STM images in section 4.4. It is not realizable to image more than a small fraction of the surface; Imaging even 1 promille of the surface would require more than a million images. Therefore, we confirmed that the distribution of the MoS_2 on the surface was even by scanning electron microscopy (SEM) and scanning auger microscopy (SAM) measurements of a sample. This showed a very homogeneous distribution of the MoS_2 over the entire (111) facet of the Au crystal. This is also reflected by the relatively small deviations from STM image to STM image in the area coverage and edge lengths measured and in the very small differences in the size distributions from image to image.

As the areas and edge lengths measured from in the STM images are representative of the sample surface exposed to hydrogen evolution, their relation to the exchange current densities measured may be explored. Figure 4.21 and 4.22 shows the extracted exchange current densities as a function of the MoS_2 area coverage and the MoS_2 edge length determined from STM images of the samples. The area coverage, reflecting the number of MoS_2

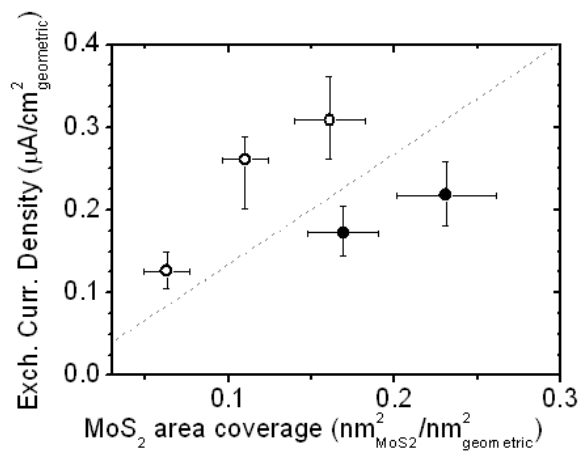Figure 4.21: The exchange current density of MoS$_2$ samples as a function of the MoS$_2$ area coverage. Open circles: Standard samples. Full circles: Sintered samples.
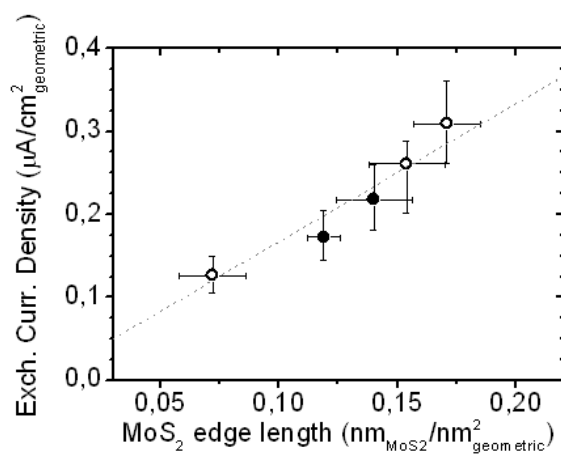
Figure 4.22: The exchange current density of MoS$_2$ samples as a function of the MoS$_2$ edge length. Open circles: Standard samples. Full circles: Sintered samples.

terrace sites, does not describe the exchange current density well. The data scattering is large and the samples annealed to 400°C yield higher activities per area than the samples annealed to 550°C. The edge length on the other hand describes the exchange current densities very well. A linear dependence is seen of the exchange current density on the edge length as expected if the activity of a catalytic surface is related to number of catalytically active sites on that surface. In this plot, both data from samples prepared with the standard preparation and sintered samples adhere to this linear dependence. The data does show a little scatter, but considering the inherent uncertainties in the experiments the scatter is very small. The errorbars on the data extracted from the STM images are simply standard deviations, reflecting the differences in the number from image to image, and does therefore not account for any uncertainties related to extracting from the small area imaged to the much larger area measured on in HER. The errorbars on the exchange current densities are standard deviations based on the Tafel plot data. Figure 4.21 and 4.22 show that the active site for the reaction is on the particle edge.
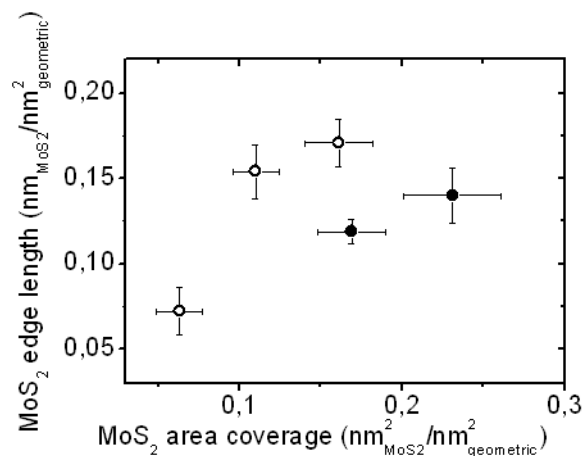
Figure 4.23: The MoS_2 edge length and area coverage. The plot shows great similarity to figure 4.21 as the exchange current density scales with the MoS_2 edge length. Open circles: standard samples. Full circles: Sintered samples.

Taking another look at figure 4.21, the positions of the data points here may also be explained. In the plot, the standard samples and the sintered samples are clearly different. With the active site on the edge of the particles, this can be understood by considering the ratios of edge to area in

different particle sizes. The larger a particle is, the less edge it has relative
to its area, and consequently the less its activity is per area. Though some
particles in the sintered samples have sizes that are similar to the sizes ob-
served in the standard samples, a large population of particles are larger
than the ones seen in the standard samples. On average the area to edge
ratio is therefore smaller in the sintered samples and thus the activity per
area is smaller. If the edge length is plotted as a function of the area cover-
age the plot should look very similar to the plot of exchange current density
as function of area coverage. Figure 4.23 shows such a plot, and indeed the
similarity to figure 4.21 is striking.
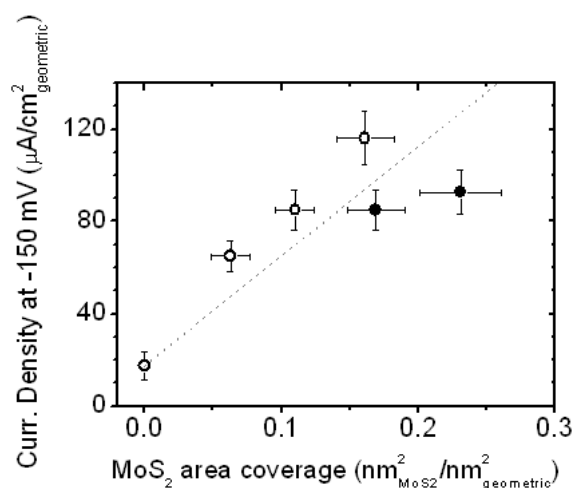
Figure 4.24: The current density at 150mV of MoS$_2$ samples as a function
of the MoS$_2$ area coverage. Open circles: Standard samples. Full circles:
Sintered samples.

In addition to using exchange current density as a measure of HER
activity, one can also use the current density at a specific overpotential from
the polarization curves. In general, this figure of merit is more pertinent
on practical devices, such as fuel cells or electrolyzers, whereas exchange
current density is a property of more fundamental interest. Figure 4.24
and 4.25 show the current density at 150mV overpotential as a function
of the area coverage and edge length analogous to figure 4.21 and 4.22 for
the exchange current density. The value of 150mV was chosen because
it is a value low enough that the effect of diffusion limitations should be

Figure 4.25: The current density at 150mV of MoS$_2$ samples as a function of the MoS$_2$ edge length. Open circles: Standard samples. Full circles: Sintered samples.

negligible for even the most active samples and high enough that all samples evolve enough hydrogen for the resulting current to be clearly higher than background current. The trends in these two figures are the same as for the exchange current density. The area coverage does not describe the current density; the data point for standard and sintered samples have two separate dependencies. The edge length describes the data well, the data for all samples collapse into one linear dependence of the current density on the edge length. The scatter in this plot seems a little larger than for the exchange current density, but the linear trend is still clear.

4.5.1 Differentiating between edge sites

Having identified the active site to the edge of the nanoparticles, one could hope to perhaps elaborate even further on its nature. The DFT calculations predict that the Mo edge sites are the active sites, and therefore attempts were made to show this. The Mo edge length was measured in the same way as the edge length, except only including the Mo edge. The Mo edge was estimated on each particle to be the predominating edge, i.e. the longer edges on truncated triangles. On hexagonal particles where the length difference between the two types of edges was not seen, the total edge length

was simply divided by two as the distinction between the two edges required atomic resolution which was not available in the 470Å x 470Å images. Figure 4.26 and 4.27 shows the exchange current density and current density at -150mV as a function of the Mo edge length. In the figures linear relations are again seen. The scatter of the data however is similar to the plots versus total edge length. It should be noted that a recent publication by the Besenbacher group suggests that the Mo edge dominance, which is very clear on the average sizes nanoparticles they observed, might not be maintained for the smallest particles [81]. Therefore an estimate was made of the impact of this possible change for the smallest particles on the total Mo edge measured and the effect is negligible. The conclusion is that the distinction between different segments of the edge lies beyond the resolution of these measurements.
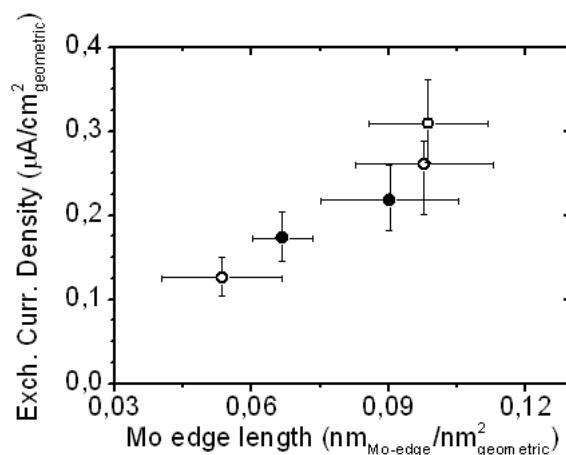
Figure 4.26: The exchange current density of MoS$_2$ samples as a function of the MoS$_2$ Mo-edge length. Open circles: Standard samples. Full circles: Sintered samples.
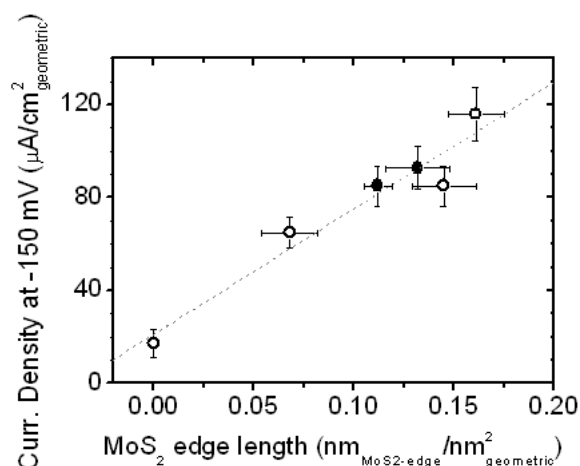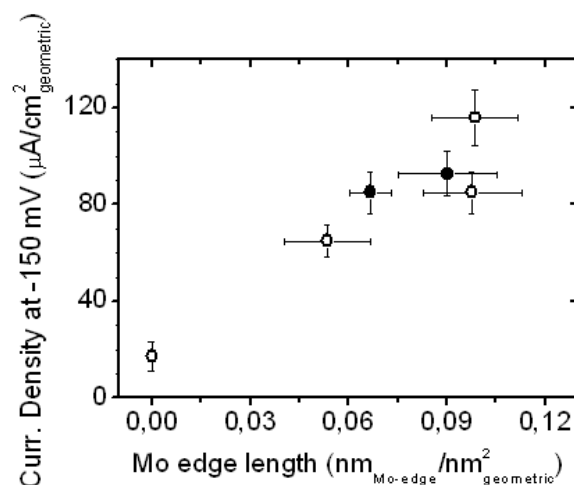
Figure 4.27: The current density at 150mV of MoS$_2$ samples as a function of the MoS$_2$ Mo-edge length. Open circles: Standard samples. Full circles: Sintered samples.

4.5.2   MoS$_2$ activity

Having located the active site for the hydrogen evolution reaction on MoS$_2$ nanoparticles, the turn over frequency (TOF) of the active site may be estimated. The relation between the exchange current density and the edge length is determined by a best linear fit to the data in figure 4.21, yielding a slope of $1.67 \cdot 10^{-20}$ A/nm$_{MoS2-edge}$. Remembering that the atomic spacing in MoS$_2$ is 3.15 and that the overall reaction $2H^+ + 2e^- \rightarrow H_2$ yields two electrons per turn over, the turn over frequency is 0.2 s^{-1}.

Comparing this number to the values for Pt and other metals first requires an estimate of their TOFs from their exchange current densities. For Pt(111) the site density is $1.5 \cdot 10^{15}$ sites/cm^2 as all surface atoms are believed to turn over for this reaction [82]. Using this density the exchange current density for Pt(111) of $4.5 \cdot 10^{-4}$ A/cm^2 [82], yields a TOF of 0.9 s^{-1}. Thus the MoS$_2$ TOF is slightly lower than the Pt value. Pt is the archetypical catalyst for the reaction, but in general the metal surfaces have a wide range of TOFs. Using the Pt(111) density, the exchange current density of $5.0 \cdot 10^{-13}$ A/cm^2 for Hg [19] yields a TOF of $1 \cdot 10^{-9}$ s^{-1}, showing that the turn over frequencies of the metals range over many orders of magnitude and that within this range, the MoS$_2$ TOF is in the high end.
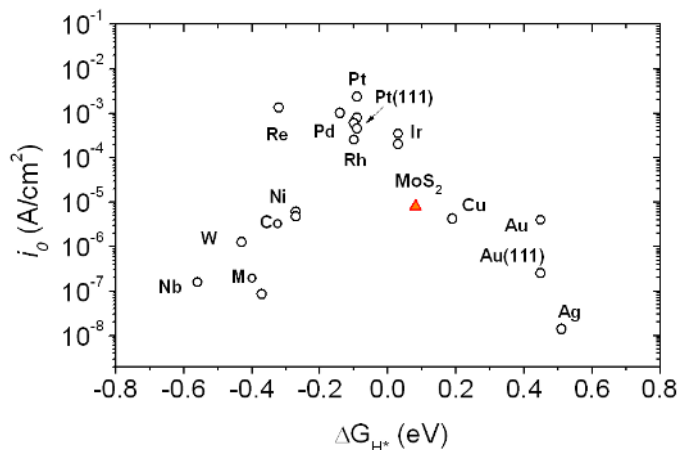
Figure 4.28: Volcano plot of the exchange current density as a function of the DFT-calculated Gibbs free energy of adsorbed hydrogen for MoS$_2$ nanoparticles and the pure metals. Samples are polycrystalline unless otherwise noted. The Gibbs free energies for the metals are from [17]. Exchange current densities are from [19, 21–24]

To more easily compare the activity of MoS$_2$ to other materials and to be able to place it on the volcano based on its DFT calculated Gibbs free energy, the TOF is converted into an exchange current density. To compare on a site to site basis, the exchange current density is calculated for an imaginary MoS$_2$ edge site density equal to the Pt(111) site density. This of course is not a realizable density, but merely a gedanken experiment to allow fair comparison of the sites, no different than using the Pt density to calculate a TOF for Hg. The MoS$_2$ exchange current density calculated in this way is $7.9 \cdot 10^{-6}$ A/cm^2. In figure 4.28 this value is added to the volcano plot from figure 1.1 using the DFT calculated Gibbs free energy of 0.08eV. The figure reveals that MoS$_2$ lies just below the well-known highly catalytically active but scarce and noble metals close to Pt, and above the common metals. The figure also shows that MoS$_2$ follows the volcano trend, validating the predictive capacity of this DFT model and its applicabiliy beyond metal catalysts.

Chapter 5

Summary and Outlook

In this work STM investigations of MoS_2 nanoparticles on etch pitted HOPG and Au(111) surfaces were undertaken to relate the structure and activity for hydrogen evolution on MoS_2 nanoparticles.

On the etch pitted HOPG surface, MoS_2 nanoparticles were synthesized and imaged as 3-4nm wide, 1-1.5nm high particles. The particles are very weakly bound to the HOPG substrate, resulting in poor imaging conditions and unresolved particle shapes with the careful scanning parameters required. A strategy of combining increased annealing temperatures during preparation and the introduction of sputter defects to achieve flatter, larger particles with better pinning to the substrate to achieve resolution of the particle shapes was chosen and experiments initiated. Unfortunately the experiments were hindered by an H_2S induced corrosion of the STM and in the meanwhile the Besenbacher group had taken up STM studies of the same system and achieved resolution of the particle shape by invoking the same strategy. These results showed that the structure of MoS_2 on HOPG was analogous to the structure on Au(111).

On the Au(111) surface MoS_2 nanoparticles were synthesized using two different preparation procedures using annealing temperatures of 400°C for standard samples and 550°C for sintered samples. The particles resulting from both preparation procedures were shown by XPS and atomically resolved STM to be MoS_2. The morphologies of the particles in standard samples were shown to be primarily single layered triangular particles at a low coverage of 0.06ML and as the coverage increases to 0.16ML the single layered particles increase their density on the surface and start to grow in more truncated shapes and finally, at an area coverage of 0.31ML the particles were observed to have multilayered forms. The single-layered region

of coverages for the samples was shown to be maintained for coverages up to somewhere between 0.16ML and 0.31ML. The sintered samples with area coverages of 0.17ML and 0.23ML showed morphologies with many larger, single layer an truncated triangular particles.

The MoS_2 on Au(111) samples from both preparation methods were tested for their hydrogen evolution activity after STM imaging. The activity for hydrogen evolution of the samples was shown to scale with the edge length of the MoS_2 nanoparticles and not with the area coverage, showing that the active site for hydrogen evolution is on the edge of the MoS_2 nanoparticles. The activity in terms of the exchange current density of the MoS_2 nanoparticle edge was compared to other catalysts for hydrogen evolution and found to be in the higher activity range, above the common metals, and its activity is consistent with the predicted volcano trend for Gibbs free energies of hydrogen adsorption on hydrogen evolution catalysts.

The work presented in this thesis has identified the active site for hydrogen evolution on MoS_2 nanoparticles to the particle edge by combining STM imaging of UHV model system samples with reactivity measurements in ambient conditions of the same samples. The MoS_2 edge sites are more active than the common metals, yet show less activity than the precious Pt-group metals. One could imagine that the activity of the MoS_2 nanoparticle edge sites could be improved by appropriately tuning the electronic properties of the edge to increase the bonding of the adsorbed hydrogen and thus move the material further towards the peak of the volcano. This could possibly be achieved by promoting with Ni or Co as known from the HDS reaction or by other elements not yet identified.

Another path one might explore is the investigation of other transistionmetal sulphides, nitrides or oxides and compounds not yet thought of that might result from a DFT to screening based on the Gibbs free energy of adsorption. The field of interesting research to be done is wide open. Nanoparticulate MoS_2 may or may not be a next generation hydrogen evolution catalyst depending on its industrial properties such as stability, ability to disperse on highly porous supports and so on, but it has certainly opened up for new insights on the approach to finding better hydrogen evolution catalysts.

Bibliography

[1] Gabor A. Somorjai. *Introduction to Surface Chemistry and Catalysis*. John Wiley and Sons, New York, 1994.

[2] Ib Chorkendorff and Hans Niemantsverdriet. *Concepts of Modern Catalysis and Kinetics*. Wiley-VCH, Weinheim, 2003.

[3] P.L.J. Gunter, J.W. Niemantsverdriet, F.H. Ribeiro, and G.A. Somorjai. Surface science approach to modeling supported catalysts. *Catalysis Reviews-Science and Engineering*, 39(1-2):77–168, 1997.

[4] S. Dahl, E. Törnqvist, and I. Chorkendorff. *J. Catal.*, 192:381–390, 2000.

[5] S. Dahl, A. Logadottir, C.H.J. Jacobsen, and J.K. Nørskov. *Appl. Catal. A: General*, 222:19–29, 2001.

[6] S. Dahl, A. Logadottir, R.C. Egeberg, J.H. Larsen, I. Chorkendorff, E. Tornqvist, and J.K. Norskov. Role of steps in n-2 activation on ru(0001). *Physical Review Letters*, 83(9):1814–1817, 1999.

[7] J.K. Norskov, T. Bligaard, A. Logadottir, S. Bahn, L.B. Hansen, M. Bollinger, H. Bengaard, B. Hammer, Z. Sljivancanin, M. Mavrikakis, Y. Xu, S. Dahl, and C.J.H. Jacobsen. Universality in heterogeneous catalysis. *Journal of Catalysis*, 209(2):275–278, 2002.

[8] R.C. Egeberg, S. Dahl, A. Logadottir, J.H. Larsen, J.K. Norskov, and I. Chorkendorff. N-2 dissociation on fe(110) and fe/ru(0001): what is the role of steps? *Surface Science*, 491(1-2):183–194, 2001.

[9] A.K. Santra and D.W. Goodman. Oxide-supported metal clusters: models for heterogeneous catalysts. *Journal of Physics-Condensed Matter*, 15(2):R31–R62, 2003.

[10] M.S. Dresselhaus and I.L. Thomas. Alternative energy technologies. *Nature*, 414(6861):332–337, 2001.

[11] M.Z. Jacobson, W.G. Colella, and D.M. Golden. Cleaning the air and improving health with hydrogen fuel-cell vehicles. *Science*, 308(5730):1901–1905, 2005.

[12] J.K. Norskov and C.H. Christensen. Chemistry: Enhanced: Toward efficient hydrogen production at surfaces. *Science*, 312(5778):1322–1323, 2006.

[13] M. Gratzel. Photoelectrochemical cells. *Nature*, 414(6861):338–344, 2001.

[14] L. Schapbach and A. Zuttel. Hydrogen-storage materials for mobile applications. *Nature*, 414(6861):353, 2001.

[15] John O'M. Bockris and Shahed U. M. Khan. *Surface Electrochemistry - A Molecular Level Approach*. Plenum Press, New York, 1993.

[16] The Southampton Electrochemistry Group. *Instrumental Methods in Electrochemistry*. 1985.

[17] J.K. Norskov, T. Bligaard, A. Logadottir, J.R. Kitchin, J.G. Chen, S. Pandelov, and J.K. Norskov. Trends in the exchange current for hydrogen evolution. *Journal of the Electrochemical Society*, 152(3):J23–J26, 2005.

[18] R. Parsons. The rate of electrolytic hydrogen evolution and the heat of adsorption of hydrogen. *Transactions of the Faraday Society*, 54(7):1053–1063, 1958.

[19] S. Trasatti. Work function, electronegativity, and electrochemical behavior of metals .3. electrolytic hydrogen evolution in acid solutions. *Journal of Electroanalytical Chemistry*, 39(1):163, 1972.

[20] B.E. Conway and B.V. Tilak. Interfacial processes involving electrocatalytic evolution and oxidation of h-2, and the role of chemisorbed h. *Electrochimica Acta*, 47(22-23):3571–3594, 2002.

[21] J. O'M. Bockris and A. K. N. Reddy. *Modern electrochemisty*, volume 2. Plenum Press, New York, 1970.

[22] J. Perez, E.R. Gonzalez, and H.M. Villullas. Hydrogen evolution reaction on gold single-crystal electrodes in acid solutions. *Journal of Physical Chemistry B*, 102(52):10931–10935, 1998.

[23] O. Savadogo and D.L. Piron. New hydrogen cathodes in acid-medium - case of nickel electrodeposited with heteropolyacids (hpas). *International Journal of Hydrogen Energy*, 15(10):715–721, 1990.

[24] N. M. Markovic and P. N. Ross. *in Modern electrochemisty*. A. Wieckovski, Editor Macel Dekker, New York, 1999.

[25] Henrik Topsøe, Bjerne S. Clausen, and Franklin E. Massoth. *Hydrotreating Catalysis - Science and Technology, vol. 11*. Eds. J. R. Anderson, M. Boudart, Springer Verlag, New York, 1996.

[26] R.R. Chianelli, M.H. Siadati, M.P. De la Rosa, G. Berhault, J.P. Wilcoxon, R. Bearden, and B.L. Abrams. Catalytic properties of single layers of transition metal sulfide catalytic materials. *Catalysis Reviews-Science and Engineering*, 48(1):1–41, 2006.

[27] R. Prins, V.H.J. Debeer, and G.A. Somorjai. Structure and function of the catalyst and the promoter in co-mo hydrodesulfurization catalysts. *Catalysis Reviews-Science and Engineering*, 31(1-2):1–41, 1989.

[28] J.A. Wilson and A.D. Yoffe. Transition metal dichalcogenides discussion and interpretation of observed optical, electrical and structural properties. *Advances in Physics*, 18(73):193, 1969.

[29] B. Schonfeld, J.J. Huang, and S.C. Moss. Anisotropic mean-square displacements (msd) in single-crystals of 2h-mos2 and 3r-mos2. *Acta Crystallographica Section B-Structural Science*, 39(AUG):404–407, 1983.

[30] R.R. Chianelli, E.B. Prestridge, T.A. Pecoraro, and J.P. Deneufville. Molybdenum-disulfide in the poorly crystalline rag structure. *Science*, 203(4385):1105–1107, 1979.

[31] R. Dickinson and L. Pauling. The crystal structure of molybdenite. *J. Am. Chem. Soc.*, 45:1466, 1923.

[32] M. Daage and R.R. Chianelli. Structure-function relations in molybdenum sulfide catalysts - the rim-edge model. *Journal of Catalysis*, 149(2):414–427, 1994.

[33] M. Salmeron, G.A. Somorjai, A. Wold, R. Chianelli, and K.S. Liang. The adsorption and binding of thiophene, butene and h2s on the basal-plane of mos2 single-crystals. *Chemical Physics Letters*, 90(2):105–107, 1982.

[34] T.F. Hayden and J.A. Dumesic. Studies of the structure of molybde-num oxide and sulfide supported on thin-films of alumina. *Journal of Catalysis*, 103(2):366–384, 1987.

[35] S. Kasztelan, H. Toulhoat, J. Grimblot, and J.P. Bonnelle. A geo-metrical model of the active phase of hydrotreating catalysts. *Applied Catalysis*, 13(1):127–159, 1984.

[36] H. Shimada. Morphology and orientation of mos2 clusters on al2o3 and tio2 supports and their effect on catalytic performance. *Catalysis Today*, 86(1-4):17–29, 2003.

[37] A. Carlsson, M. Brorson, and H. Topsoe. Morphology of ws2 nan-oclusters in ws2/c hydrodesulfurization catalysts revealed by high-angle annular dark-field scanning transmission electron microscopy (haadf-stem) imaging. *Journal of Catalysis*, 227(2):530–536, 2004.

[38] S. Helveg, J.V. Lauritsen, E. Laegsgaard, I. Stensgaard, J.K. Norskov, B.S. Clausen, H. Topsoe, and F. Besenbacher. Atomic-scale structure of single-layer mos2 nanoclusters. *Physical Review Letters*, 84(5):951–954, 2000.

[39] M.V. Bollinger, J.V. Lauritsen, K.W. Jacobsen, J.K. Norskov, S. Helveg, and F. Besenbacher. One-dimensional metallic edge states in mos2. *Physical Review Letters*, 8719(19), 2001.

[40] J.V. Lauritsen, M.V. Bollinger, E. Laegsgaard, K.W. Jacobsen, J.K. Norskov, B.S. Clausen, H. Topsoe, and F. Besenbacher. Atomic-scale insight into structure and morphology changes of mos2 nanoclusters in hydrotreating catalysts. *Journal of Catalysis*, 221(2):510–522, 2004.

[41] J.V. Lauritsen, M. Nyberg, R.T. Vang, M.V. Bollinger, B.S. Clausen, H. Topsoe, K.W. Jacobsen, E. Laegsgaard, J.K. Norskov, and F. Be-senbacher. Chemistry of one-dimensional metallic edge states in mos2 nanoclusters. *Nanotechnology*, 14(3):385–389, 2003.

[42] H. Topsoe, B. Hinnemann, J.K. Norskov, J.V. Lauritsen, F. Besen-bacher, P.L. Hansen, G. Hytoft, R.G. Egeberg, and K.G. Knudsen. The

role of reaction pathways and support interactions in the development of high activity hydrotreating catalysts. *Catalysis Today*, 107-08:12–22, 2005.

[43] P. Raybaud, J. Hafner, G. Kresse, S. Kasztelan, and H. Toulhoat. Ab initio study of the h-2-h2s/mos2 gas-solid interface: The nature of the catalytically active sites. *Journal of Catalysis*, 189(1):129–146, 2000.

[44] J. M. Thomas and W. J. Thomas. *Principles and Practice of Heterogeneous Catalysis.* VCH Verlagsgesellshaft, Weinheim, 1997.

[45] C.D. Wagner et al. *Handbook of X-Ray Photoelectron Spectroscopy - A Reference Book of Standard Data For Use in X-Ray Photoelectron Spectroscopy.* Perkin-Elmer Corporation - Physical Electronics Division, USA, 1979.

[46] *NIST X-ray Photoelectron Spectroscopy Database: http://srdata.nist.gov/xps.*

[47] Ib Chorkendorff and Jane H. Larsen. *An Experimentalists Approach to Materials Surface Science.* To be published.

[48] Roland Weisendanger. *Scanning Probe Microscopy and Spectroscopy - Methods and Applications.* Cambridge University Press, 1994.

[49] J. Tersoff and D.R. Hamann. Theory and application for the scanning tunneling microscope. *Physical Review Letters*, 50(25):1998–2001, 1983.

[50] J. Tersoff and D.R. Hamann. Theory of the scanning tunneling microscope. *Physical Review B*, 31(2):805–813, 1985.

[51] J. Bardeen. Tunnelling from a many-particle point of view. *Physical Review Letters*, 6(2):57, 1961.

[52] N.D. Lang. Vacuum tunneling current from an adsorbed atom. *Physical Review Letters*, 55(2):230–233, 1985.

[53] N.D. Lang. Theory of single-atom imaging in the scanning tunneling microscope. *Physical Review Letters*, 56(11):1164–1167, 1986.

[54] *Introduction to the Aarhus STM.* Part of the documentation of the STM from the Aarhus STM group.

[55] M. Breysse, B.A. Bennett, D. Chadwick, and M. Vrinat. Structure and hds activity of co-mo catalysts - a comparison of alumina and carbon supports. *Bulletin des Societes Chimiques Belges*, 90(12):1271–1277, 1981.

[56] J.C. Duchet, E.M. Vanoers, V.H.J. Debeer, and R. Prins. Carbon-supported sulfide catalysts. *Journal of Catalysis*, 80(2):386–402, 1983.

[57] H. Topsoe and B.S. Clausen. Importance of co-mo-s type structures in hydrodesulfurization. *Catalysis Reviews-Science and Engineering*, 26(3-4):395–420, 1984.

[58] J.P.R. Vissers, B. Scheffer, V.H.J. Debeer, J.A. Moulijn, and R. Prins. Effect of the support on the structure of mo-based hydrodesulfurization catalysts - activated carbon versus alumina. *Journal of Catalysis*, 105(2):277–284, 1987.

[59] D. Tomanek, S.G. Louie, H.J. Mamin, D.W. Abraham, R.E. Thomson, E. Ganz, and J. Clarke. Theory and observation of highly asymmetric atomic-structure in scanning-tunneling-microscopy images of graphite. *Physical Review B*, 35(14):7790–7793, 1987.

[60] I.P. Batra, N. Garcia, H. Rohrer, H. Salemink, E. Stoll, and S. Ciraci. A study of graphite surface with stm and electronic-structure calculations. *Surface Science*, 181(1-2):126–138, 1987.

[61] S. Hembacher, F.J. Giessibl, J. Mannhart, and C.F. Quate. Revealing the hidden atom in graphite by low-temperature atomic force microscopy. *Proceedings of the National Academy of Sciences of the United States of America*, 100(22):12539–12542, 2003.

[62] H. Hovel, T. Becker, A. Bettac, B. Reihl, M. Tschudy, and E.J. Williams. Controlled cluster condensation into preformed nanometer-sized pits. *Journal of Applied Physics*, 81(1):154–158, 1997.

[63] J.D. McBride, B. Van Tassell, R.C. Jachmann, and T.P. Beebe. Molecule corrals as templates for the formation of metal and silicon nanostructures. *Journal of Physical Chemistry B*, 105(18):3972–3980, 2001.

[64] Z. Song, T.H. Cai, J.C. Hanson, J.A. Rodriguez, and J. Hrbek. Structure and reactivity of ru nanoparticles supported on modified graphite surfaces: A study of the model catalysts for ammonia synthesis. *Journal of the American Chemical Society*, 126(27):8576–8584, 2004.

[65] R.T. Yang and C. Wong. Mechanism of single-layer graphite oxidation - evaluation by electron-microscopy. *Science*, 214(4519):437–438, 1981.

[66] F. Stevens, L.A. Kolodny, and T.P. Beebe. Kinetics of graphite oxidation: Monolayer and multilayer etch pits in hopg studied by stm. *Journal of Physical Chemistry B*, 102(52):10799–10804, 1998.

[67] Stig Helveg. *Scanning Tunneling Microscopy Studies on Model Systems Relevant for Heterogeneous Catalysis.* PhD thesis, University of Aarhus, Denmark, 2000.

[68] E.J.M. Hensen, P.J. Kooyman, Y. van der Meer, A.M. van der Kraan, V.H.J. de Beer, J.A.R. van Veen, and R.A. van Santen. The relation between morphology and hydrotreating activity for supported mos2 particles. *Journal of Catalysis*, 199(2):224–235, 2001.

[69] Q. Li, E.C. Walter, W.E. van der Veer, B.J. Murray, J.T. Newberg, E.W. Bohannan, J.A. Switzer, J.C. Hemminger, and R.M. Penner. Molybdenum disulfide nanowires and nanoribbons by electrochemical/chemical synthesis. *Journal of Physical Chemistry B*, 109(8):3169–3182, 2005.

[70] Q. Li, J.T. Newberg, E.C. Walter, J.C. Hemminger, and R.M. Penner. Polycrystalline molybdenum disulfide (2h-mos2) nano- and microribbons by electrochemical/chemical synthesis. *Nano Letters*, 4(2):277–281, 2004.

[71] I. Lopez-Salido, D.C. Lim, and Y.D. Kim. Ag nanoparticles on highly ordered pyrolytic graphite (hopg) surfaces studied using stm and xps. *Surface Science*, 588(1-3):6–18, 2005.

[72] J. Kibsgaard, J.V. Lauritsen, E. Laegsgaard, B.S. Clausen, H. Topsoe, and F. Besenbacher. Cluster-support interactions and morphology of mos2 nanoclusters in a graphite-supported hydrotreating model catalyst. *Journal of the American Chemical Society*, 2006.

[73] Jeppe Vang Lauritsen. *Atomic-scale Study of a Hydrodesulfurization Model Catalyst.* PhD thesis, University of Aarhus, Denmark, 2002.

[74] A.J. Leavitt and T.P. Beebe. Chemical-reactivity studies of hydrogen-sulfide on au(111). *Surface Science*, 314(1):23–33, 1994.

[75] M.M. Biener, J. Biener, R. Schalek, and C.M. Friend. Surface alloying of immiscible metals: Mo on au(111) studied by stm. *Surface Science*, 594(1-3):221–230, 2005.

[76] D.V. Potapenko, J.M. Horn, R.J. Beuhler, Z. Song, and M.G. White. Reactivity studies with gold-supported molybdenum nanoparticles. *Surface Science*, 574(2-3):244–258, 2005.

[77] J.C. Muijsers, T. Weber, R.M. vanHardeveld, H.W. Zandbergen, and J.W. Niemantsverdriet. Sulfidation study of molybdenum oxide using moo3/sio2/si(100) model catalysts and mo-3(iv)-sulfur cluster compounds. *Journal of Catalysis*, 157(2):698–705, 1995.

[78] W. Grunert, A.Y. Stakheev, R. Feldhaus, K. Anders, E.S. Shpiro, and K.M. Minachev. Analysis of mo(3d) xps spectra of supported mo catalysts - an alternative approach. *Journal of Physical Chemistry*, 95(3):1323–1328, 1991.

[79] S. Mattila, J.A. Leiro, M. Heinonen, and T. Laiho. Core level spectroscopy of mos2. *Surface Science*, 600(24):5168–5175, 2006.

[80] Y. Araki, K. Honna, and H. Shimada. Formation and catalytic properties of edge-bonded molybdenum sulfide catalysts on tio2. *Journal of Catalysis*, 207(2):361–370, 2002.

[81] J.V. Lauritsen, J. Kibsgaard, S. Helveg, H. Topsoe, B.S. Clausen, E. Laegsgaard, and F. Besenbacher. Size-dependent structure of mos2 nanocrystals. *Nature Nanotechnology*, 2:53–58, 2007.

[82] N.M. Markovic, B.N. Grgur, and P.N. Ross. Temperature-dependent hydrogen electrochemistry on platinum low-index single-crystal surfaces in acid solutions. *Journal of Physical Chemistry B*, 101(27):5405–5413, 1997.

List of Papers

Paper I *Biomimetic Hydrogen evolution: MoS$_2$ Nanoparticies as Catalyst for Hydrogen Evolution*
B. Hinnemann, P.G. Moses, J. Bonde, K.P. Jørgensen, J.H. Nielsen, S. Horch, I. Chorkendorff and J.K. Nørskov
Journal of the American Chemical Society **127** 5308-5309 (2005)

Paper II *Identifying the active site: Atomic-scale imaging and ambient reactivity of MoS2 nanocatalysts*
T. F. Jaramillo, K. P. Jørgensen, J. Bonde, J. H. Nielsen, S. Horch and I. Chorkendorff
Submitted

Paper 1

Biomimetic Hydrogen Evolution: MoS$_2$ Nanoparticles as Catalyst for Hydrogen Evolution

Berit Hinnemann, Poul Georg Moses, Jacob Bonde, Kristina P. Jørgensen, Jane H. Nielsen,
Sebastian Horch, Ib Chorkendorff, and Jens K. Nørskov*

*Center for Atomic-scale Materials Physics, Department of Physics, NanoDTU, Technical University of Denmark,
DK-2800 Lyngby, Denmark*

Received January 24, 2005; E-mail: norskov@fysik.dtu.dk

The electrochemical hydrogen evolution process whereby protons and electrons are combined into molecular hydrogen is catalyzed most effectively by the Pt group metals.[1] The interest in hydrogen evolution catalysts is currently increasing, as molecular hydrogen, H$_2$, is being considered as an energy carrier.[2] Unlike the hydrocarbon fuels used today, hydrogen produces only water during oxidation, for instance in a fuel cell. For hydrogen to be a real alternative to hydrocarbons, it must be produced in a sustainable fashion. One possibility is to use sunlight directly or indirectly (through wind power, for instance) to split water.[2] This requires an efficient catalyst for hydrogen evolution, preferably based on materials that are cheap and abundant. It is therefore important to find alternatives to the Pt group metals.

Hydrogenases and nitrogenases are also effective catalysts for the hydrogen evolution process[3,4] even though the catalytically active site of these enzymes contains the much less noble metals Fe, Ni, and Mo. Recently it has become possible to anchor hydrogenase to an electrode surface,[5] and considerable progress has been made in the synthesis of compounds in solution resembling the hydrogenase active site and showing activity for hydrogen evolution.[6]

In the present communication, we use density functional calculations to guide us to a new inorganic analogue of the other hydrogen-producing enzyme, nitrogenase. We analyze the difference between the metallic and the biological catalysts and show that in terms of being able to stabilize intermediates involving atomic hydrogen they have very similar properties. This allows us to identify a parameter determining whether a certain compound will be suitable as a catalyst in electrochemical hydrogen evolution, and it provides an efficient way to search for new systems.

Most water-splitting processes rely on electrochemical hydrogen evolution $2H^+ + 2e^- \rightarrow H_2$ in the final step. The hydrogen evolution reaction must in the first step involve bonding of hydrogen to the catalyst $H^+ + e^- + * \rightarrow H*$, where * denotes a site on the surface able to bind to hydrogen. The second step is the release of molecular hydrogen through one of the two processes:[1] $2H* \rightarrow H_2 + 2*$ or $H^+ + e^- + H* \rightarrow H_2 + *$.

Using density functional theory (DFT) calculations, we can elucidate the thermochemistry (which is independent on the precise mechanism of the second step) of the reaction; see Figure 1.[7] By calculating the free energy of atomic hydrogen bonding to the catalyst, one can compare different metal surfaces as catalysts. For a chemical process to proceed at or around room temperature, no reaction step can be associated with large changes in the free energy. This immediately excludes the metals that form strong bonds to atomic hydrogen (Ni and Mo in Figure 1) as good catalysts because the hydrogen release step will be slow. Metals that do not bind to atomic hydrogen (Au in Figure 1) are also excluded because here the proton/electron-transfer step will be thermodynamically uphill
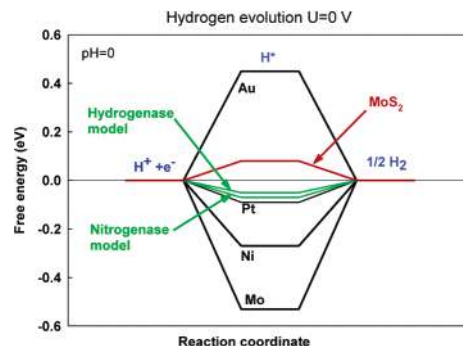

Figure 1. Calculated free energy diagram for hydrogen evolution at a potential $U = 0$ relative to the standard hydrogen electrode at pH = 0. The free energy of $H^+ + e^-$ is by definition the same as that of $^1/_2$ H$_2$ at standard conditions. The free energy of H atoms bound to different catalysts is then found by calculating the free energy with respect to molecular hydrogen including zero-point energies and entropy terms. The comparison of different elemental metals is taken from ref 7. The results for hydrogenase are from ref 11. The included result for MoS$_2$ is the free energy required to increase the hydrogen coverage from 25 to 50%; see Figure 2.
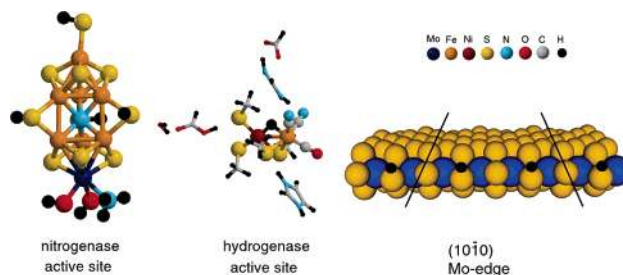
Figure 2. (Left) Nitrogenase FeMo cofactor (FeMoco) with three hydrogen atoms bound at the equatorial μ_2S sulfur atoms. (Middle) Hydrogenase active site with one hydrogen atom bound. The structure is taken from ref 11. (Right) MoS$_2$ slab with sulfur monomers present at the Mo edge. The coverage is 50%, i.e., hydrogen is bound at every second sulfur atom. The lines mark the dimension of the unit cell in the *x*-direction.

and therefore slow. There could be extra energy barriers associated with the proton-transfer steps or H$_2$ recombination, but independent of this it is a necessary, but not sufficient, criterion for a material to be a good catalyst that the free energy of adsorbed H is close to that of the reactant or product (i.e., $\Delta G_H^\circ \cong 0$). This principle can explain available experimental observations regarding metals as catalysts and electrode materials for hydrogen evolution.[7]

It is interesting to apply the same analysis to the active sites in nitrogenases and hydrogenases. For nitrogenase we have considered the model of the active site, the FeMo cofactor (FeMoco) shown in Figure 2.[8] We find that hydrogen atoms can only bind exothermically to the three equatorial sulfur ligands (μ_2S ligands) on the FeMoco. When the free energy of hydrogen atoms bound to the equatorial sulfur of the FeMoco is included in Figure 1, it
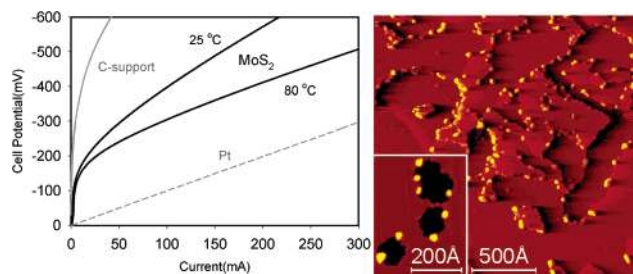
Figure 3. (Left) Polarization curve for hydrogen evolution on Pt, daihope C-support, and MoS_2 cathodes. The polarization curves for Pt and C support are made at 25 °C. The potentials are measured with respect to a carbon-supported Pt anode in a proton exchange membrane electrode assembly. (Right) STM images of MoS_2 nanoparticles on modified graphite.

results in a binding energy close to that of Pt. The FeMoco thus complies with the $\Delta G_H^\circ \cong 0$ requirement.[9] A number of research-ers have performed computational studies of hydrogenase,[10,11] and the results obtained by Siegbahn[11] allow us to calculate the atomic hydrogen adsorption free energy for a [NiFe]-hydrogenase system. The Siegbahn model for the hydrogenase active site is shown in Figure 2. When the free energy is included in Figure 1, one can see that hydrogenase also fulfils the $\Delta G_H^\circ \cong 0$ requirement and fulfils it best for all considered systems.[9]

We therefore conclude that ΔG_H° is a good descriptor of materials that can catalyze hydrogen evolution and applies to a broad range of systems, both metals and enzymes. This means that we can use the same calculations to search for other systems, which could be candidates as catalysts for hydrogen evolution. One compound we have found computationally to obey the criterion is MoS_2; see Figure 1. Comparing the nitrogenase active site and the MoS_2 edge structure, we see that they bear a close resemblance, as shown in Figure 2. In both structures, the sulfur atom, which binds the hydrogen, is 2-fold coordinated to metal atoms, either to molybdenum or to iron. Only the edges of MoS_2 are interesting in this context, as the basal plane of MoS_2 is catalytically inactive.[12] The first H that bonds to the edge is strongly bound, but at an H coverage above 0.25, the differential free energy of adsorption is 0.1 eV. According to the calculations, additional H atoms should then be able to adsorb with a low barrier or, equivalently, a low overpotential of the order 0.1 V. A good material would be nanometer-large MoS_2 crystallites supported on, for example, graphite, which is conducting but otherwise inert. Such materials are used as catalysts for hydrotreating (hydrogenation of sulfur compounds in crude oil[13]), and methods for their preparation can be found in the literature.[14] It is indeed possible to prepare nanosized MoS_2 clusters on a graphite support, as can be seen in the scanning tunnel microscope (STM) image shown in Figure 3. The MoS_2 nanoparticles are approximately 4 nm in diameter and 1 nm in apparent height, and nucleate along the graphitic steps.

We have tested experimentally whether MoS_2 nanoparticles supported on carbon can be used as catalyst for electrochemical hydrogen evolution. This was done by preparing a membrane electrode assembly (MEA), based on a Nafion proton exchange membrane, with a standard platinum electrode on one side and a MoS_2/graphite electrode on the other side. By having the same hydrogen pressure on both sides, we could make the electrochemical measurements using a Parstat 2273 potentiostat resulting in the $I-V$ curve shown in Figure 3. The experimental approach has been used successfully in other studies.[15] The conditions of the experiment correspond to pH = 0 as in the calculations. As shown in Figure 3, MoS_2/graphite is a quite reasonable material for hydrogen evolution with an overpotential in the range $0.1-0.2$ V.

We note that MoS_2 has been found to be a promoter for the hydrogen evolution activity of NiS_x electrodes,[16] which can be understood from our findings. Furthermore, MoS_2 has been tested for photocatalytic hydrogen evolution and shows activity but with significantly lower currents.[17]

Our findings suggest that we can begin searching for new catalytic materials using quantum chemical methods. The MoS_2 nanoparticles supported on graphite may be an example of a new class of electrode materials.

Supporting Information Available: Details of the DFT calcula-tions, experimental setup, and obtained data. This material is available free of charge via the Internet at http://pubs.acs.org.

References

(1) (a) Trasatti, R. S. *J. Electroanal. Chem.* **1972**, *39*, 163. (b) Bockris, J. O'M.; Reddy, A. K. N.; Gamboa-Aldeco, M. *Modern Electrochemistry 2A* 2nd ed.; Kluwer Academic/Plenum Publishers: New York, 1998.
(2) Dresselhaus, M. S.; Thomas, I. L. *Nature* **2001**, *414*, 332.
(3) (a) Evans, D. J.; Pickett C. J. *Chem. Soc. Rev.* **2003**, *32*, 268. (b) Vollbeda, A.; Fontecilla-Camps, J. C. *J. Chem. Soc., Dalton Trans.* **2003**, *21*, 4030.
(4) (a) Rees, D. C.; Howard, J. B. *Science* **2003**, *300*, 929. (b) Lee, S. C.; Holm, R. H. *Proc. Natl. Acad. Sci. U.S.A.* **2003**, *100*, 3595.
(5) Lamle, S. E.; Vincent, K. A.; Halliwell, L. M.; Albracht, S. P. J.; Armstrong, F. A. *J. Chem. Soc., Dalton Trans.* **2003**, *21*, 4152.
(6) (a) Rauchfuss, T. B. *Inorg. Chem.* **2004**, *43*, 14. (b) Meija-Rodriguez, Chong, D.; Reibenspies, J. H.; Soriaga, M. P.; Darensbourg, M. Y. *J. Am. Chem. Soc.* **2004**, *126*, 12004. (c) Razavet, M.; Davies, S. C.; Hughes, D. L.; Barclay, J. E.; Evans, D. J.; Fairhurst, S. A.; Liu, X.; Pickett, C. *J. Chem. Soc., Dalton Trans.* **2003**, *4*, 586.
(7) Nørskov, J. K.; Bligaard, T.; Logadóttir, Á.; Kitchin, J. R.; Chen, J. G.; Pandelov, S.; Stimming, U. *J. Electrochem. Soc.* **2005**, *152*, J23.
(8) Hinnemann, B.; Nørskov, J. K. *J. Am. Chem. Soc.* **2004**, *126*, 3920.
(9) The difference in pH and chemical potential for electron transfer is of the same order and cancel each other; see Supporting Information.
(10) (a) Cao, Z.; Hall, M. B. *J. Am. Chem. Soc.* **2001**, *123*, 3734. (b) Liu, Z.-P.; Hu, P. *J. Chem. Phys.* **2002**, *117*, 8177. (c) Bruschi, M.; Fantucci, P.; De Goia, L. *Inorg. Chem.* **2004**, *43*, 3733.
(11) Siegbahn, P. E. M. *Adv. Inorg. Chem.* **2004**, *56*, 101.
(12) Raybaud, P.; Hafner, J.; Kresse, G.; Kasztelan, S.; Toulhoat, H. *J. Catal.* **2000**, *189*, 129.
(13) Topsøe, H.; Clausen, B. S.; Massoth, F. E. *Hydrotreating Catalysis—Science and Technology*, Springer-Verlag: Berlin, 1996.
(14) Chorkendorff, I.; Niemantsverdriet, J. W. *Concepts of Modern Catalysis and Kinetics*; Wiley-VCH: New York, 2003.
(15) Davies, J. C.; Nielsen, R. M.; Thomsen, L. B.; Chorkendorff, I.; Logadóttir, Á.; Łodziana, Z.; Nørskov, J. K.; Li, W. X.; Hammer, B.; Longwitz, S. R.; Schnadt, J.; Vestergaard, E. K.; Vang, R. T.; Besenbacher, F. *Fuel Cells* **2004**, *4*, 309.
(16) Nidola, A.; Schira, R. *Int. J. Hydrogen Energy* **1986**, *11*, 449.
(17) Sobczynski, A. *J. Catal.* **1991**, *131*, 156.

JA0504690

Biomimetic Hydrogen Evolution: MoS$_2$ nanoparticles on graphite as catalyst for hydrogen evolution

Berit Hinnemann, Poul Georg Moses, Jacob Bonde, Kristina P. Jørgensen, Jane H. Nielsen, Sebastian Horch, Ib Chorkendorff, Jens K. Nørskov

Center for Atomic-scale Materials Physics, Department of Physics, Technical University of Denmark, DK-2800 Lyngby, Denmark

Computational Methods

All density functional calculations have been carried out with the plane-wave pseudopotential code dacapo[1], which uses a plane-wave basis and ultra soft pseudopotentials[2, 3, 4]. All energies have been calculated self-consistently with the RPBE functional[5]. For the calculations of the MoS$_2$ system, plane waves up to an energy of 30Ry have been included, and the cut-off in the electron density has been set to 180Ry. The standard choice is to take the density cutoff as four times the wavefunction cutoff (120Ry in the present case), but increasing the cutoff even further improves the accuracy for contributions from the pseudopotentials and the nonlinear core correction (double grid technique as described in Ref.4) The hydrogen adsorption energies have been calculated with a slab, which are four Mo atoms wide in x-direction and six Mo atoms wide in y-direction. The lattice constant of MoS$_2$ has been determined to be 3.235Å and compares well with the experimental lattice constant of 3.16Å. The unit cell dimension in x-direction is 12.94 Å, in y-direction 25Å and in z-direction 18Å. Electrostatic decoupling of the slabs is used. The Brillouin zone is sampled by a Monkhorst-Pack 4x1x1 k-point grid[6], i.e. 4 k-points in the x-direction, and one k-point in the y- and z-direction. The separation between neighboring k-points is 0.12Å^{-1}. The slab exposes two edges simultaneously, the $\left(10\bar{1}0\right)$ Mo-edge, which is the edge present in the catalytic particles, and the $\left(\bar{1}010\right)$ S-edge. Under the employed reaction conditions, the nanoparticles are terminated by the Mo-edge with sulfur monomers[7]. The S-edge is not present in the catalytic particles, and the exact termination is irrelevant in the calculations, as long as the same termination is used throughout. The DFT binding energies do not contain contributions from zero-point energies and entropy, and we have added these contributions separately in order to obtain the Gibbs free energy.

We describe the stability of hydrogen by the differential hydrogen chemisorption energy ΔE_H, which is calculated as follows

$$\Delta E_H = E(MoS_2+nH) - E(MoS_2+(n-1)H) - n/2\ E(H_2) \qquad (1)$$

where $E(MoS_2+nH)$ is the total DFT energy for the MoS$_2$ system with n hydrogen atoms adsorbed on the edge, $E(MoS_2+(n-1)H)$ is the total DFT energy for (n-1) hydrogen atoms adsorbed on the edge and $E(H_2)$ is the DFT energy for a hydrogen molecule in the gas phase. The differential hydrogen binding energy describes the energy needed to increase the coverage by one hydrogen atom. Our model slab is four rows of Mo wide and therefore we have four hydrogen binding sites and can describe the coverages 25%, 50%, 75% and 100%. The differential binding energy is defined such that the value for 25% indicates, how much energy is required for

increasing the coverage from 0% to 25%, the value for 50% indicates, how much energy is required to increase the coverage from 25% to 50%, and similar for the other coverages. From the DFT results we obtain the differential binding energies -0.62eV for 25%, -0.21eV for 50%, 0.48eV for 75% and 0.50eV for 100%. From these energies we calculate the Gibbs free energy for hydrogen adsorption as

$$\Delta G_H^0 = \Delta E_H + \Delta E_{ZPE} - T\Delta S_H \qquad (2)$$

where ΔE_H is the differential hydrogen chemisorption energy from the DFT calculations, ΔE_{ZPE} is the difference in zero point energy between the adsorbed state and the gas phase and ΔS_H is the entropy difference between the adsorbed state and the gas phase. The energy contribution from the configurational entropy in the adsorbed state is small (<0.04eV) and is therefore neglected. Likewise, as the vibrational entropy in the adsorbed state is small (<0.005eV), we can take the entropy of hydrogen adsorption as $\Delta S_H \cong \frac{1}{2} S_{H_2}^0$ where $S_{H_2}^0$ is the entropy of H_2 in the gas phase at standard conditions. The gas phase values are all taken from Ref. 8. We have calculated the vibrational frequencies of H adsorbed on MoS_2 with 50% coverage and found them to be 2535cm^{-1}, 594cm^{-1} and 474cm^{-1}. This means that for the MoS_2 structures $\Delta G_H^0 = \Delta E_H^{diff} + 0.29eV$. As the vibrational frequencies do not differ notably for different coverages, we use this correction for all coverages. This results in the differential binding free energies of -0.33eV for 25%, 0.08eV for 50%, 0.76eV for 75% and 0.79eV for 100%. The only free energy close to thermoneutral is 0.08eV, which describes the change in coverage from 25% to 50%. Therefore, it is most likely that the hydrogen evolution is mainly driven by hydrogen adsorption at these two coverages.

The methodology of the calculations for the nitrogenase active site is specified in Ref.9. To obtain the Gibbs free energy for hydrogen adsorption, we have calculated the vibrational frequencies for H adsorbed on the FeMoco (see Figure 2) and find them to be 2547cm^{-1}, 541cm^{-1} and 440cm^{-1}, which leads to $\Delta G_H^0 = \Delta E_H + 0.29eV$ and a free energy of hydrogen binding of -0.07eV. The hydrogen binding energy for hydrogenase has been taken from Ref.10 for the model with a charged His77, which presumably is the most realistic one. The binding energy is the energy of structure 6 (specified in Fig. 9 and 10 of Ref.10). To estimate the zero-point energy, we use the frequencies of adsorbed H on Cu(111) calculated by Gokhale *et al.*[11] as an estimate. This leads to $\Delta G_H^0 = \Delta E_H + 0.24eV$ and to a free energy of hydrogen binding of -0.05eV.

Both nitrogenase and hydrogenase work at pH=7 instead of pH=0. The change from pH=0 to pH=7 introduces a shift in redox potential of -414mV[8], which corresponds to an energy shift of -0.41eV. This means that the hydrogen adsorption energies for nitrogenase and hydrogenase are decreased by -0.41eV. The second correction results from the redox potential, with which the electrons are transferred to the active site. In nitrogenase, the electrons are provided by the $[4S-4Fe]^{1+/2+}$ redox pair, whose redox potential has been measured to be -430mV/SHE for Azotobacter vinelandii in the presence of bound MgATP[12]. This means that the electrons are provided to the FeMoco with an extra chemical potential of 430mV which corresponds to an energy shift of

0.43eV. Thus for nitrogenase, the energy corrections from pH=7 and from the electron transfer redox potential compensate each other to a large degree, so that the net correction will be small. For hydrogenase, the redox potential of the proximal [4Fe-4S] cluster is -340mV and the redox potential of the distal [4Fe-4S] cluster is -290mV[13]. Thus also in this case the energy shifts introduced by the pH=7 correction and by the redox potential for the electron transfer compensate each other to a large degree. Therefore, we can neglect these contributions in the present study.

Figure 2 has been prepared with Molscript and Raster3D[14,15].

Experiments

The catalyst used as electrode materials are hydrodesulphurization catalysts consisting of pure MoS_2 supported on active carbon. The catalyst was made by standard incipient wetness impregnation of active carbon (Mitsubishi active carbon Daihope008) with a solution of the active metals. The catalyst was then dried at 110^oC and subsequently activated by treatment sulfidation in gaseous H_2S at 450^oC. The metal loads obtained depended on the concentration of the impregnation liquid and the pore volume of the carbon and was in this case found to be 9.7% Mo.

The supported MoS_2 catalyst was then used to make one of the electrodes in a membrane electrode assembly (MEA). The MEA was made by a thin layer deposition technique described by Litster and McLean[16], where one side was prepared with Pt and the other side with a MoS_2 based electrode catalyst. The Pt side of the MEA was made using commercially available E-TEK 20 % Pt/C. Approximately 40 mg of the E-TEK powder was mixed with 0.1mL of a 5 wt% Nafion solution and diluted with methanol until an ideal viscosity was reached. When good suspension was reached, the solution was painted onto a 3.14 cm^2 torray carbon sheet, by fine paint brush. By weighing the carbon sheet before and after deposition it was found that this recipe enabled the deposition of approximately 1 mg Pt pr. cm^2. The MoS_2 electrodes were prepared in a similar manner except that the deposition was performed in a glove bag filled with nitrogen in order to reduce oxidation. Approximately 1mg of MoS_2 pr. cm^2 was deposited. After the catalyst was deposited on the carbon sheets, the sheets were bonded to a Nafion 117 membrane. The carbon sheets with catalyst, was positioned on both sides of the Nafion membrane and then pressed together with 150 bars of pressure at 120 ^oC for 5 minutes. Pressing under lower temperatures, was found to give poor bonding. The final MEAs containing MoS_2, thus consisted of one side with E-TEK Pt and one side with MoS_2 both supported on carbon.

The MEAs were tested in an experimental setup described elsewhere in detail[17] and pure hydrogen (99.9999%) was used in all experiments. First the MEA was inserted under an argon flow, then the gas flow was switched to hydrogen flow on the Pt side. A mass spectrometer probing the gas on the MoS_2 side was then used to

determine if there was any hydrogen leaking through the membrane. If no leak was detected H_2 was also flowed over the MoS$_2$ side. During measurements the H_2 flow is 25 mL/min on both sides.

The electrochemical measurements were made with a Parstat 2273, where the working electrode and the reference electrode were connected to the Pt side of the MEA, while the counter electrode was connected to the MoS$_2$ side of the MEA. Thus the potential is measured with respect to the platinum side of the MEA.

The MEA was activated by cycling the cell through potentials between 0 and -1000mV for approximately 24 hours. After the catalysts were activated, polarization curves were measured, see Figure 4, by ramping the cell potential with 30mV/min while recording the corresponding current. The applied cell potential was usually varied between 0 and -1000 mV as higher cell potentials could damage the catalyst.

The MoS$_2$ MEA has also been tested in a simple electrolysis setup, where MoS$_2$ was used as the cathode, and no significant loss in activity was measured during 60 hours of operation.

The MoS$_2$ particles on a graphite support were investigated in a stardard ultra-high vacuum (UHV) system with a scanning tunneling microscope (STM) of the Århus type[18]. The STM images were measured in a constant current mode (scanning parameters for the 2000 Å x 2000 Å image were 1V and 0.5 nA, for the smaller image of 360 Å x 460 Å, 1 V and 0.2 nA were used, see Figure 3).

The graphite surface (highly oriented pyrolytic graphite, HOPG) was cleaved in air, transported into the UHV chamber via a loadlock, and then activated by ion sputtering with 160 eV He$^+$ ions for 30 s under UHV to create defects on the surface. The sputtered surface was then heated in atmospheric air to 900K for 5 min[19]. After re-introduction into UHV, the sample was again sputtered (160 eV, 120 s). The MoS$_2$ structures were then synthesized on to the modified and activated graphite surface under UHV, following the procedure of Ref. 20, where a Au(111) surface was used as a substrate. Before imaging with STM, the samples were annealed at 1000K for 20 min.

References

(1) The plane-wave pseudopotential code dacapo is open-source and can be obtained free of charge at http://www.fysik.dtu.dk.

(2) Payne, M. C.; Teter, M. P.; Allan, D. C.; Arias, T. A.; Joannopoulos, J. D. *Rev. Mod. Phys.* **1992**, *64*, 1045.

(3) Vanderbilt, D. *Phys. Rev. B* **1990**, *41*, 7892.

(4) Laasonen, K.; Pasquarello, A.; Car, R.; Lee, C.; Vanderbilt, D. *Phys. Rev. B* **1993**, *47*, 10142.

(5) Hammer, B.; Hansen, L. B.; Nørskov, J. K. *Phys. Rev. B.* **1999**, *59*, 7413.

(6) Monkhorst, H. J.; Pack, J. D. *Phys. Rev. B* **1976**, *41*, 7892.

(7) Raybaud, P.; Hafner, J.; Kresse, G.; Kasztelan, S.; Toulhoat, H. *J. Catal.* **2000**, *189*, 129.

(8) Atkins, P. W. *Physical Chemistry*, Oxford University Press: Oxford, 1998.

(9)   Hinnemann, B.; Nørskov, J. K. *J. Am. Chem. Soc.* **2004**, *126*, 3920.

(10)   Siegbahn, P. E. M. *Adv. Inorg. Chem.* **2004**, *56*, 101.

(11)   Gokhale, A. A.; Dumesic, J. A.; Mavrikakis, M. submitted.

(12)   Ryle, M. J.; Lanzilotta, W. N.; Mortenson, L. E.; Watt, G. D.; Seefeldt, L. C. *J. Biol. Chem.* **1995**, *270*, 13112.

(13)   Teixeira, M.; Moura, I.; Xavier, A. V.; Moura, J. J. G.; LeGall, J.; DerVartanian, D. V.; Peck Jr., H. D.; Huynh, B.-H. *J. Biol. Chem.* **1989**, *264*, 16435.

(14)   Kraulis, P. *J. Appl. Crystallogr.* **1991**, *24*, 946.

(15)   Merrit, E. A.; Bacon, D. J. *Methods Enzymol.* **1997**, *277*, 505.

(16)   Litster, S.; McLean, G. *J. Power Sources* **2004**, *130*, 61.

(17)   Davies, J. C; Nielsen, R. M.; Thomsen, L. B.; Chorkendorff, I.; Logadóttir, Á.; Łodziana, Z.; Nørskov, J. K.; Li, W. X.; Hammer, B.; Longwitz, S. R.; Schnadt, J.; Vestergaard, E. K.; Vang, R. T.; Besenbacher, F., *Fuel Cells* **2004**, *4*, 309.

(18)   Besenbacher, F. *Rep. Prog. Phys.* **1996**, *59*, 1737.

(19)   Song, Z.; Cai, T.; Hanson, J. C.; Rodriguez, J. A.; Hrbek, J. *J. Am. Chem. Soc.* **2004**, *126*, 8576.

(20)   Helveg, S.; Lauritsen, J. V.; Lægsgaard, E.; Stensgaard, I.; Nørskov, J. K.; Clausen, B. S.; Topsøe, H.; Besenbacher, F. *Phys. Rev. Lett.* **2000**, *84*, 951.

.

Paper 2

Identifying the active site:
Atomic-scale imaging and ambient reactivity of MoS$_2$ nanocatalysts

Thomas F. Jaramillo[1], Kristina P. Jørgensen[1], Jacob Bonde[1], Jane H. Nielsen[1], Sebastian Horch[2], Ib Chorkendorff[1]

[1]Center for Individual Nanoparticle Functionality (CINF)

[2]Center for Atomic-scale Materials Design (CAMD)

Department of Physics, Nano-DTU, Technical University of Denmark, DK-2800 Lyngby, Denmark

One-sentence summary:

The active site of a nanoparticulate catalyst has been identified by measuring reactivity at ambient conditions on atomically imaged nanoparticles; in this case pinpointing the active site for hydrogen evolution on MoS$_2$ to be its edge.

One of the great challenges in heterogeneous catalysis is the identification of the active site. In this study, we conclusively determine the active site for hydrogen evolution on MoS$_2$ by atomically resolving the surface of this nanoparticulate catalyst prior to reactivity measurements under ambient conditions. We systematically vary different surface sites on MoS$_2$ nanoparticles on Au(111) and quantify these with Scanning Tunneling Microscopy (STM). Electrocatalytic activity measurements for hydrogen evolution correlate linearly with the number of edge sites on the MoS$_2$ catalyst. Thus, a direct coupling of the structure and catalytic turnover on MoS$_2$ nanoparticles is established.

Progress in the field of heterogeneous catalysis is often hampered by the difficulty of identifying the active site on a catalyst surface. Unlike homogeneous catalysts, where the active center is generally more clearly defined, solid-state catalysts commonly exhibit a variety of different surface sites which may or may not be active. Identifying the most active site is crucial to the design and development of improved catalytic materials [1, 2]. In pursuit of this purpose, many useful *in-situ* and *ex-situ* experimental techniques, as well as computational methods, have been developed [3, 4, 5]. Nevertheless, identifying the active site remains a challenging task – one that we undertake in this study as we aim to determine the active site of nanoparticulate MoS_2 for hydrogen evolution.

Ideally, a catalytic surface should be characterized so thoroughly that all types of surface sites are identified and quantified. This is particularly difficult on industrial catalysts as they exhibit complex morphologies. One approach to correlating activity to surface sites is to estimate surface site distributions based on particle sizes and Wulff constructions [6]. In order to minimize ambiguity in correlating activity to surface sites, however, surface science has relied upon the synthesis and characterization of model catalysts, as precise structure-activity relationships are more readily drawn on these well-defined surfaces [1]. Studies on carefully prepared single crystal metal and oxide surfaces, in well-controlled environments, were the first to bring such understanding to light. Investigations on the low-index crystal faces [7-10] were followed by studies on stepped single crystals [2, 5, 11], which more accurately model surface sites on nanoparticles. More recent studies have involved carefully deposited metal adatoms, overlayers, or nanoparticles on support materials [12-16]. In this work, we take the next step and atomically resolve the surfaces of well-defined, catalytically active nanoparticles prior to reactivity measurements under ambient conditions.

Nanoparticulate MoS_2 is one example of a nanoparticulate catalyst that has been studied in an attempt to link activity to specific surface sites. MoS_2 has gained much attention as it has been used for decades as a hydrodesulfurization (HDS) catalyst [17, 18].

Detailed insight has been gained from studies on simplified model systems in Ultra High Vacuum (UHV) and by using computational methods [19, 20], as well as from combining reactivity measurements and *ex-situ* characterization of industrial catalyst samples [17, 18, 21]. Structural studies on the MoS$_2$ catalyst have shown that it is composed almost entirely of flat polygons of S-Mo-S trilayers [17]; depending on the synthesis conditions, these trilayers may stack in a graphite-like fashion, or remain as single trilayers. For single trilayers, two general kinds of surface sites exist – terrace sites, which are those on the basal plane, and edge sites, which lie at the edge of the nanoparticles. DFT studies suggest that the active site for HDS is on the edge of the MoS$_2$ nanoparticles. This is supported by adsorption studies of thiophene using STM [22]. Despite numerous studies on this material, there is a call for studies that uniquely link the well defined structures of the model system to catalytic activity under standard reaction conditions [23].

Nanoparticulate MoS$_2$ has been shown to be active for the hydrogen evolution reaction (HER) [24], where protons and electrons combine to form molecular hydrogen, $2H^+ + 2e^- \rightarrow H_2$ [25]. In this work, we investigate this reaction as it is fundamentally important for a variety of electrochemical processes and is technologically interesting for present and future energy applications – particularly those where there is a need to replace precious metal catalysts such as Pt [24, 25]. In its bulk form, MoS$_2$ has been found to be a poor hydrogen evolution electrocatalyst [26]. Nanoparticulate MoS$_2$, however, is a more promising system as DFT calculations indicate that only the edges of MoS$_2$ nanoparticles are active for hydrogen evolution [24]; but no previous experiments has shown this conclusively.

In an attempt to provide an experimental elucidation of the active site, we have carefully prepared a sample set in UHV with deliberately chosen nanoparticulate MoS$_2$ morphologies, characterized by STM, such that the fractions of the terrace and edge sites are systematically varied. All MoS$_2$ samples in this study were synthesized on a clean Au(111) substrate by physical vapor deposition of Mo in H$_2$S, followed by annealing in

the same H_2S environment, inspired by reference [20]. Six samples were synthesized, three annealed at 400 °C and two annealed at 550 °C. Finally, a "blank" sample was synthesized by the same procedure as the others, however without the deposition of Mo. The Au(111) substrate was chosen as it serves to disperse the MoS_2 nanoparticles via its herringbone reconstruction, and is not particularly active for the HER [27]. In order to maintain discretely separated single-layered particles, the samples were purposely synthesized with low area coverages of MoS_2, less than ¼ ML (i.e. 0.25 $nm^2_{MoS2}/nm^2_{geometric}$).

Immediately after deposition, each sample is vacuum transferred to a second UHV chamber for STM imaging, Figure 1. The morphologies of the crystallized, single-layered MoS_2 nanoparticles can be described as flat polygons with a conducting edge state, seen as bright lines following the particle perimeter. Figures 1a and 1b show representative images of samples annealed at both temperatures, (a) 400 °C and (b) 550 °C, exhibiting a considerable increase in particle size for samples sintered at the higher temperature. The particles annealed to 400 °C are consistent with similarly-prepared MoS_2 nanoparticles on Au(111), reported by the Besenbacher group [20]. This is also the case for particles sintered to 550 °C despite their larger sizes. More recently, Besenbacher et al. have shown that the dominant edge structure of these nanoparticles is that of a sulfided Mo edge, and that this edge is particularly favored by larger-sized particles [19, 23]. We also observe the predominance of the sulfided Mo-edge in our samples, regardless of annealing temperature. Thus, controlled sintering allows us to change the ratio of basal plane sites to edge sites without changing the nature of the edge. Note that this sulfided Mo-edge is the same structure predicted by DFT calculations to be the active site for hydrogen evolution [24].

After imaging a sample, we transfer it out of UHV into an electrochemical cell where we measure catalytic activity for the HER. The cell, specifically designed for studies on UHV-transferred samples, is sealed upon the imaged (111) face of the sample

with a viton o-ring, exposing ~ 0.10 cm^2 to the H_2SO_4 electrolyte (pH 0.24), and cyclic voltammograms are recorded. By following this procedure, we ensure a one-to-one correlation between the imaged MoS_2 nanoparticles and the measured activity for hydrogen evolution.

Electrocatalytic activity for all six samples is shown in Figure 2 by means of polarization curves (i − E) within a cathodic potential window, and corresponding Tafel plots (log i − E). Current densities are normalized to the geometric area of the exposed face of all samples. The well-defined MoS_2 nanoparticles obtained by our preparation procedures are active for hydrogen evolution, verifying that this UHV model system truly catalyzes reactions under ambient conditions.

The most inherent measure of activity for the HER is the exchange current density, i_0 [25, 28, 29]. This value is determined by fitting i − E data to the Tafel equation [25], yielding Tafel slopes of 55-60 mV/decade, and exchange current densities in the range of 1.3 − 3.1 x 10^{-7} A/$cm^2_{geometric}$ for all MoS_2 samples (supporting online text). In Figure 3, we plot the exchange current density for each sample versus two sample parameters: (a) the MoS_2 area coverage, and (b) the MoS_2 edge state length. All data points in Figure 3(a) would fall on a straight line if the active sites for this catalyst were the terrace sites. This is clearly not the case. In Figure 3(b), however, the activities of all samples adhere to the same linear dependence on edge length. The points show some scatter around this trend, but are described by a best fit linear relation with a slope of 1.67 x 10^{-20} A/$nm_{MoS2-edge}$. As the rate of reaction is directly proportional to the number of edge sites for all samples, regardless of particle size, we conclude that the edge site is indeed the active site. Bearing this in mind, it is worth revisiting Figure 3(a) to note that the exchange current densities of the samples sintered at 550°C are significantly lower than those prepared at 400°C, per MoS_2 coverage, exactly as one would expect since the sintered samples have less edge length per area of MoS_2. Figure 3 thus provides conclusive experimental evidence

pinpointing the active site to the edge of the MoS$_2$ nanoparticles, validating predictions from DFT calculations [24].

Another important question to answer regarding this material is how well it compares to other materials, specifically those known to catalyze the HER effectively. The most direct method to compare catalysts is on a per active site basis [1], and having identified the active site to be on the edge of the MoS$_2$ nanoparticles, we can now directly compare their activity for hydrogen evolution to that of the pure metals, as their activities are well known [28]. For this direct site-to-site comparison, we will use the 1.5 x 10^{15} sites/cm^2 of the Pt(111) face as the basis for comparison, as Pt is the archetypical HER catalyst. An exchange current density of 4.5 x 10^{-4} A/cm^2 for this face [30] yields a turn over frequency (TOF) of 0.9 s^{-1} (supporting online text). In general, TOFs of transition metals range over 10 orders of magnitude (Hg, for instance, has a TOF as low as ~ 10^{-9} s^{-1}) [28]. Given the slope in Figure 3(b), we have calculated the TOF of the MoS$_2$ edge to be 0.02 s^{-1}, indeed in the high range of TOFs for metals.

For further insight into the catalytic nature of the MoS$_2$ edge, a recent version of the volcano-type relationship observed for HER catalysts is shown in Figure 4, to which we have added our data for nanoparticulate MoS$_2$. A number of volcano curves have been published for HER catalysts in the last 50 years relating exchange current density to different physico-chemical properties of metals such as work function, metal-hydride enthalpy of formation, or Gibbs free energy for hydrogen adsorption (ΔG_H) [28, 29]. Volcano relationships ultimately reflect the Sabatier principle – a general framework in catalysis that explains that optimal surfaces exhibit moderate binding energies of reaction intermediates, e.g. hydrogen adsorption in the case of the HER. In Figure 4, the exchange current density is shown as a function of the DFT-calculated free energy of adsorption of hydrogen, which was recently determined to be +0.08 eV for the MoS$_2$ edge [24]. In order to add MoS$_2$ to this figure, we convert the TOF of nanoparticulate MoS$_2$ to its exchange current density per 1.5 x 10^{15} sites/cm^2, which yields 7.9 x 10^{-6} A/cm^2 (supporting online

text). This value surpasses those of the common metals, and lies just below those of the precious Pt-group metals. When plotting this experimentally determined activity of the edge site versus its DFT-calculated ΔG_H [24], we see that it follows the volcano trend [29]. This validates the predictive capability of this DFT model as well as its applicability beyond metal catalysts.

After identifying the active site and comparing it to typical metal catalysts, we may consider how to improve the activity of that site and thereby the catalyst material. The DFT-calculated ΔG_H of the MoS_2 edge site is slightly positive at +0.08 eV, with calculations suggesting a H-coverage of only ¼ on the edge under operating conditions [24]. Thus, only 1 in 4 edge atoms evolves molecular H_2 at a given time, unlike Pt(111) which operates at a H-coverage of ~ 1 ML [30]. If all MoS_2 edge sites could be made to adsorb H, activity could be increased by a factor of 4. This might be accomplished by appropriately tuning the electronic structure of the edge to increase the bond strength of the adsorbed H [29]. Such a modification could simultaneously improve the inherent turnover of each edge site, further improving the overall activity of the material towards that of Pt-group metals.

Identifying the active site is crucial in developing better catalysts; this is particularly important for energy-conversion technologies where precious metals need to be replaced. In this work, we have identified the active site in MoS_2 by atomically resolving the surface of this nanoparticulate catalyst prior to reactivity measurements under ambient conditions. Systematic variations of surface sites show that hydrogen evolution activity correlates with the number of edge sites on the nanoparticles. The edge site of MoS_2 was found to be more active than earth-abundant transition metals, and its activity agrees with predictions based on DFT-calculations. Correlating atomically imaged nanostructures with catalytic turnover under ambient conditions is a challenging, but direct approach that identifies the active site. With this knowledge, research efforts can be focused on improving that specific site and thereby the catalyst material.

References and Notes

1: G. A. Somorjai, *Introduction to Surface Chemistry and Catalysis* (Wiley-Interscience, New York, 1994).

2: T. Zambelli, J. Wintterlin, J. Trost, G. Ertl, *Science* **273**, 1688 (1996).

3: C.T. Campbell, *Science* **294** 1471 (2001).

4: N. I. Jaeger, *Science* **293** 1601 (2001).

5: S. Dahl, et al., *Phys. Rev. Lett.* **83**, 1814 (1999).

6: T. V. W. Janssens, A. Carlsson, A. Puig-Molina, B. S. Clausen, *J. Catal.* **240**, 108 (2006).

7: D. W. Goodman, R. D. Kelley, T. E. Madey, J. T. Yates, Jr. *J. Catal.* **63,** 226 (1980).

8: R. R. Adzic, A. V. Tripkovic, W. E. O'Grady, *Nature* **296,** 137 (1982).

9: J. Clavilier, R. Parsons, R. Durand, C. Lamy, J. M. Leger, *J. Electroanal. Chem.* **124,** 321 (1981).

10: A. A. Gewirth, A. J. Bard, *J. Phys. Chem.* **92,** 5563 (1988).

11: R. R. Adzic, A. V. Tripkovic, V. B. Vesovic, *J. Electroanal. Chem.* **204,** 329 (1986).

12: F. Maroun, F. Ozanam, O. M. Magnussen, R. J. Behm, *Science* **293,** 1811 (2001).

13: M. S. Chen, D. W. Goodman, *Science* **306**, 252 (2004).

14: L. A.Kibler, A. M. El-Aziz, R. Hoyer, D. M. Kolb, *Ang. Chem. Int. Ed.* **44,** 2080 (2005).

15: E. Herrero, J. M. Feliu, A. Wieckowski, *Langmuir* **15,** 4944 (1999).

16: K. H. Hansen, et al., *Phys. Rev. Lett.* **83,** 4120 (1999).

17: H. Topsøe, B.S. Clausen, F.E. Massoth, in *Catalysis-Science and Technology*, J. R. Anderson, M. Boudart Eds. (Springer-Verlag, New York, 1996), vol. 11.

18: R. R. Chianelli, et al., *Catal. Rev.* **48**, 1 (2006).

19: M. V. Bollinger, et al., *Phys. Rev. Lett.* **87**, 19 (2001).

20: S. Helveg, et al., *Phys. Rev. Lett.* **84,** 951 (2000).

21: R. Prins, V. H. J. de Beer, G. A. Somorjai, *Catal. Rev. – Sci. Eng.*, **31**, 1 (1989).

22: J. V. Lauritsen, et al., *J. Catal.* **224**, 94 (2004).

23: J.V. Lauritsen, et al., *Nature Nanotech.* **2**, 53 (2007) .

24 : B. Hinneman, et al., *J. Am. Chem. Soc.* **127,** 5308 (2005).

25: J. O. M. Bockris, S. U. M. Khan, *Surface Electrochemistry: A Molecular Level Approach.* (Plenum Press, New York, 1993), pp. 1014.

26: W. Jaegermann, H. Tributsch, *Prog. Surf. Sci.* **29,** 1 (1988).

27: J. Perez, E. R. Gonzalez, H. M. Villullas, *J. Phys. Chem. B* **102,** 10931 (1998).

28: S. Trasatti, *J. Electroanal. Chem.* **39**, 163 (1972).

29: J. K. Nørskov, et al., *J. Electrochem. Soc.* **152**, J23 (2005).

30: N. M. Markovic, B. N. Grgur, P. N. Ross, *J. Phys. Chem. B* **101,** 5405 (1997).

Figure Captions

Figure 1.

STM images of MoS_2 nanoparticles on Au(111). The particles have the well known

morphology of polygons with conducting edge states and are dispersed on the Au surface

irrespective of coverage and annealing temperature (400 °C or 550 °C). (a) low coverage

(0.06 nm^2_{MoS2}/$nm^2_{geom.}$), annealed to 400 °C (470 Å x 470 Å, 1.2 nA, 4 mV). (b) high

coverage (0.23 nm^2_{MoS2}/$nm^2_{geom.}$), annealed to 550 °C (470 Å x 470 Å, 1.2 nA,1.9 V).

(c) Atomically resolved MoS_2 particle, from a sample annealed to 550 °C, showing the

predominance of the sulfided Mo-edge [19, 20]. (60 Å x 60 Å, 1.0 nA, 300 mV).

Figure 2.

Polarization curves and Tafel plots in a cathodic potential window for the 5 different

MoS_2 samples as well as the blank sample. Samples annealed to 400 °C are dark blue,

samples annealed to 550 °C light blue. Main: Polarization curve showing hydrogen

evolution on all samples. Inset: Tafel plot. Note that all the MoS_2 samples have Tafel

slopes of 55-60 mV/dec irrespective of annealing temperature and coverage. Sweep rate:

5 mV/s. Data is iR corrected.

Figure 3.

Exchange current density vs. MoS_2 area coverage (a) and MoS_2 edge length (b). In both

figures, open circles are samples annealed to 400 °C, filled circles are samples annealed

to 550 °C. The exchange current density does not correlate with the area coverage of

MoS_2, whereas it shows a linear dependence on the MoS_2 edge length, clearly showing

that the active site for the hydrogen evolution reaction is on the particle edge. Exchange current densities are extracted from the Tafel plot in Figure 2.The edge length is measured on all imaged particles and normalized by the imaged area.

Figure 4.

Volcano plot of the exchange current density as a function of the DFT-calculated Gibbs free energy of adsorbed hydrogen for nanoparticulate MoS_2 and the pure metals [29]. As seen, MoS_2 follows the same trend as the pure metals. The MoS_2 exchange current density is normalized to the atomic site density of Pt for comparison. Samples are polycrystalline unless otherwise noted.

Figure 1.
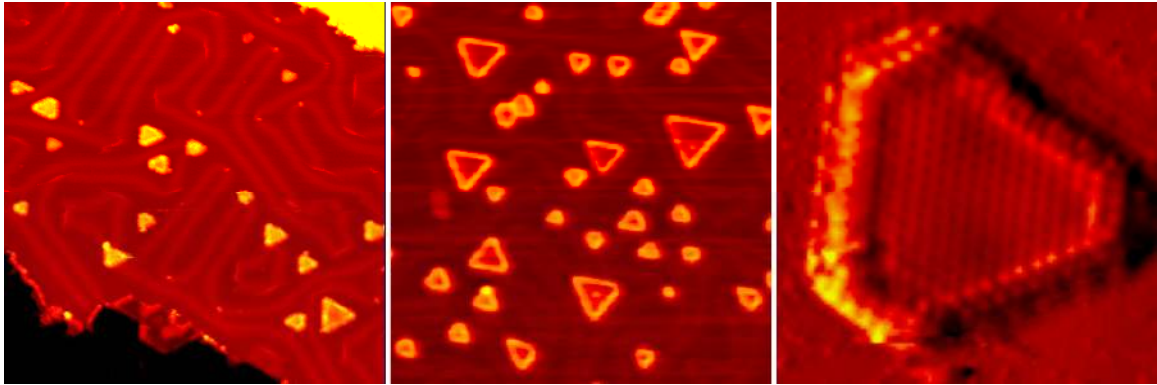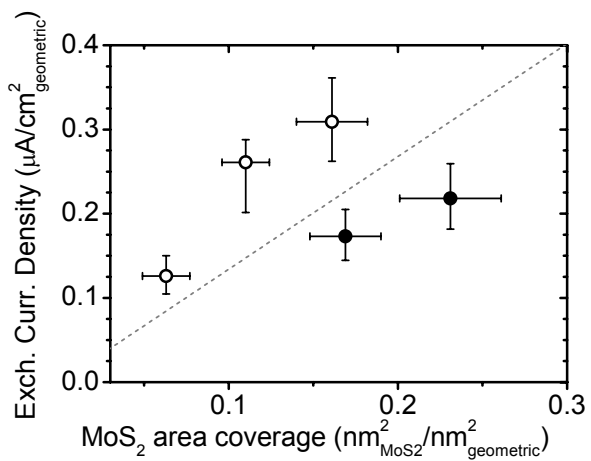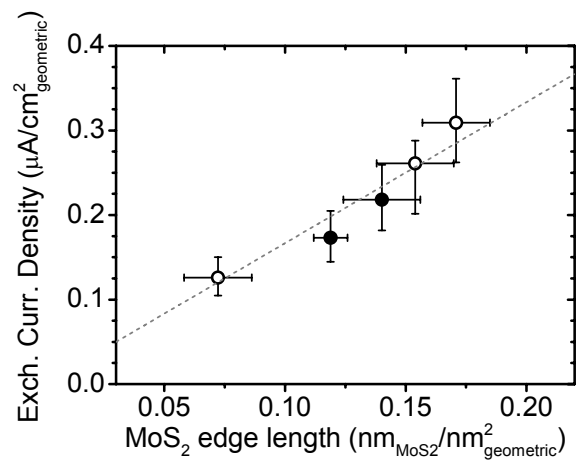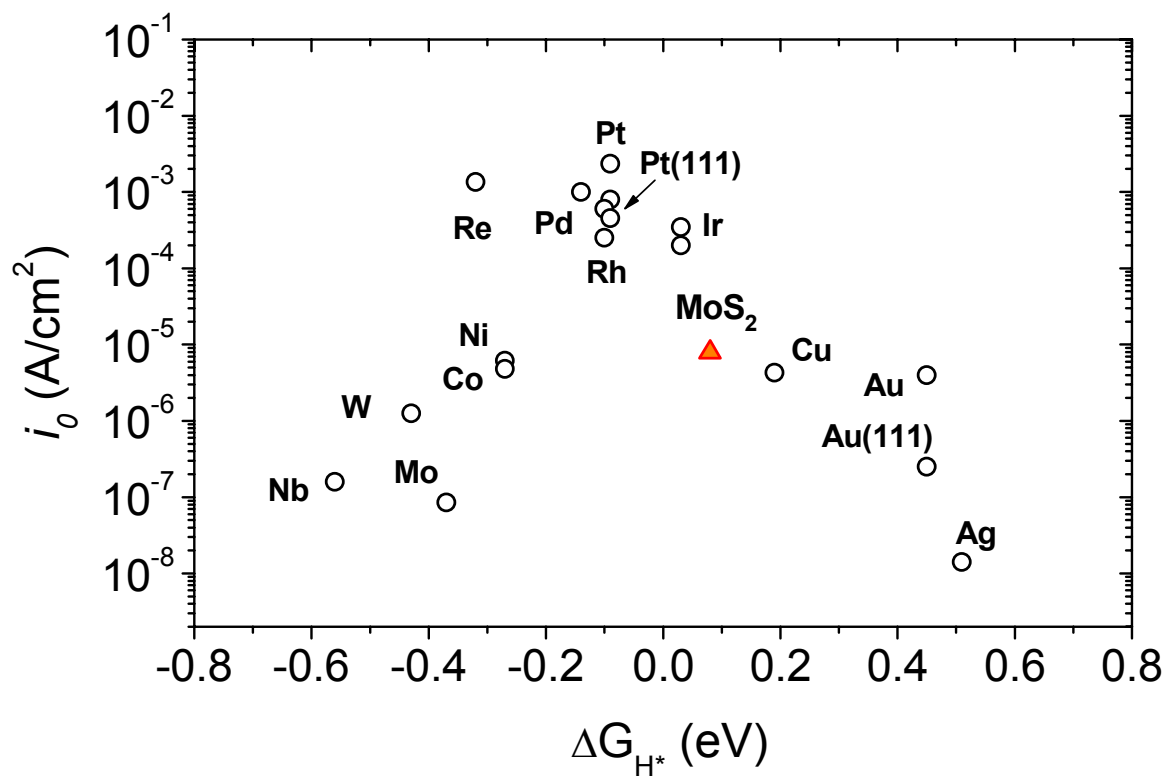

(a)　　　　　　　(b)　　　　　　　(c)

Figure 2.
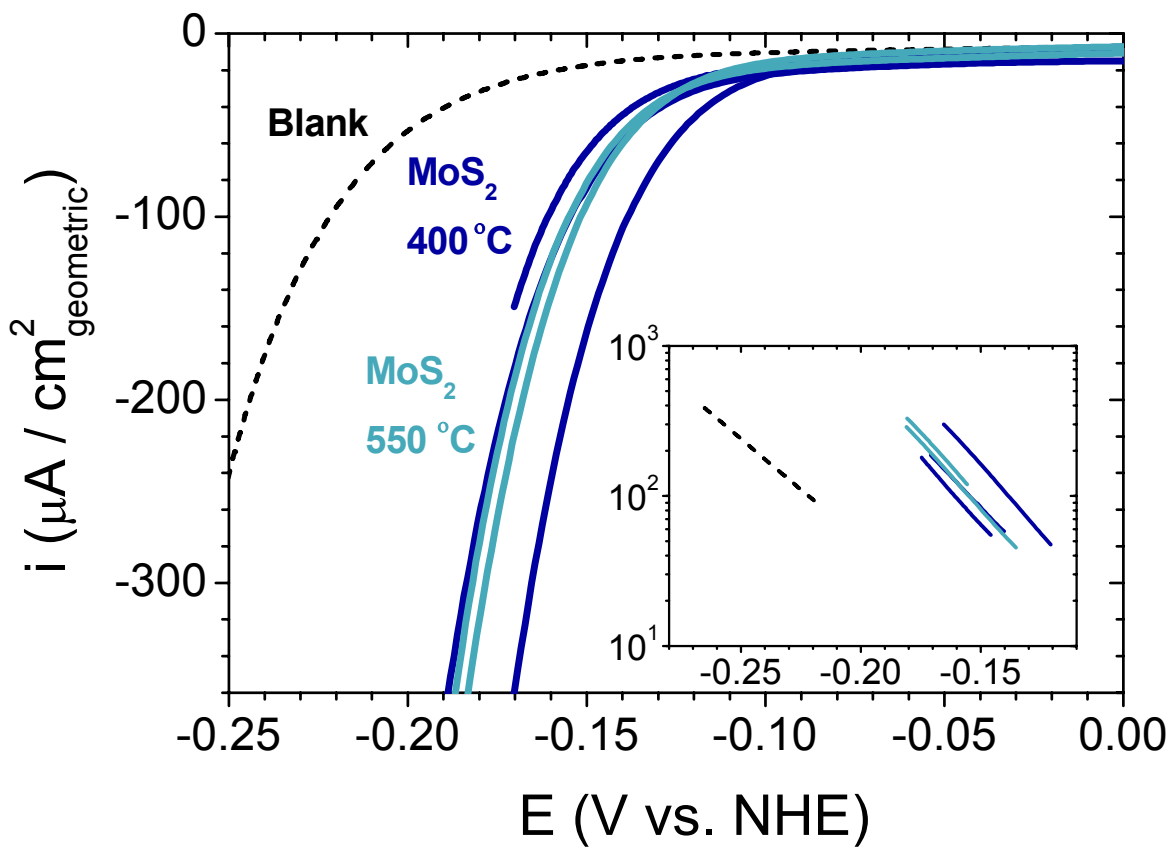
Figure 3.

(a)

(b)

Figure 4.

Supporting Online Material

The MoS_2 is deposited onto Au(111) after the crystal has been cleaned by sputter-annealing cycles. Mo is vapor deposited from a thoroughly degassed resistively heated Mo filament. Cleanliness of Au and the purity of Mo is confirmed by XPS and STM. Mo is deposited and post-annealed in a sulfiding atmosphere achieved by leaking H_2S through a directed doser until a chamber pressure of 10^{-7} Torr is reached.

After deposition the MoS_2/Au(111) sample is transferred in vacuum to a second UHV chamber and STM is performed with an Aarhus-type STM [S1]. STM images are scanned in constant current mode, and a number of 470 Å x 470 Å, 512 x 512 pixel images are obtained for analysis. The well-known structure of MoS_2 [20] is confirmed by atomically resolved images. MoS_2 edge length is found by measuring the edge state length of all particles in each image, and normalizing the sum of these by the area of the analyzed images, resulting in an "edge length unit" of $nm_{MoS2\text{-}edge}/nm^2_{geometric}$.

For HER measurements aqueous H_2SO_4 at pH 0.24 (de-aerated with N_2) was used. A platinum mesh counter electrode and a SCE reference electrode were employed. Cyclic voltammograms were measured at 5 mV/s using a PAR VMP2 potentiostat. All data are corrected for a small ohmic drop using impedance spectroscopy. In addition to using exchange current density as a measure of HER activity, one can also use the current density at a specific overpotential from the polarization curves. In general, this figure of merit is more pertinent on practical devices, such as fuel cells or electrolyzers, whereas exchange current density is a property of more fundamental interest. Figure S1 exhibits current densities measured at -150 mV overpotential versus (a) area coverage and (b) edge state length, analogous to the exchange current density scatter plots in Figure 3. Figure S1 affirms the conclusions drawn from Figure 3: current density is not determined by the MoS_2 area coverage – it is linearly dependent on the MoS_2 edge length.

Table S1 compiles results from analysis of STM images and electrochemical data.

Annealing temperature	MoS$_2$ Area coverage nm^2/nm^2	MoS$_2$ Edge length nm/nm^2	Exchange current density μA/cm^2	Tafel Slope (mV/decade)	R^2 for fitting to Tafel equation
Blank - 400°C	-	-	9.84E-08	-73.8	> 0.999
400°C	0.063	0.072	1.26E-07	-55.5	> 0.999
400°C	0.110	0.154	2.61E-07	-59.9	> 0.999
400°C	0.161	0.171	3.09E-07	-55.2	> 0.999
550°C	0.231	0.140	2.18E-07	-56.7	> 0.999
550°C	0.169	0.119	1.73E-07	-56.1	> 0.999

Table S1: Annealing temperature, MoS$_2$ area coverage, MoS$_2$ edge length, exchange current densities and Tafel slopes (and their R^2 values).

For MoS$_2$ samples, an exchange current per site was determined by the slope of the linear fit of exchange current density (A / cm$^2_{geometric}$) versus edge state length (nm$_{MoS2\text{-}edge}$/nm$^2_{geometric}$), resulting in 1.67 x 10^{-20} A/nm$_{MoS2\text{-}edge}$ and an R^2 value of 0.93. The Mo-Mo and S-S distances in MoS$_2$ are 3.15 Å [20], resulting in (1/0.315) sites/nm$_{MoS2\text{-}edge}$. This yields 5.25 x 10^{-21} A/site. This value was then multiplied by the site density of Pt (1.5 x 10^{15} sites/cm^2) for a fair comparison to transition metals, resulting in 7.9 x 10^{-6} A/cm^2, as seen in Table S2.

Turn-over frequencies are calculated in Table S2 from exchange current densities using the following relation:

$$\text{TOF (s}^{-1}) = (i_0, \text{A/cm}^2) / [(1.5 \times 10^{15} \text{ sites/cm}^2)(1.602 \times 10^{-19} \text{ C/e}^-)(2 \text{ e}^-/\text{H}_2)]$$

Material	Exchange current density (A/cm^2), assuming 1.5 x 10^{15} sites/cm^2	Exchange current pr site (A/site)	TOF (s^{-1})
Pt(111)	4.5E-04 [30]	3.00E-19	0.94
Hg	5.0E-13 [28]	3.34E-28	1.04E-09
MoS$_2$-edge	7.9E-06	5.25E-21	1.64E-02

Table S2: Calculation of TOFs.
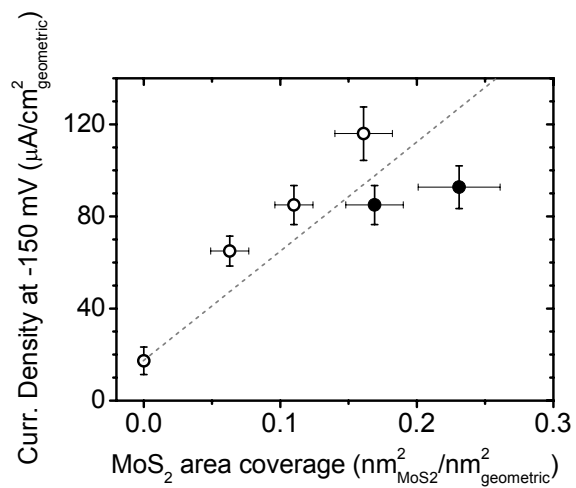
Supporting References

S1. E. Lægsgaard, F. Besenbacher, K. Mortensen, I. Stensgaard, *J. Microsc.* **152** 663 (1988).
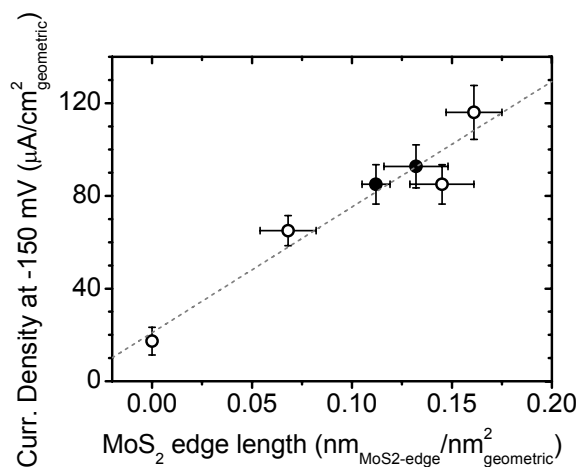
Supporting Figure Captions

Figure S1.

Current density at -150 mV vs. NHE as a function of MoS_2 area coverage (a) and MoS_2 edge length (b). In both figures, open circles are samples annealed to 400 °C, filled circles are samples annealed to 550 °C. The current density does not correlate with the area coverage of MoS_2, whereas it shows a linear dependence on the MoS_2 edge length. This is further support that the active site for the hydrogen evolution reaction is on the particle edge. The edge length is measured on all imaged particles and normalized by the imaged area, similar to Figure 3.

Figure S1.

(a)

(b)